

RECEIVER AUTONOMOUS INTEGRITY MONITORING AGAINST ORBIT  
EPHEMERIS FAULTS IN CARRIER PHASE DIFFERENTIAL GPS

BY  
STEFAN STEVANOVIC

Submitted in partial fulfillment of the  
requirements for the degree of  
Master of Science in Mechanical and Aerospace Engineering  
in the Graduate College of the  
Illinois Institute of Technology

Approved \_\_\_\_\_  
Advisor

Chicago, Illinois  
May 2013



## ACKNOWLEDGMENT

This work would not have been possible without my advisor, Professor Boris Pervan. I thank him very much for giving me the opportunity to conduct this research. I especially value his insightful ideas, patience, and encouragement throughout my graduate studies. I would like to thank Professor Matthew Spenko, and Professor Kevin Cassel for serving on the oral defense committee. The time they set aside to read and provide valuable comments on this work is greatly appreciated.

I also thank my lab mates of the Navigation Lab: Dr. Mathieu Joerger, Dr. Samer Khanafseh, Dr. Fang Chan, Jing Jing, Steven Langel, and Farui Peng. I feel very lucky to be associated with the lab and these wonderful individuals. I am especially grateful to Dr. Mathieu Joerger for his support and encouragement throughout this process. His ideas and suggestions through our close collaboration have made this work possible. I also appreciate the time he spent reading and providing comments on this document, which greatly improved its quality. I would like to thank Dr. Samer Khanafseh, for his willingness to answer questions and improve my understanding of the algorithms this work is based upon. In addition, I would like to acknowledge the Naval Air Warfare Center (NAVAIR) of the US Navy for sponsoring this research.

Finally, this work is dedicated to my family, who continued to support me throughout my education. My parents Dragan and Velinka Stevanovic, made endless sacrifices to provide me with the opportunities I have now. I also thank my sister Danica (who constantly tests my knowledge) for her support and encouragement.

## TABLE OF CONTENTS

	Page
ACKNOWLEDGEMENT . . . . .	iii
LIST OF TABLES . . . . .	vii
LIST OF FIGURES . . . . .	viii
LIST OF SYMBOLS . . . . .	ix
LIST OF ABBREVIATIONS . . . . .	x
ABSTRACT . . . . .	xii
CHAPTER	
1. INTRODUCTION . . . . .	1
1.1. Background on GPS . . . . .	1
1.1.1. Architecture and Signal Structure . . . . .	2
1.1.2. Sources of Error . . . . .	4
1.1.3. Navigation Performance Metrics . . . . .	6
1.2. High Accuracy and High Integrity Applications . . . . .	7
1.2.1. Carrier Phase Differential GPS (CPDGPS) . . . . .	7
1.2.2. Prior Work on Integrity Monitoring in CPDGPS . . . . .	8
1.2.3. Contributions . . . . .	9
2. RELATIVE POSITIONING AND CYCLE RESOLUTION ALGORITHMS . . . . .	11
2.1. Carrier Phase Differential GPS . . . . .	11
2.1.1. Differential Measurements . . . . .	11
2.1.2. Geometry Free Measurements . . . . .	15
2.1.3. Positioning Algorithm for Benchmark Application . . . . .	17
2.2. Integrity in Cycle Ambiguity Resolution . . . . .	20
2.2.1. Integer Fixing Procedure . . . . .	20
2.2.2. Integrity Risk Requirement . . . . .	21
2.3. Fault Free Integrity in Bootstrap Cycle Resolution . . . . .	22
2.3.1. Bootstrap Integrity Risk Bound . . . . .	23
2.3.2. Computing The Probability of Fix . . . . .	24
2.4. Fault Free Integrity in EPIC-Light Cycle Resolution . . . . .	25
2.4.1. EPIC-Light Integrity Risk Bound . . . . .	25
2.4.2. Integer Candidate Subset . . . . .	26
2.4.3. Probability Computations . . . . .	26

2.4.4. Impact on Position Domain . . . . .	27
3. UPDATED ERROR AND FAULT MODELS . . . . .	29
3.1. Differential Error Models . . . . .	29
3.1.1. Ionospheric Error Model . . . . .	30
3.1.2. Tropospheric Error Model . . . . .	32
3.2. Receiver Noise and Multipath Error Models . . . . .	33
3.2.1. Carrier Time-Correlation . . . . .	34
3.2.2. Geometry Free Noise Variance . . . . .	35
3.2.3. Correlation of GF Measurements with Carrier Measurements . . . . .	36
3.3. Complete Error Covariance Matrix Derivation . . . . .	38
3.3.1. Receiver Noise and Multipath . . . . .	40
3.3.2. Ionosphere and Troposphere . . . . .	41
3.3.3. Correlation Matrix Between Geometry-Free and Carrier Measurements . . . . .	42
3.3.4. Carrier Phase Measurement Time-Correlation . . . . .	43
3.3.5. Case of Multiple Reference Receivers . . . . .	44
3.4. Orbit Ephemeris Fault (OEF) . . . . .	45
3.4.1. Types of Orbit Ephemeris Faults . . . . .	45
3.4.2. Effect on Differential Measurements . . . . .	46
3.4.3. Ephemeris Fault Vector For Straight in Approach . . . . .	46
3.4.4. Orbit Ephemeris Fault Modelling . . . . .	48
4. ORBIT EPHEMERIS FAULT DETECTION . . . . .	50
4.1. Differential RAIM . . . . .	50
4.2. Relative RAIM . . . . .	52
4.2.1. Relative Fault Vector and Noise Covariance Matrix Derivation . . . . .	56
4.2.2. Relative Residual . . . . .	56
4.2.3. Test Statistic Correlation . . . . .	57
4.3. Unified RAIM Concept . . . . .	60
5. UNIFIED RAIM FOR FIXED SOLUTION USING EPIC . . . . .	63
5.1. Modifying the Integrity Risk Bound . . . . .	63
5.2. Modifying the Integer Candidate Subset Selection . . . . .	66
5.3. Impact on Position Domain . . . . .	67
5.4. Evaluation of the EPIC-Light URAIM Integrity Risk Bound . . . . .	69
5.5. EPIC-URAIM Integrity Risk Evaluation For All Possible Faults . . . . .	70

5.6. EPIC-URAIM Fixing Criterion . . . . .	71
6. AVAILABILITY PERFORMANCE ANALYSIS . . . . .	76
6.1. Framework For JPALS Benchmark Application . . . . .	76
6.2. Float URAIM Results . . . . .	78
6.3. Understanding EPIC-URAIM . . . . .	80
6.3.1. Impact of Fault Magnitude . . . . .	80
6.3.2. Impact of Candidates . . . . .	84
6.3.3. Impact of Fixing . . . . .	87
6.4. EPIC-URAIM Single Location Results . . . . .	89
6.5. Unified RAIM Results - EPIC light . . . . .	93
7. CONCLUSION . . . . .	95
7.1. Measurement Error Models . . . . .	95
7.2. Unified RAIM . . . . .	95
7.3. RAIM With Fixing Cycle Ambiguities . . . . .	96
7.4. Recommendations and Future Work . . . . .	97
APPENDIX . . . . .	99
A. CLOSED-FORM EXPRESSION OF FINITE SERIES TERM FOR MEASUREMENT TIME-CORRELATION . . . . .	99
B. DERIVATION OF GEOMETRY-FREE MEASUREMENT NOISE VARIANCE USING DISCRETE SAMPLING RATE . . . . .	102
C. FILTERED GEOMETRY FREE MEASUREMENT CORRELA- TION WITH CARRIER MEASUREMENT AT INITIAL EPOCH . . . . .	105
D. INDEPENDENT TEST STATISTIC FOR RRAIM . . . . .	108
E. LIMITATIONS OF A MEASUREMENT EQUATION USED TO GENERATE THE TEST STATISTIC . . . . .	111
E.1. Test Statistic Derived Using RRAIM Measurement Equation	114
E.2. Test Statistic Derived Using URAIM Measurement Equation	115
E.3. Working Detector Criteria . . . . .	117
F. CANDIDATE GENERATION FOR EPIC-LIGHT . . . . .	119
BIBLIOGRAPHY . . . . .	121

## LIST OF TABLES

Table	Page
6.1 Example (JPALS) System Requirements . . . . .	77
6.2 Float Simulation Parameters . . . . .	79
6.3 Single Location EPIC-URAIM Simulation Parameters . . . . .	90
6.4 Avail. for Location 35N -150E; 0.5nmi to TD . . . . .	92

## LIST OF FIGURES

Figure	Page
1.1 GPS System Architecture [GPSb] . . . . .	2
1.2 GPS Satellite Constellation [GPSa] . . . . .	3
2.1 Relative Positioning . . . . .	14
3.1 Ionospheric and tropospheric layers . . . . .	30
5.1 Overview of EPIC-URAIM Fixing Criterion 1 . . . . .	72
5.2 EPIC-URAIM Fixing Criterion 2: Minimizing Integrity Risk Bound	74
5.3 EPIC-URAIM Fixing Criterion 3: Maximum Number of Integer Fixes	75
6.1 Example Integrity Allocation Tree . . . . .	77
6.2 Comparison of DRAIM and URAIM float availability performance	79
6.3 Bound on $P(HMI   F)$ for all fault modes . . . . .	82
6.4 EPIC with 1/8 fixed integers . . . . .	82
6.5 EPIC with 8/8 fixed integers . . . . .	83
6.6 Probability of fix occurrence . . . . .	85
6.7 Integrity risk and probability of fixing to candidate set versus number of candidates . . . . .	86
6.8 Inflated measurement noise effect on candidate set . . . . .	87
6.9 Bound on $P(HMI   F)$ and modified probability of HI versus number of candidates . . . . .	88
6.10 Impact of fixing integers on integrity risk . . . . .	89
6.11 URAIM using EPIC-light results over 24 hr period . . . . .	90
6.12 URAIM using EPIC-light results over 24 hr period using fewer candidates . . . . .	92
6.13 World map showing the simulation grid points . . . . .	93
6.14 Integrity availability of sea based locations for JPALS . . . . .	94
C.1 GF carrier measurement sampling during approach . . . . .	106

## LIST OF SYMBOLS

Symbol	Definition
$\mathbf{u}$	state vector (includes position and ambiguity states)
$\mathbf{x}$	position state vector
$\mathbf{n}$	cycle ambiguity state vector
$\delta \square$	error in $\square$
${}^i \square$	$\square$ for space vehicle (i.e. satellite) $i$
$ \square$	given $\square$
$P(\square)$	probability of event $\square$
$E\{\square\}$	expected value operator, on $\square$
$\langle \square \rangle$	round $\square$ to nearest integer (if vector round each element)
$\check{\square}$	updated $\square$ after integer fixing

## LIST OF ABBREVIATIONS

Abbreviation	Definition
CPDGPS	Carrier Phase Differential GPS
DGPS	Differential GPS
GPS	Global Positioning System
GNSS	Global Navigation Satellite System
LAMBDA	Least-Square Ambiguity Decorrelation Adjustment
MEO	Medium Earth Orbit
TD	Touch down
CDF	Cumulative Distribution Function
SV	Space Vehicle (satellite)
GF	Geometry Free
BS	Bootstap
EPIC	Enforced Position-Domain Integrity-Risk Cycle [Resolution Algorithm]
MP	Multipath
OEF	Orbit Ephemeris Fault
MLF	Most Likely Fix

NFF	Noise Free Fix
RAIM	Receiver Autonomous Integrity Monitor
DRAIM	Differential RAIM
RRAIM	Relative RAIM
URAIM	Unified RAIM

## ABSTRACT

This work investigates the potential of the Global Positioning System (GPS) to enable a safe approach for rendezvous applications including shipboard landing of military aircraft. GPS has been shown to have the necessary accuracy for such an operation, and could potentially replace the existing radar or laser based systems. [Kha08][WPF08]<sup>1</sup> However, to ensure safe operation, GPS must also be able to avoid hazardous situations. Shipboard aircraft approach navigation is an example rendezvous application requiring both high accuracy and high integrity. In this work, GPS measurement error models and orbit ephemeris fault (OEF) detection algorithms are developed for rendezvous applications, and performance is analyzed for the aircraft shipboard landing application.

Both reference station and user based monitors can be used for orbit ephemeris fault detection. The available reference monitors either require a stationary reference receiver, or cannot protect against all types of orbit ephemeris faults. As an alternative, this work develops and investigates the use of receiver autonomous integrity monitoring (RAIM), which is user-based. Two contrasting algorithms, differential RAIM (DRAIM) and relative RAIM (RRAIM) are derived and analyzed for a realistic shipboard landing application. DRAIM is most effective when the aircraft first begins the approach. On the other hand, RRAIM performs best near the end of the approach.

Assessing integrity risk is shown to be a major challenge for the RRAIM algorithm. Thus, a new unified RAIM (URAIM) concept is introduced. It seamlessly integrates DRAIM and RRAIM into a single detection algorithm, and also facilitates integrity risk evaluation. This is because the URAIM measurement equation can be used for both position estimation as well as fault detection.

---

<sup>1</sup>Corresponding to references in the Bibliography.

Since high accuracy is desired, fixing integer cycle ambiguities is required. The Enforced Position-Domain Integrity-Risk Cycle Resolution Algorithm (EPIC) method of integrity risk bounding is used along with the URAIM fault detection algorithm in what we call the EPIC-URAIM algorithm. In general, the OEF will interfere with the cycle resolution process. In this work, the EPIC integrity risk bound formula is modified to account for the presence of an OEF. The EPIC-URAIM algorithm is simulated for 1507 sea-based locations around the globe. An average global availability of accuracy and integrity of 98.6% is achieved. This work illustrates the feasibility of detecting orbit ephemeris faults with integrity, while simultaneously meeting stringent accuracy requirements for real-time rendezvous navigation applications.

## CHAPTER 1

### INTRODUCTION

This work investigates the potential of the Global Positioning System (GPS) to enable safe navigation for rendezvous applications including shipboard landing of military aircraft. GPS has been shown to have the necessary accuracy for such operations, and could potentially replace the existing visual, radar or laser based systems [Kha08][WPF08]. However, to ensure safe operation, GPS must also be able to avoid hazardous situations. Shipboard aircraft approach navigation is an example rendezvous application requiring both high accuracy and high integrity. In this work, GPS measurement error models and orbit ephemeris fault (OEF) detection algorithms are developed for rendezvous applications, and performance is analyzed for the aircraft shipboard landing application.

#### 1.1 Background on GPS

The Global Positioning System (GPS) is a satellite (space vehicle) based navigation system. It is a global navigation satellite system (GNSS) that provides global coverage of four or more space vehicles (SVs). Developed by the department of defense in the 1970s for use by the military, GPS is now available to civilian users. GPS is a passive system, which means that the SVs blanket the earth with their signals, and users process these signals to determine their position. There is no two-way communication between the satellite and user. This means that GPS can potentially have an unlimited number of simultaneous users. The worldwide coverage of GPS motivates ongoing research aimed at bringing it into use for a wide variety of applications.

We begin by discussing the current GPS architecture and signal structure. Then some common sources of error are introduced, and we discuss the metrics used

to quantify GPS performance.

**1.1.1 Architecture and Signal Structure.** GPS is arranged into three segments, the space, control and user segments. Figure 1.1 illustrates the interaction between these three main segments. The space segment consists of the GPS satellites or space vehicles (SVs). A representation of the GPS constellation is shown in Figure 1.2. The constellation is composed of 24 nominal SVs in a medium earth orbit (MEO), at roughly 20 thousand kilometers altitude. Satellites broadcast signals which users process to determine their position. Signal structure will be discussed in the next section. In addition, the SVs are able to receive signals broadcast from the control segment. Note that each satellite is equipped with an atomic clock. Time synchronization between all SVs and the user is the key to reducing positioning error.

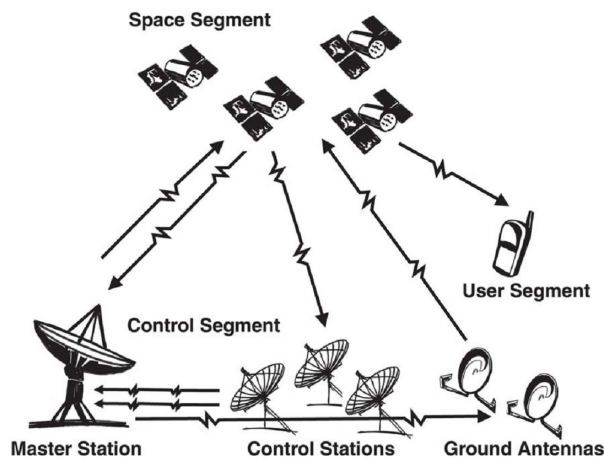


Figure 1.1. GPS System Architecture [GPSb]

The user segment includes all ground and air vehicles that use GPS as a navigational tool. They are equipped with at least a single GPS antenna and receiver. Finally, the ground control segment consists of monitoring stations that are responsible for monitoring and maintaining the health of the satellites, and commanding periodic maneuvers to maintain their orbits. Control stations also estimate and upload orbit ephemeris and SV clock parameters to the satellite, for broadcast to users

in the navigation message [ME06].

The broadcast navigation message includes orbit ephemeris parameters. Ephemeris parameters are used to determine satellite position. SV position must be known, in order to determine user position using the trilateration technique. Each SV also broadcasts an almanac of approximate ephemeris parameters for all space vehicles. The navigation message repeats every 12.5 minutes.

#### 1.1.1.1 GPS Signals and Receivers.

The structure of GPS signals is key to the passive nature of the system. All satellites transmit signals on the same frequency, called the carrier frequency. Receivers are able to distinguish between the various satellites using Code Division Multiple Access (CDMA) signal design. The CDMA is enabled by the use of pseudorandom noise (PRN) code sequences. PRN allows a receiver to pick out the signal from a desired SV in the presence of noise. This allows GPS to operate using low signal power relative to the electro-magnetic background noise. More information on satellite tracking and signal acquisition is available in [ME06].

Receivers essentially duplicate and match the code signal of the desired satellite in order to extract its signal from the noise. In this process, the carrier signal is extracted as well. When acquiring a SV signal, the receiver “locks” onto it and tracks it continuously. Each satellite transmits its own code modulated on top of the carrier wave. In fact, there are two carrier frequencies, denoted as L1 and L2.

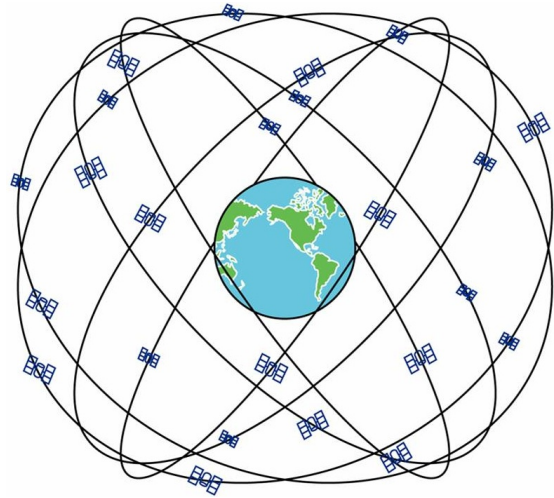


Figure 1.2. GPS Satellite Constellation [GPSa]

The L1 frequency is 1575.42 MHz and L2 is 1227.60 MHz. The L1 is in a protected aeronautical radio navigation systems (ARNS) band and is available to civilian users. The L2 frequency is for military use and is not in a protected band. The L1 frequency carries the coarse acquisition (C/A) code as well as the military P(Y) encrypted signal. The L2 frequency only carries the encrypted signals, which civilians are unable to access. But, civil users are free to make use of the L2 carrier itself.

GPS positioning is based upon trilateration. Both code and carrier phase signals are available to the user, but the GPS system was designed with the intention that the code phase would be used as a range measurement. Positioning using code measurements is called standalone GPS positioning. Measurements from at least 4 satellites are necessary to estimate user three-dimensional position and receiver clock error.<sup>2</sup> The carrier phase can also be used for positioning. However, an integer bias (also called a cycle ambiguity) affects each SV carrier phase signal because of the unknown number of complete carrier wavelength cycles between the user and SV. Despite the presence of cycle ambiguities, it is desirable to use carrier phase measurements for applications requiring high accuracy because tracking noise is 100 times lower for carrier than it is for code [ME06].

**1.1.2 Sources of Error.** The ranging accuracy of GPS measurements is limited by error sources. Below, we describe some of the most common sources of GPS errors.

**Receiver clock :** GPS precision hinges upon precisely synchronized SVs and user clocks. To keep GPS receivers compact and low-cost, receivers are normally fitted with inexpensive quartz clocks. Not knowing the precise travel time of the GPS signal from SV to receiver results in inaccurate ranging measurement. Because the receiver clock error is unknown and not easy to correct for, it

---

<sup>2</sup>Receiver clock error is discussed in Section 1.1.2

is usually estimated along with the three position coordinates. This means a fourth satellite is necessary for combined position and time estimation. The GPS constellation was designed to ensure continuous global coverage of four or more SVs. Therefore, receiver clock error is often referred to as a nuisance parameter rather than a source of error.

**Satellite clock** : Contrary to user clocks, satellites are equipped with atomic clocks. However, even with their high precision, they still cannot all be perfectly synchronized. Again, because accurate signal travel time is required, the satellite clock bias is monitored by the control segment. Control stations estimate the bias and upload corrections to the SV, for broadcast to users in the navigation message. Nevertheless, residual errors at the meter level remain.

**Receiver noise** : Receiver noise is the term used to describe the noise in measurements due to receiver hardware imperfection. Receiver noise can be caused by thermal noise in antennas, cables and other connections.

**Multipath** : Multipath error is the result of signal reflections off nearby surfaces. Since these reflections arrive at a slightly different time than the direct signal, they interfere with the receiver's ability to reliably extract the code or carrier signal from the surrounding background noise.

**Ionosphere** : The ionosphere (iono for short) is a layer of charged atmosphere at altitudes ranging from about 50-1000 km above the earth's surface. The electrons in the ionosphere are excited by solar activity. So, the ionosphere is more active during the daytime than at night. In addition, the ionosphere is dispersive, which means that it affects various signal frequencies differently. It delays the code signal and advances carrier signals. This is the largest GPS error source.

**Troposphere** : The lower atmosphere from sea level to roughly 10 km altitude is called the troposphere (tropo for short). The tropospheric error is the same on both the carrier and code signals. Weather conditions impact the tropo error.

**Nominal Ephemeris** : The nominal ephemeris error is the result of inaccuracies in the broadcast orbit ephemeris parameters. This nominal error is (usually) approximately at the meter level and should not be confused with the much more hazardous condition of orbit ephemeris fault. The fault is discussed in Section 3.4.

**Other** : Other errors include carrier phase wind-up, interfrequency biases, receiver antenna phase center variation. Phase center variation can be calibrated with negligibly small residual error. The other errors cancel entirely using the differential techniques used in this work, and they will not be discussed further.

**1.1.3 Navigation Performance Metrics.** Navigation system performance is quantified using the metrics listed below.

**Accuracy** : Accuracy is a measure of the navigation system output deviation from the truth, under fault-free conditions. It is often specified in terms of a 95% confidence level.

**Integrity risk** : Integrity risk is the probability of a navigation system error or fault that results in hazardous misleading information.

**Continuity risk** : Continuity risk is the probability of a detected but unscheduled navigation function interruption after an operation has been initiated.

**Availability** : Availability is the fraction of time the navigation system is useable (as defined by its compliance with accuracy, integrity, and continuity requirements) before the operation is initiated.

Application-specific requirements are set that specify the required level of accuracy, integrity and continuity. We will discuss the requirements set forth in our benchmark application in Section 6.1.

## 1.2 High Accuracy and High Integrity Applications

GPS is implemented in a wide variety of applications ranging from pedestrian (personal) navigation to very demanding military uses. As mentioned earlier, this work focuses on rendezvous applications requiring both high accuracy and high integrity. Such applications require differential GPS.

**1.2.1 Carrier Phase Differential GPS (CPDGPS).** In high accuracy applications, it is necessary to use carrier phase differential GPS (CPDGPS) in order to meet mission requirements. Carrier phase measurements are able to provide the necessary accuracy because carrier measurement tracking noise is 100 times lower than for code measurements.

Also, using differential GPS aids in eliminating ranging measurement errors. In differential implementations, there is a reference receiver in addition to the user receiver. Depending on the system design, the reference receiver may either broadcast range corrections to the user, or directly broadcast measurements. The latter will be considered throughout the remainder of this work. The advantage of differential GPS is that the satellite clock bias can be completely eliminated. The details of differential GPS implementation will be shown in Chapter 2. In addition, if the user is within roughly 10 miles of the reference antenna, the largest part of the ionospheric and tropospheric errors can be removed due to the fact that they are correlated between user and reference antennas [ME06]. But, iono and tropo decorrelation errors remain, and they increase as the separation between user and reference is increased. One practical constraint of differential GPS is that a data link between

user and reference receivers is necessary for communication. The ‘broadcast radius’ is the maximum distance from the reference receiver where it is still possible to establish communication for a given data link.

Carrier phase differential GPS (CPDGPS) improves positioning accuracy. Further improvement is obtained by exploiting the integer nature of the carrier phase cycle ambiguities. In this regard, cycle ambiguity resolution processes, including the Enforced Position-Domain Integrity-Risk Cycle Resolution Algorithm (EPIC-Light) [KP10] which is used in this work, provide the ultimate GPS-based positioning accuracy.

**1.2.2 Prior Work on Integrity Monitoring in CPDGPS.** GPS measurement faults are unusually large errors that can cause a significant error in the position estimate. This can produce hazardous information (HI) for the user and affect mission integrity. In response, fault detection algorithms have been designed and implemented. If the fault is not detected, it can result in hazardously misleading information (HMI). In other words, the hazardous information is misleading in that the user is not aware of the hazard.

There are numerous existing algorithms for fault detection. Some are able to detect orbit ephemeris faults (OEF), and others are used to detect atmospheric anomalies. For example, a monitor for ionospheric fronts is proposed in [GP06]. Orbit ephemeris fault detection is the focus of this work. (OEFs are discussed in Section 3.4.) OEF monitoring algorithms can be either user-based or reference receiver-based.

Monitors have been developed for the local area augmentation system (LAAS) that are able to detect orbit ephemeris faults. However, the monitor presented in [PG05] can not detect all types of OEFs. Another monitor exists, that is able to detect all types of OEF, but requires a static (land based) reference antenna with

known location [TPE<sup>+</sup>10]. This monitor would not be practical for the rendezvous applications considered in Chapter 6 of this work. In response, a reference station monitor is developed in [JSKP] that does not require a stationary antenna. Similar to the LAAS monitor, it cannot detect all types of orbit ephemeris faults.

**1.2.3 Contributions.** As an alternative, this work investigates OEF detection for rendezvous applications using Receiver Autonomous Integrity Monitoring (RAIM), which is user-based. Specifically, the relative RAIM (RRAIM) algorithm is investigated. RRAIM is introduced in [HP04], and has been implemented in [GJP]. Unfortunately, RRAIM cannot be directly implemented in rendezvous applications requiring both high accuracy and high integrity, and in which user and reference are in constant motion relative to the earth. Therefore, the main contributions of this work can be described as follows.

In Chapter 3 of this thesis, iono, tropo, and multipath measurement error models are updated to rigorously account for measurement error time-correlation, as well as spatial correlation between signals at user and reference receivers.

In Chapter 4, a major challenge in measurement monitoring is addressed, which is the integrity risk evaluation. Chapter 4 shows that the RRAIM detection test statistic is correlated with the position estimate error, which prevents direct integrity risk evaluation using RRAIM. In response, the Unified RAIM (URAIM) concept is developed which unifies RRAIM and Differential RAIM (DRAIM) into a single algorithm.

In addition, in Chapter 5, carrier phase cycle ambiguity resolution is investigated because it is needed to achieve stringent accuracy requirements. The EPIC-Light [KP10] integrity risk bounding method is modified to account for the combined positioning impact of incorrect cycle ambiguity fixes and of undetected OEF using

URAIM.

Finally, in Chapter 6, the performance of URAIM using EPIC-Light is quantified and analyzed globally, for the benchmark rendezvous application of shipboard landing of aircraft.

## CHAPTER 2

### RELATIVE POSITIONING AND CYCLE RESOLUTION ALGORITHMS

This chapter introduces an example GPS carrier-phase based measurement processing method that has been shown in [Kha08] to provide high accuracy and high integrity navigation. First, the differential carrier-phase-based positioning algorithm is described. Then, the integer fixing procedure is introduced and two different methods used to bound fault-free integrity risk are discussed. Subsequent chapters will build upon the previous work presented in this chapter. In particular, the integrity risk bounding methods are modified in Chapter 5 to allow integrity risk evaluation in the presence of faults.

#### 2.1 Carrier Phase Differential GPS

This section introduces code and carrier phase differential measurements at L1 and L2 frequencies, and combines them to form the measurement equation used for positioning in our benchmark application. All measurements taken at the current time (i.e. current epoch).

**2.1.1 Differential Measurements.** To begin, raw code and carrier measurements for a single space vehicle  $i$  (denoted using left superscript  $i$ ) are presented. The raw (meaning unmodified or unprocessed) measurement obtained at the receiver is a function of true range to the SV  ${}^i r$  plus a number of terms corresponding to errors [ME06] [Kha08]. The code phase measurement is shown below in equation 2.1, which is expressed in units of length.

$${}^i \rho_{\square} = {}^i r + c\delta t_u - c^i \delta t_s + {}^i \delta x_{eph} + {}^i v_{\rho_{\square}} \quad (2.1)$$

$$\text{with: } {}^i v_{\rho_{\square}} := {}^i \varepsilon_{\rho_{\square}} + \frac{\lambda_{\square}^2}{\lambda_{L1}^2} {}^i I + {}^i T$$

where,

${}^i \rho_{\square}$  : code measurement for SV  $i$ , where  $\square$  represents frequency (at either L1 or L2)

${}^i r$  : range to satellite  $i$

$c$  : speed of light (m/s)

$\delta t_u$  : user clock error (s)

$\delta t_s$  : satellite clock error (s)

${}^i \delta x_{eph}$  : nominal ephemeris error for SV  $i$

${}^i v_{\rho_{\square}}$  : remaining code measurement errors

${}^i \varepsilon_{\rho_{\square}}$  : code receiver noise and multipath error for SV  $i$

${}^i I$  : impact of ionosphere on measurements at L1 frequency for SV  $i$

${}^i T$  : tropospheric error for SV  $i$

Note that the clock errors and orbit ephemeris are shown explicitly whereas the remaining terms are grouped into  ${}^i v_{\rho_{\square}}$  to simplify notation for future derivations. Similarly, the carrier phase measurement (expressed in units of length) may be written as follows,

$${}^i \phi_{\square} = {}^i r + \lambda_{\square} {}^i n_{\square} + c \delta t_u - c \delta t_s + {}^i \delta x_{eph} + {}^i v_{\phi_{\square}} \quad (2.2)$$

$$\text{with: } {}^i v_{\phi_{\square}} := {}^i \varepsilon_{\phi_{\square}} + \frac{-\lambda_{\square}^2}{\lambda_{L1}^2} {}^i I + {}^i T$$

where,

${}^i \phi_{\square}$  : carrier measurement for SV  $i$

$\lambda_{\square}$  : carrier wavelength

${}^i n_{\square}$  : integer/cycle ambiguity

${}^i v_{\phi_{\square}}$  : remaining carrier measurement errors

${}^i \varepsilon_{\phi_{\square}}$  : carrier receiver noise and multipath error for SV  $i$

Again, the receiver noise and multipath  ${}^i\varepsilon_{\phi_{\square}}$ , ionospheric error  $\frac{-\lambda_{\square}^2}{\lambda_{L1}^2}{}^iI$ , and tropospheric error  ${}^iT$  are grouped into the  ${}^iv_{\phi_{\square}}$  term.

Differential carrier phase measurements are formed by subtracting user from reference measurements. This is denoted with the addition of subscript  $SD$  as presented in equation 2.3. Since the satellite clock bias  ${}^i\delta t_s$  and nominal ephemeris error  ${}^i\delta x_{eph}$  are common to both user and reference measurements, differencing them eliminates these errors.

$${}^i\phi_{\square,SD} = {}^ir_{SD} + \lambda_{\square}{}^in_{\square,SD} + c\delta t_{u,SD} + {}^iv_{\phi_{\square,SD}} \quad (2.3)$$

User and reference receivers are considered to be in close proximity to each other, with separation assumed to be less than 15 nmi (nautical miles) for the benchmark application. Since GPS satellites are in medium earth orbit, the lines of sight (LOS) to a satellite for the user and reference receivers are parallel. This means that user and reference receivers have the same LOS vectors. Referring to Figure 2.1 the differential range  ${}^ir_{SD}$  may be written as a function of the LOS vector  ${}^ie$  and position vector  $\mathbf{x}$ . Equation 2.3 then becomes

$${}^i\phi_{\square,SD} = {}^ie^T\mathbf{x} + \lambda_{\square}{}^in_{\square,SD} + c\delta t_{u,SD} + {}^iv_{\phi_{\square,SD}} \quad (2.4)$$

where,

${}^ie$  : line of sight from receiver to SV  $i$

$\mathbf{x}$  : position state vector

The measurements are now stacked for all SVs in view ( $n$  of them). It is worth noting that boldface notation is used for vectors. So, the stacked SD measurement vector is

$$\boldsymbol{\phi}_{\square,SD} = \left[ {}^1\phi_{\square,SD} \quad \cdots \quad {}^i\phi_{\square,SD} \quad \cdots \quad {}^n\phi_{\square,SD} \right]^T \quad (2.5)$$

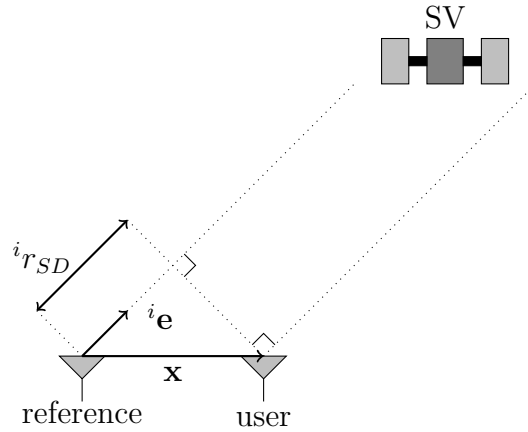


Figure 2.1. Relative Positioning

The single difference cycle ambiguities  ${}^i n_{\square,SD}$ , user clock error  $\delta t_{u,SD}$  and measurement error  ${}^i v_{\phi_{\square,SD}}$  may be stacked in a similar fashion. Equation 2.4 is written for all SVs as,

$$\phi_{\square,SD} = \begin{bmatrix} \mathbf{e}^T \end{bmatrix} \mathbf{x} + \lambda_{\square} \mathbf{n}_{\square,SD} + c \begin{bmatrix} \mathbf{1} \end{bmatrix} \delta t_{u,SD} + \mathbf{v}_{\phi_{\square,SD}} \quad (2.6)$$

where,

$\begin{bmatrix} \mathbf{e}^T \end{bmatrix}$  : matrix containing LOS vectors to each SV as rows

i.e.  $\begin{bmatrix} {}^1 \mathbf{e} & \dots & {}^i \mathbf{e} & \dots & {}^n \mathbf{e} \end{bmatrix}^T$

$\begin{bmatrix} \mathbf{1} \end{bmatrix}$  : = vector of ones, i.e.  $\begin{bmatrix} 1 & \dots & 1 \end{bmatrix}^T \in \mathbb{R}^{n \times 1}$

There are  $n$  cycle ambiguities  $\mathbf{n}_{\square,SD}$  to deal with as well as the receiver clock error  $\delta t_{u,SD}$ . Differencing these measurements again, but with respect to the measurement of a master SV this time, gives the carrier phase double difference (DD) measurement equation 2.8. The master SV is typically chosen to be the SV with the highest elevation, but any satellite can be chosen (for consistency defined to be SV 1). The subscript  $DD$  is used to denote double difference. So, the DD measurement vector is

$$\phi_{\square,DD} = \begin{bmatrix} {}^2 \phi_{\square,SD} - {}^1 \phi_{\square,SD} & \dots & {}^i \phi_{\square,SD} - {}^1 \phi_{\square,SD} & \dots & {}^n \phi_{\square,SD} - {}^1 \phi_{\square,SD} \end{bmatrix}^T \quad (2.7)$$

From equation 2.6, we obtain

$$\phi_{\square,DD} = \mathbf{G}\mathbf{x} + \lambda_{\square}\mathbf{n}_{\square,DD} + \mathbf{v}_{\phi_{\square}} \quad (2.8)$$

$$\text{where: } \mathbf{G} := \begin{bmatrix} 2\mathbf{e} - 1\mathbf{e} & \dots & i\mathbf{e} - 1\mathbf{e} & \dots & n\mathbf{e} - 1\mathbf{e} \end{bmatrix}^T$$

where,

$\mathbf{G}$  : matrix containing differenced LOS vectors as rows;  $\mathbf{G} \in \mathbb{R}^{(n-1) \times 3}$

The same procedure may be used to create double difference code measurements [ME06]. Since double difference measurements are used throughout the remainder of this work, the  $DD$  subscript will be dropped for clarity of notation. In cases where raw measurements are needed, it will be stated explicitly.

The current-time set of carrier phase measurements in equation 2.8 is insufficient for precise estimation since we need to estimate both position and cycle ambiguities. There are several options. We can either wait to accumulate more measurements over time. Or, another option is to include other measurements, or combinations of measurements. Following [Kha08], we include geometry free measurements.

**2.1.2 Geometry Free Measurements.** The geometry free (GF) measurement is a combination of code and carrier measurements, which eliminates the satellite geometry. To be more specific, this is accomplished by subtracting narrow-lane (NL) code from wide-lane (WL) carrier measurements [Kha08]. First, WL carrier and NL code are formed using raw measurements.

**2.1.2.1 Wide lane carrier phase.** To form the WL carrier, the raw carrier measurement for SV  $i$  at L1 and L2 frequencies is first expressed in units of (L1 and L2) cycles.

$$\begin{aligned} \frac{{}^i\phi_{L1}}{\lambda_{L1}} &= {}^i n_{L1} + \frac{1}{\lambda_{L1}} \{ {}^i r + c\delta t_u - c^i\delta t_s + {}^i v_{\phi_{L1}} \} \\ \frac{{}^i\phi_{L2}}{\lambda_{L2}} &= {}^i n_{L2} + \frac{1}{\lambda_{L2}} \{ {}^i r + c\delta t_u - c^i\delta t_s + {}^i v_{\phi_{L2}} \} \end{aligned}$$

The wide-lane carrier phase measurement (expressed in units of WL cycles) is formed by subtracting the carrier phase measurement at L2 frequency from the measurement at L1 frequency [Kha08]. It is defined as,

$$\begin{aligned}
\frac{{}^i\phi_w}{\lambda_w} &:= \frac{{}^i\phi_{L1}}{\lambda_{L1}} - \frac{{}^i\phi_{L2}}{\lambda_{L2}} \\
&= ({}^i n_{L1} - {}^i n_{L2}) + \left( \frac{1}{\lambda_{L1}} - \frac{1}{\lambda_{L2}} \right) \{ {}^i r + c\delta t_u - c^i \delta t_s \} + \frac{{}^i v_{\phi_{L1}}}{\lambda_{L1}} - \frac{{}^i v_{\phi_{L2}}}{\lambda_{L2}} \\
&= {}^i n_w + \frac{1}{\lambda_w} \{ {}^i r + c\delta t_u - c^i \delta t_s \} + \frac{{}^i v_{\phi_{L1}}}{\lambda_{L1}} - \frac{{}^i v_{\phi_{L2}}}{\lambda_{L2}} \\
&\quad \text{where, } \lambda_w := \frac{\lambda_{L1}\lambda_{L2}}{\lambda_{L2} - \lambda_{L1}} \quad \text{and} \quad {}^i n_w := {}^i n_{L1} - {}^i n_{L2}
\end{aligned} \tag{2.9}$$

The wide lane carrier is expressed in units of length as,

$$\begin{aligned}
{}^i\phi_w &= \lambda_w {}^i n_w + \{ {}^i r + c\delta t_u - c^i \delta t_s \} + {}^i v_{\phi_w} \\
&\quad \text{where, } {}^i v_{\phi_w} := \lambda_w \left( \frac{{}^i v_{\phi_{L1}}}{\lambda_{L1}} - \frac{{}^i v_{\phi_{L2}}}{\lambda_{L2}} \right)
\end{aligned} \tag{2.10}$$

**2.1.2.2 Narrow lane code phase.** To form the NL code, the raw code measurement for SV  $i$  at L1 and L2 frequencies is first expressed in units of cycles.

$$\begin{aligned}
\frac{{}^i\rho_{L1}}{\lambda_{L1}} &= \frac{1}{\lambda_{L1}} \{ {}^i r + c\delta t_u - c^i \delta t_s + {}^i v_{\rho_{L1}} \} \\
\frac{{}^i\rho_{L2}}{\lambda_{L2}} &= \frac{1}{\lambda_{L2}} \{ {}^i r + c\delta t_u - c^i \delta t_s + {}^i v_{\rho_{L2}} \}
\end{aligned}$$

The narrow-lane code phase measurement is formed by summing the raw code phase measurements at L1 and L2 frequencies [Kha08]. It is defined as,

$$\begin{aligned}
\frac{{}^i\rho_n}{\lambda_n} &= \frac{{}^i\rho_{L1}}{\lambda_{L1}} + \frac{{}^i\rho_{L2}}{\lambda_{L2}} \\
&= \left( \frac{1}{\lambda_{L1}} + \frac{1}{\lambda_{L2}} \right) \{ {}^i r + c\delta t_u - c^i \delta t_s \} + \frac{{}^i v_{\rho_{L1}}}{\lambda_{L1}} + \frac{{}^i v_{\rho_{L2}}}{\lambda_{L2}} \\
&= \frac{1}{\lambda_n} \{ {}^i r + c\delta t_u - c^i \delta t_s \} + \frac{{}^i v_{\rho_{L1}}}{\lambda_{L1}} + \frac{{}^i v_{\rho_{L2}}}{\lambda_{L2}} \\
&\quad \text{where: } \lambda_n = \frac{\lambda_{L1}\lambda_{L2}}{\lambda_{L1} + \lambda_{L2}}
\end{aligned} \tag{2.11}$$

The narrow lane code is expressed in units of length as,

$${}^i\rho_n = \{ {}^i r + c\delta t_u - c^i \delta t_s \} + {}^i v_{\rho_n} \tag{2.12}$$

$$\text{where, } \quad {}^i v_{\rho_n} := \lambda_n \left( \frac{{}^i v_{\rho_{L1}}}{\lambda_{L1}} + \frac{{}^i v_{\rho_{L2}}}{\lambda_{L2}} \right)$$

**2.1.2.3 Combining to form GF Measurement.** To form the raw GF measurement, NL code is subtracted from WL carrier (where both measurements are expressed in units of length). Subtracting equation 2.12 from 2.10 results in,

$$\begin{aligned} \lambda_w {}^i z_{GF} &:= {}^i \phi_w - {}^i \rho_n \\ &= \lambda_w {}^i n_w + \lambda_w \left( \frac{{}^i v_{\phi_{L1}}}{\lambda_{L1}} - \frac{{}^i v_{\phi_{L2}}}{\lambda_{L2}} \right) - \lambda_n \left( \frac{{}^i v_{\rho_{L1}}}{\lambda_{L1}} + \frac{{}^i v_{\rho_{L2}}}{\lambda_{L2}} \right) \\ &= \lambda_w {}^i n_w + \lambda_w {}^i v_{GF} \end{aligned} \quad (2.13)$$

$$\text{where: } \quad {}^i v_{GF} = \left( \frac{{}^i v_{\phi_{L1}}}{\lambda_{L1}} - \frac{{}^i v_{\phi_{L2}}}{\lambda_{L2}} \right) - \frac{\lambda_n}{\lambda_w} \left( \frac{{}^i v_{\rho_{L1}}}{\lambda_{L1}} + \frac{{}^i v_{\rho_{L2}}}{\lambda_{L2}} \right)$$

Equation 2.13 may be expressed in units of cycles by dividing the equation by  $\lambda_w$ . Then, stacking for all SVs ( $i = 1 \dots n$ ) we obtain,

$$\mathbf{z}_{GF} = \mathbf{n}_w + \mathbf{v}_{GF} \quad (2.14)$$

$$\text{where: } \quad \mathbf{v}_{GF} = \left( \frac{\mathbf{v}_{\phi,L1}}{\lambda_{L1}} - \frac{\mathbf{v}_{\phi,L2}}{\lambda_{L2}} \right) - \frac{\lambda_n}{\lambda_w} \left( \frac{\mathbf{v}_{\rho,L1}}{\lambda_{L1}} + \frac{\mathbf{v}_{\rho,L2}}{\lambda_{L2}} \right)$$

The GF measurement is a noisy but direct measure of the cycle ambiguities. Also, it can be shown that ionospheric and tropospheric errors are eliminated [Kha08].

These GF measurements are also double differenced in the same manner as carrier measurements. In addition, both the user and reference in our benchmark application filter these measurements for a period of time before rendezvous. The filtering period and its implication are discussed in Chapter 3. For now, it is enough to know that GF measurements are filtered over time using a running average. When the user enters the broadcast radius, it is possible to use differential GPS and double difference these GF measurements for use in relative position estimation.

**2.1.3 Positioning Algorithm for Benchmark Application.** Having defined both carrier and geometry free measurements, it is now possible to construct the

measurement equation used in our benchmark application [Kha08]. The measurement equation used for position estimation is given by,

$$\begin{bmatrix} \mathbf{z}_{GF} \\ \phi_w \end{bmatrix} = \begin{bmatrix} \mathbf{0} & \mathbf{I} \\ \mathbf{G} & \lambda_w \mathbf{I} \end{bmatrix} \begin{bmatrix} \mathbf{x} \\ \mathbf{n}_w \end{bmatrix} + \begin{bmatrix} \mathbf{v}_{GF} \\ \mathbf{v}_{\phi,w} \end{bmatrix} \quad (2.15)$$

Filtered geometry free measurements  $\mathbf{z}_{GF}$  are expressed in cycles. The double differenced WL carrier phase measurements  $\phi_w$  are expressed in units of length. An alternative implementation uses carrier measurements at L1 and L2 frequencies as shown in equation 2.16 [Kha08].

$$\begin{bmatrix} \mathbf{z}_{GF} \\ \phi_{L1} \\ \phi_{L2} \end{bmatrix} = \begin{bmatrix} \mathbf{0} & \mathbf{I} & -\mathbf{I} \\ \mathbf{G} & \lambda_{L1} \mathbf{I} & \mathbf{0} \\ \mathbf{G} & \mathbf{0} & \lambda_{L2} \mathbf{I} \end{bmatrix} \begin{bmatrix} \mathbf{x} \\ \mathbf{n}_{L1} \\ \mathbf{n}_{L2} \end{bmatrix} + \begin{bmatrix} \mathbf{v}_{GF} \\ \mathbf{v}_{\phi,L1} \\ \mathbf{v}_{\phi,L2} \end{bmatrix} \quad (2.16)$$

If we wish to not yet specify which implementation we want to consider, the measurement equation for estimation may be written as,

$$\begin{bmatrix} \mathbf{z}_{GF} \\ \phi \end{bmatrix} = \begin{bmatrix} \mathbf{0} & \mathbf{D}_{GF} \\ \mathbf{G} & \mathbf{D}_{\phi} \end{bmatrix} \begin{bmatrix} \mathbf{x} \\ \mathbf{n} \end{bmatrix} + \begin{bmatrix} \mathbf{v}_{GF} \\ \mathbf{v}_{\phi} \end{bmatrix} \quad (2.17)$$

where,

$\phi$  : DD carrier phase measurements (either WL, or L1 and L2 frequencies)

$\mathbf{n}$  : DD cycle ambiguities (either WL, or L1 and L2 frequencies)

$\mathbf{v}_{\phi}$  : DD measurement noise (either WL, or L1 and L2 frequencies)

$\mathbf{G}$  : sub-matrix containing LOS vectors as rows (stacked twice for L1 and L2 frequencies)

$\mathbf{D}_{GF}$  : sub-matrix corresponding to GF cycle ambiguities

$\mathbf{D}_{\phi}$  : sub-matrix corresponding to DD carrier phase ambiguities

Measurement equation 2.17 is expressed in the form of a standard linear measurement equation,

$$\mathbf{z} = \mathbf{H}\mathbf{u} + \mathbf{v} \quad (2.18)$$

where,

$\mathbf{z}$  : measurement vector

$\mathbf{H}$  : observation matrix

$\mathbf{u}$  : state vector

$\mathbf{v}$  : measurement error vector

The measurement noise is assumed to be Gaussian distributed with a mean  $\mathbf{b}$  and covariance matrix  $\mathbf{V}$  (i.e.  $\mathbf{v} \sim N(\mathbf{b}, \mathbf{V})$ ). Equation 2.18 is in state space form. It is commonly called the output equation in control theory. The objective is to observe/estimate the states  $\mathbf{u}$  (in this case, position coordinates and cycle ambiguities) using an observer/estimator. The estimator used in this work is a weighted least squares (WLS) estimator. Assuming Gaussian distributed errors, the WLS estimator minimizes the sum of squares of the diagonal components of the state estimate covariance. In this case, it is equivalent to the maximum likelihood estimator. The state estimate vector and estimate-covariance matrix are given below for the WLS estimator,

$$\hat{\mathbf{u}} = \mathbf{S}\mathbf{z} \quad (2.19)$$

$$\hat{\mathbf{P}} = (\mathbf{H}^T \mathbf{V}^{-1} \mathbf{H})^{-1} \quad \text{invertible if: } n > m \text{ for } \mathbf{H} \in \mathbb{R}^{n \times m} \quad (2.20)$$

where,

$\hat{\mathbf{u}}$  : state estimate vector

$\hat{\mathbf{P}}$  : estimate covariance matrix

$\mathbf{S}$  : weighted pseudoinverse, where  $\mathbf{S} = (\mathbf{H}^T \mathbf{V}^{-1} \mathbf{H})^{-1} \mathbf{H}^T \mathbf{V}^{-1}$

The estimate error  $\delta \mathbf{u}$  is defined as the difference between estimated and true state values [ME06],

$$\delta \mathbf{u} = \hat{\mathbf{u}} - \mathbf{u} = \mathbf{S}\mathbf{v} \quad (2.21)$$

where,

$\delta \mathbf{u}$  : estimate error vector

The error vector,  $\delta\mathbf{u}$ , will subsequently be used to assess system performance.

## 2.2 Integrity in Cycle Ambiguity Resolution

Least Squares estimation is referred to as float estimation in this work. This is because the cycle ambiguities are treated as real numbers by the Least Squares estimator, which is sufficient for many applications [ME06]. However, because high accuracy is desired, we can take advantage of the additional knowledge that the cycle ambiguities are integers. If they are constrained to be integers (either in the estimation process, or afterwards) the additional information will improve the position solution.

There are multiple methods to fix cycle ambiguities to integer values. The focus of this work is directed toward the bootstrap fixing method. This procedure is preferred in our situation because ambiguities can be fixed sequentially. This method provides significant freedom in implementation in that we can choose to fix all ambiguities, or a subset [Teu01a].

**2.2.1 Integer Fixing Procedure.** The bootstrap integer fixing method is shown below in equation 2.22. Note that the procedure is sequential, which is computationally efficient.

$$\check{\mathbf{u}}_k = \check{\mathbf{u}}_{k-1} + \mathbf{K}_k(\langle \mathbf{H}_k \check{\mathbf{u}}_{k-1} \rangle - \mathbf{H}_k \check{\mathbf{u}}_{k-1}) \quad (2.22)$$

$$\text{where : } \mathbf{H}_k = \begin{bmatrix} \mathbf{0} & \mathbf{Z}_{:,k}^T \end{bmatrix} \in \mathbb{R}^{1 \times m}$$

$$\mathbf{K}_k = \mathbf{P}_{k-1} \mathbf{H}_k^T (\mathbf{H}_k \mathbf{P}_{k-1} \mathbf{H}_k^T)^{-1} \in \mathbb{R}^{m \times 1}$$

$$\mathbf{P}_k = \mathbf{P}_{k-1} - \mathbf{K}_k (\mathbf{H}_k \mathbf{P}_{k-1} \mathbf{H}_k^T) \mathbf{K}_k^T \in \mathbb{R}^{m \times m}$$

Here,  $\check{\mathbf{u}}_k$  is the fixed state vector at the current iteration where  $k$  denotes the number of fixed integers. The notation  $\langle \rangle$  is used to represent the rounding procedure. In addition,  $\mathbf{Z}^T$  is an integer transformation matrix, where the notation  $\mathbf{Z}_{:,k}$  denotes the  $k^{\text{th}}$  column vector of matrix  $\mathbf{Z}$ . The simplest choice is to use the identity matrix ( $\mathbf{Z}^T =$

I). Another option is to use the least-square ambiguity decorrelation adjustment (LAMBDA) method [Teu98]. The LAMBDA procedure facilitates fixing by providing a decorrelated ambiguity covariance matrix, which may be used to sort the integers according to their likelihood of correct fix. So, we can fix the ‘easiest-to-fix’ integers first. Also,  $\mathbf{K}_k$  is the gain and  $\mathbf{P}_k$  is the updated state covariance matrix after fixing.

In equation 2.22, the rounding procedure is written as an update on the previous fixed state vector  $\check{\mathbf{u}}_{k-1}$ . An alternative representation can be written as a function of the float state vector  $\hat{\mathbf{u}}$  as follows,

$$\check{\mathbf{u}}_k = \hat{\mathbf{u}} + \mathbf{K}_{kk}(\langle \mathbf{H}_{kk} \hat{\mathbf{u}} \rangle - \mathbf{H}_{kk} \hat{\mathbf{u}}) \quad (2.23)$$

$$\text{where : } \mathbf{H}_{kk} = \begin{bmatrix} \mathbf{0} & \mathbf{Z}_{:,1:k}^T \end{bmatrix} \in \mathbb{R}^{k \times m}$$

$$\mathbf{K}_{kk} = \hat{\mathbf{P}} \mathbf{H}_{kk}^T (\mathbf{H}_{kk} \hat{\mathbf{P}} \mathbf{H}_{kk}^T)^{-1} \in \mathbb{R}^{m \times k}$$

$$\mathbf{P}_k = \hat{\mathbf{P}} - \mathbf{K}_{kk} (\mathbf{H}_{kk} \hat{\mathbf{P}} \mathbf{H}_{kk}^T)^{-1} \mathbf{K}_{kk}^T \in \mathbb{R}^{m \times m}$$

where  $\mathbf{Z}_{:,1:k}$  denotes the first  $k$  columns of matrix  $\mathbf{Z}$ .

Following the rounding procedure, the position states are still Gaussian distributed; however, because of rounding, ambiguities are no longer Gaussian. We will see a new ambiguity distribution when computing integrity risk [KP10].

**2.2.2 Integrity Risk Requirement.** Integrity risk may be thought of as the probability of being in a hazardous situation, and being unaware that it is hazardous. This is called having hazardous misleading information (HMI). Using this definition, we can write an expression for the integrity risk  $I_R$  as,  $I_R = P(HMI)$ ; where  $P(HMI)$  is the probability of HMI. Using the laws of mutually exclusive and conditional probabilities the integrity risk can be written in terms of fault-free and faulted hypotheses.

$$I_R = \underbrace{P(HMI | \bar{F})}_{\text{Chapter 2}} P(\bar{F}) + \underbrace{P(HMI | F)}_{\text{Chapter 5}} P(F) \quad (2.24)$$

where,

$I_R$  : integrity risk

$P(HMI | \bar{F})$  : probability of HMI under fault free ( $\bar{F}$ ) hypothesis

$P(\bar{F})$  : prior probability fault free hypothesis

$P(HMI | F)$  : probability of HMI under faulted ( $F$ ) hypothesis

$P(F)$  : prior probability of faulted hypothesis

The symbol  $|$  is the notation used to signify ‘given’. In addition, when cycle ambiguities are fixed, an infinite number of fix hypotheses are generated (one for each fix candidate  $\boldsymbol{\eta}$ , since we cannot assume that the correct fix is always achieved.) The integrity risk assuming that  $k$  integers have been fixed is shown below, given that the fixed cycle ambiguity vector  $\check{\mathbf{n}}$  belongs to the  $k$  dimensional space of integers (i.e.  $\check{\mathbf{n}} \in \mathbb{Z}^k$ ).

$$\begin{aligned}
 I_R = P(\bar{F}) \sum_{\boldsymbol{\eta} \in \mathbb{Z}^k} P(HMI | \bar{F}, \boldsymbol{\eta}) P(\check{\mathbf{n}} = \boldsymbol{\eta} | \bar{F}) \\
 + P(F) \sum_{\boldsymbol{\eta} \in \mathbb{Z}^k} P(HMI | F, \boldsymbol{\eta}) P(\check{\mathbf{n}} = \boldsymbol{\eta} | F)
 \end{aligned} \tag{2.25}$$

where,

$P(\check{\mathbf{n}} = \boldsymbol{\eta})$  : probability of fixing to vector  $\boldsymbol{\eta}$

This involves considering an infinite number of fix candidates, which would be impossible to deal with. To make the computational load practical, two techniques have been developed in the past, both of which generate conservative bounds on the integrity risk [KP10]. One method is Bootstrap, and the other is EPIC-light. Since we have not discussed faults yet, we will develop these techniques for the fault free scenario and extend EPIC to the faulted scenario in Chapter 5.

### 2.3 Fault Free Integrity in Bootstrap Cycle Resolution

When using the bootstrap fixing algorithm, a single fix candidate is first chosen. This single fix candidate is often taken to be the correct fix  $\mathbf{o}$  (for reasons which

will become clear). For all remaining fixes in the integer space  $\mathbb{Z}^k$ , the probability of HMI is conservatively assumed to be one. That is, we assume if we do not fix correctly, we will be in a hazardous situation.

**2.3.1 Bootstrap Integrity Risk Bound.** The bootstrap integrity risk bound can be derived from equation 2.25. For the fault free case we have,

$$\begin{aligned}
P(HMI | \bar{F}) &:= \sum_{\boldsymbol{\eta} \in \mathbb{Z}^k} P(HMI | \bar{F}, \boldsymbol{\eta}) P(\check{\mathbf{n}} = \boldsymbol{\eta} | \bar{F}) \\
&= P(HMI | \bar{F}, \mathbf{o}) P(\check{\mathbf{n}} = \mathbf{o} | \bar{F}) \\
&\quad + \sum_{\substack{\boldsymbol{\eta} \in \mathbb{Z}^k \\ \boldsymbol{\eta} \neq \mathbf{o}}} \overset{1}{P}(HMI | \bar{F}, \boldsymbol{\eta}) P(\check{\mathbf{n}} = \boldsymbol{\eta} | \bar{F}) \\
&\leq P(HMI | \bar{F}, \mathbf{o}) P(\check{\mathbf{n}} = \mathbf{o} | \bar{F}) + \sum_{\substack{\boldsymbol{\eta} \in \mathbb{Z}^k \\ \boldsymbol{\eta} \neq \mathbf{o}}} P(\check{\mathbf{n}} = \boldsymbol{\eta} | \bar{F}) \tag{2.26}
\end{aligned}$$

where,

$\mathbf{o}$  : denotes the correct fix vector

A particular fix can either be either correct or incorrect. The fix hypotheses are mutually exclusive and exhaustive. Therefore, the substitution

$$\sum_{\substack{\boldsymbol{\eta} \in \mathbb{Z}^k \\ \boldsymbol{\eta} \neq \mathbf{o}}} P(\check{\mathbf{n}} = \boldsymbol{\eta} | \bar{F}) = 1 - P(\check{\mathbf{n}} = \mathbf{o} | \bar{F}) \tag{2.27}$$

is made in equation 2.26 to obtain,

$$\begin{aligned}
P(HMI | \bar{F}) &\leq P(HMI | \bar{F}, \mathbf{o}) P(\check{\mathbf{n}} = \mathbf{o} | \bar{F}) + 1 - P(\check{\mathbf{n}} = \mathbf{o} | \bar{F}) \\
&\leq 1 + \left( P(HMI | \bar{F}, \mathbf{o}) - 1 \right) P(\check{\mathbf{n}} = \mathbf{o} | \bar{F}) \tag{2.28}
\end{aligned}$$

So, using equation 2.28, we can compute a bound on the integrity risk if we are able to compute  $P(\check{\mathbf{n}} = \mathbf{o} | \bar{F})$  and  $P(HMI | \bar{F}, \mathbf{o})$ .

Note that if our bound on the integrity risk is too conservative, the system will not be available. For example, if  $P(\check{\mathbf{n}} = \mathbf{o} | \bar{F})$  is low, the bound on the integrity

risk is likely to exceed the specified integrity risk requirement. In order to produce a tight bound on the true integrity risk, we want to minimize the right-hand-side of equation 2.28 based on the choice of fix  $\mathbf{o}$ . It is desirable to maximize  $P(\check{\mathbf{n}} = \mathbf{o} | \bar{F})$  while simultaneously minimizing  $P(HMI | \bar{F}, \mathbf{o})$ . So, under the fault free scenario,  $\mathbf{o}$  is chosen to be the correct fix because this fix generates the largest  $P(\check{\mathbf{n}} = \mathbf{o} | \bar{F})$ , and produces the lowest  $P(HMI | \bar{F}, \mathbf{o})$ .

### 2.3.2 Computing The Probability of Fix.

First we consider the probability that we will fix to the correct fix candidate  $P(\check{\mathbf{n}} = \mathbf{o} | \bar{F})$ . The formula for the probability of successful fix using bootstrap is given in [Teu01a] and shown in equation 2.29. Here, we introduce the notation  $j|J$  which means the  $j^{th}$  ambiguity given that we have fixed all previous ambiguities.

$$P(\check{\mathbf{n}} = \mathbf{o} | \bar{F}) = \prod_{j=1}^k \left[ 2\Phi \left( \frac{1}{2\sigma_{j|J}} \right) - 1 \right]$$

$$\text{with, } \Phi(x) = \int_{-\infty}^x \frac{1}{\sqrt{2\pi}} e^{-1/2v^2} dv \quad (2.29)$$

where,

$\sigma_{j|J}$  : variance of the  $j^{th}$  ambiguity given that all previous ambiguities  $J := 1, \dots, j$

have been fixed

$\Phi(x)$  : cumulative distribution function

The second term that needs to be computed in equation 2.28 is  $P(HMI | \bar{F}, \mathbf{o})$ . Computing  $P(HMI | \bar{F}, \mathbf{o})$  is not much different for bootstrap than for the float case. Except, this probability is subject to the condition of fixing to the correct fix. Hazardous misleading information for the fault free scenario occurs when the estimate error  $\delta\check{x}$  exceeds the pre-defined alert limit,  $\ell$ . This means that the impact of fixing correctly on the estimate error must be determined. Equation 2.30 shows a more detailed expression for  $P(HMI | \bar{F}, \mathbf{o})$ .

$$P(HMI | \bar{F}, \mathbf{o}) = P(|\delta\check{\mathbf{x}}_x| > \ell | \check{\mathbf{n}} = \mathbf{o}) \quad \text{with, } \delta\check{\mathbf{x}}_x \sim N(0, \sigma_x^2) \quad (2.30)$$

where,

$\delta\check{\mathbf{x}}_x$  : position error corresponding to state of interest  $x$

$\ell$  : alert limit corresponding to position state of interest

$\sigma_x$  : standard deviation of position error for state  $x$

We know that the correct fix does not introduce a bias, so the mean of  $\delta\check{\mathbf{x}}_x$  is not affected. However, the fixing procedure affects the variance. This quantity can be evaluated using equation 2.22. The variance  $\sigma_x^2$  is the element of the diagonal of the updated state covariance matrix  $\mathbf{P}_k$  corresponding to the state for which HMI is evaluated for.

## 2.4 Fault Free Integrity in EPIC-Light Cycle Resolution

The EPIC-light integrity risk bounding method was created as a less-conservative alternative to bootstrap risk bounding. This procedure does not use the conservative assumption that all incorrect fixes cause hazardous information. Instead, a candidate region is defined, in which the integrity risk is evaluated [KP10]. EPIC-light provides a tighter integrity risk bound at the cost of additional computation.

**2.4.1 EPIC-Light Integrity Risk Bound.** We choose to only evaluate the integrity risk for a subset of the complete integer space, which we call the candidate region,  $C \subset \mathbb{Z}^k$ . The complement to the candidate region is defined as  $\bar{C}$ . Together, the candidate region and its complement comprise the entire integer space. The conservative assumption here is that a hazardous situation occurs if we fix outside of the chosen candidate region (rather than just the correct fix, in Section 2.3). Again, as with the bootstrap bound, the integrity risk is developed from equation 2.25. For the fault free case, the probability of HMI is expressed as,

$$P(HMI | \bar{F}) := \sum_{\boldsymbol{\eta} \in C} P(HMI | \bar{F}, \boldsymbol{\eta}) P(\check{\mathbf{n}} = \boldsymbol{\eta} | \bar{F})$$

$$\begin{aligned}
& + \sum_{\boldsymbol{\eta} \in \bar{C}} \overset{1}{P}(HMI | \bar{F}, \boldsymbol{\eta}) P(\check{\mathbf{n}} = \boldsymbol{\eta} | \bar{F}) \\
& \leq \sum_{\boldsymbol{\eta} \in C} P(HMI | \bar{F}, \boldsymbol{\eta}) P(\check{\mathbf{n}} = \boldsymbol{\eta} | \bar{F}) + \sum_{\boldsymbol{\eta} \in \bar{C}} P(\check{\mathbf{n}} = \boldsymbol{\eta} | \bar{F}) \quad (2.31)
\end{aligned}$$

Now, since spaces  $C$  and  $\bar{C}$  are complements, the substitution

$$\sum_{\boldsymbol{\eta} \in \bar{C}} P(\check{\mathbf{n}} = \boldsymbol{\eta} | \bar{F}) = 1 - \sum_{\boldsymbol{\eta} \in C} P(\check{\mathbf{n}} = \boldsymbol{\eta} | \bar{F}) \quad (2.32)$$

is made in equation 2.31 to obtain, the bound on the probability of HMI under fault free conditions.

$$\begin{aligned}
P(HMI | \bar{F}) & \leq \sum_{\boldsymbol{\eta} \in C} P(HMI | \bar{F}, \boldsymbol{\eta}) P(\check{\mathbf{n}} = \boldsymbol{\eta} | \bar{F}) + 1 - \sum_{\boldsymbol{\eta} \in C} P(\check{\mathbf{n}} = \boldsymbol{\eta} | \bar{F}) \\
& \leq 1 - \sum_{\boldsymbol{\eta} \in C} (1 - P(HMI | \bar{F}, \boldsymbol{\eta}) P(\check{\mathbf{n}} = \boldsymbol{\eta} | \bar{F})) \quad (2.33)
\end{aligned}$$

Equation 2.33 provides a bound on the integrity risk, which is ensured to be conservative regardless of our candidate subset choice,  $C$ . However, we must be able to compute the necessary probabilities  $P(HMI | \bar{F}, \boldsymbol{\eta})$  and  $P(\check{\mathbf{n}} = \boldsymbol{\eta} | \bar{F})$  for all candidates within subset  $C$  [KP10].

#### 2.4.2 Integer Candidate Subset.

Since we have the freedom to choose the candidate subset, we want to define it such that we minimize the bound on the integrity risk. We want to find the set of candidates  $C$  that gives the tightest practical bound on  $P(HMI | \bar{F}, \boldsymbol{\eta})$  in equation 2.33. The bound is guaranteed to still be conservative.

In Section 2.3.1 the bootstrap bound was evaluated at the correct fix. In this case, the candidate region for EPIC is chosen such that it is centered about the correct fix. The correct fix has the highest probability of occurrence in the absence of a measurement bias. The size or extent of the subset can be determined experimentally (as explained in [KP10]). It can be increased if a tighter bound is desired [KP10].

#### 2.4.3 Probability Computations.

Since EPIC considers a candidate region, the

probability of fix occurrence must be computed for all possible integer fix candidates  $\boldsymbol{\eta}$  within that region. The probability distribution is developed in [Teu01b] and derived for EPIC in [KP10]. The result is equation 2.34, where  $k$  denotes the number of fixed integers.

$$P(\check{\mathbf{n}} = \boldsymbol{\eta} | \overline{F}) = \prod_{j=1}^k \left[ \Phi \left( \frac{1 - 2\mathbf{l}_j^T \boldsymbol{\zeta}}{2\sigma_{j|J}} \right) + \Phi \left( \frac{1 + 2\mathbf{l}_j^T \boldsymbol{\zeta}}{2\sigma_{j|J}} \right) - 1 \right] \quad (2.34)$$

with,  $\Phi(x) = \int_{-\infty}^x \frac{1}{\sqrt{2\pi}} e^{-1/2v^2} dv$

where,

$\boldsymbol{\eta}$  : candidate fix vector

$\mathbf{o}$  : correct fix vector

$\boldsymbol{\zeta}$  : vector offset or error with respect to the correct fix  $\boldsymbol{\zeta} := \mathbf{o} - \boldsymbol{\eta}$

$\mathbf{l}_j$  :  $j^{\text{th}}$  column of unit lower triangular decomposition matrix from the decomposition of the ambiguity covariance matrix [Teu01a]

The distribution is centered about the correct fix, therefore  $\mathbf{l}_j^T \boldsymbol{\zeta}$  represents the bias induced in the distribution by incorrect fix candidates. And, if  $\boldsymbol{\zeta} = \mathbf{0}$  the distribution collapses down to equation 2.29 for the correct fix in the bootstrap bounding method.

#### 2.4.4 Impact on Position Domain.

In addition to inducing a bias when computing the probability of fix, incorrect integer candidates also bias the mean of the position estimate error. (This was not a problem for bootstrap, since only the correct fix was considered.) The bias  $\mathbf{p}_k$  in the position estimate error due to incorrect fixes is derived in [KP10], and presented below (for  $k$  fixed integers).

$$\mathbf{p}_k = \mathbf{K}_{kk(1:3,:)}(\mathbf{o} - \boldsymbol{\eta}) \in \mathbb{R}^{3 \times 1} \quad (2.35)$$

where,

$\mathbf{p}_k$  : bias on position state estimate due to candidate  $\boldsymbol{\eta}$ , for  $k$  fixed integers

Here,  $\mathbf{K}_{kk(1:3,:)}$  denotes the first three rows of gain matrix  $\mathbf{K}_{kk}$  from the integer fixing procedure, equation 2.23. All the terms in equation 2.33 are now defined.

In this chapter, we have derived bounds on the integrity risk using the bootstrap and EPIC-light fixing processes under fault-free conditions. This derivation will be extended in Chapter 5 to cases where faults are present, so that the entire integrity risk in equation 2.24 can be computed. But, before that, the measurement error correlations for our application are modelled.

## CHAPTER 3

### UPDATED ERROR AND FAULT MODELS

In this chapter, the error models for the ionosphere, troposphere and multipath (MP time-correlation to be specific) are described and updated. For each error model, the correlation with time, with signal frequency and with other measurements is derived. In the following section, existing ionospheric and tropospheric models are discussed for a single SV, then extended to multiple SVs in later sections. The correlation between geometry free and carrier measurements is also established. Finally, the covariance matrix and fault for the example application are discussed.

There will be some foreshadowing in this chapter, because we will compute the covariance matrix not for the benchmark measurement equation 2.17, but for a measurement equation containing GF, carrier, and carrier measurements at some initial reference time. The specific reasons for the addition of initial epoch carrier will be discussed in Chapter 4. This will not distract from the focus of this chapter, which is to discuss correlations between measurements and combination of measurements. However, if it will motivate the reader through this lengthy covariance assembly, he/she is encouraged to skip to Section 3.4 and return to this chapter after reading Chapter 4 (especially Section 4.3 covering the Unified RAIM concept).

#### **3.1 Differential Error Models**

As mentioned earlier, double differenced carrier phase measurements are used for our benchmark application because they provide higher accuracy (relative to code phase measurements), and eliminate satellite and receiver clock errors. In addition, most of the ionospheric and tropospheric errors are eliminated in differential GPS. However, because the atmosphere is not uniform, separation between the user and

reference receivers causes residual errors to remain. These residual errors are often referred to as decorrelation errors. Ionospheric and tropospheric measurement errors are first described using single difference (user-reference) measurements, and considering a single SV. Figure 3.1 below depicts the ionospheric and tropospheric layers along with their nominal height from the earth's surface.

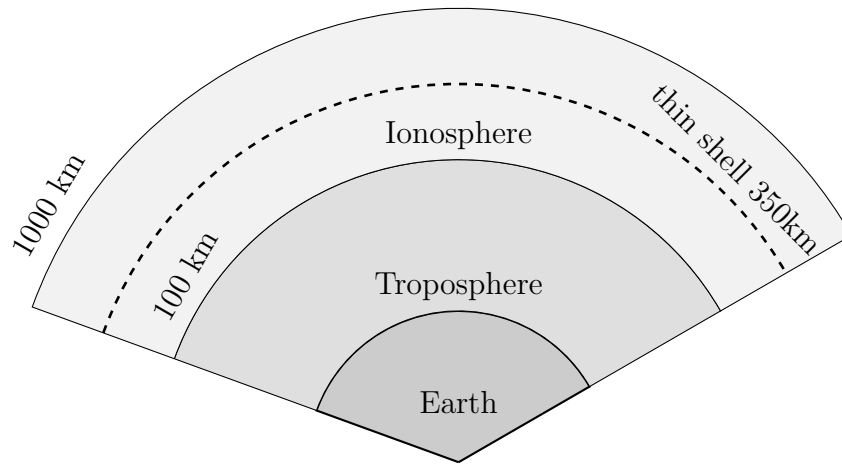


Figure 3.1. Ionospheric and tropospheric layers

**3.1.1 Ionospheric Error Model.** The model used to describe the ionospheric error in this work is developed in [MMB<sup>+</sup>00] and will be referred to as the LAAS iono model. But, before the model is introduced, we first discuss the use of an obliquity factor. The obliquity factor is used to relate the slant iono error to the vertical iono error, as shown in equation 3.1 below.

$${}^i I_{SD} = c_I({}^i \theta) I_{v,SD} \quad (3.1)$$

where,

${}^i I_{SD}$  : differential slant iono error for SV  $i$  and SD measurements at L1 frequency

$I_{v,SD}$  : differential vertical iono error for SD measurements at L1 frequency

$c_I({}^i \theta)$  : iono obliquity factor (which is a function of satellite elevation,  ${}^i \theta$ )

The obliquity factor  $c_I(i\theta)$  essentially scales the vertical iono error  $I_{v,SD}$ , taking into account that for satellite elevation angles other than 90 degrees, the signal passes through a larger layer of the ionosphere. Equation 3.2 gives the obliquity factor expression for the ionosphere [ME06].

$$c_I(i\theta) = \left[ 1 - \left( \frac{R_e}{R_e + h_I} \right)^2 \cos^2(i\theta) \right]^{-1/2} \quad (3.2)$$

where,

$R_e$  : radius of earth

$h_I$  : nominal altitude of ionosphere (thin shell model) from earth's surface

$i\theta$  : satellite elevation angle in radians

LAAS models the vertical ionospheric error as a linear gradient. The differential iono error gradient  $g_{Iv}$  is multiplied by the distance  $d$  between receivers to describe the vertical iono error ( $I_{v,SD} = dg_{Iv}$ ) [MMB<sup>+</sup>00]. Making this substitution for  $I_{v,SD}$  in equation 3.1, we write the differential iono error (for measurements at L1 frequency) as,

$${}^i I_{SD} = c_I(i\theta) dg_{Iv} \quad (3.3)$$

where,

$g_{Iv}$  : vertical iono gradient

$d$  : horizontal baseline between reference and user

Equation 3.3 is the final expression for the ionospheric error model. Under nominal ionospheric conditions, the gradient  $g_{Iv}$  is assumed to be normally distributed with zero mean and standard deviation  $\sigma_{Ivg}$ . The variance of the iono error on L1 frequency  ${}^i \sigma_I^2$  is therefore written as,

$${}^i \sigma_I^2 = c_I(i\theta)^2 d^2 \sigma_{Ivg}^2 \quad (3.4)$$

Assuming a constant gradient  $g_{Iv}$  over time, the time-correlation between successive measurements (from the same SV) is determined using the expected value operator  $E\{\}$ . Subscript 0 is used to identify term corresponding to the initial measurement.

$$\begin{aligned} E\{^i I_{SD} {}^i I_{0,SD}\} &= \{c_I({}^i\theta)d\sigma_{Ivg}\}\{c_I({}^i\theta_0)d_0\sigma_{Ivg}\} \\ &= c_I({}^i\theta)c_I({}^i\theta_0)dd_0\sigma_{vIg}^2 \end{aligned} \quad (3.5)$$

In addition, ionospheric errors are also correlated between L1 and L2 frequencies. The iono error at the L2 frequency may be written as a function of the error at L1 frequency,

$${}^i I_{L2,SD} = \frac{\lambda_{L2}^2}{\lambda_{L1}^2} {}^i I_{SD} \quad (3.6)$$

The correlation between L1 and L2 frequencies becomes,

$$E\{^i I_{SD} {}^i I_{L2,SD}\} = \frac{\lambda_{L2}^2}{\lambda_{L1}^2} \sigma_I^2 \quad (3.7)$$

**3.1.2 Tropospheric Error Model.** In this work, the model used to describe the tropospheric error is taken from [MMB<sup>+</sup>00] and will be referred to as the LAAS tropo model. Again, an obliquity factor is used to relate the zenith tropo error to the actual error.

$${}^i T_{SD} = c_T({}^i\theta)T_{v,SD} \quad (3.8)$$

where,

${}^i T_{SD}$  : differential tropo error for SV  $i$

$T_{v,SD}$  : differential vertical tropo error

$c_T({}^i\theta)$  : tropo obliquity factor (which is a function of satellite elevation,  ${}^i\theta$ )

Equation 3.9 gives the obliquity factor expression for the troposphere [ME06].

$$c_T({}^i\theta) = \frac{1.001}{[0.002001 + \sin^2({}^i\theta)]^{1/2}} \quad (3.9)$$

where,

${}^i\theta$  : satellite elevation angle in radians

The LAAS model for the differential vertical tropospheric error is shown below.

$$T_{v,SD} = h_T(1 - e^{-h/h_T})N$$

where,

$N$  : refractivity at earth's surface

$h_T$  : nominal tropo height

$h$  : height of user receiver with respect to reference receiver

Finally, the tropo error model becomes,

$${}^iT_{SD} = c_T({}^i\theta)h_T(1 - e^{-h/h_T})N \quad (3.10)$$

The variance of the tropo error  ${}^i\sigma_T^2$  is therefore written as,

$$E\{{}^iT_{SD}{}^iT_{SD}\} := {}^i\sigma_T^2 = [c_T({}^i\theta)h_T(1 - e^{-h/h_T})]^2\sigma_N^2 \quad (3.11)$$

The time correlation is computed in a similar manner to the iono time correlation. Again, subscript 0 is used to denote the initial measurement.

$$\begin{aligned} E\{{}^iT_{SD}{}^iT_{0,SD}\} &= \{c_T({}^i\theta)h_T(1 - e^{-h/h_T})\sigma_N\}\{c_T({}^i\theta_0)h_T(1 - e^{-h_0/h_T})\sigma_N\} \\ &= c_T({}^i\theta)c_T({}^i\theta_0)(1 - e^{-h/h_T})(1 - e^{-h_0/h_T})h_T^2\sigma_N^2 \end{aligned} \quad (3.12)$$

Also, since the troposphere affects all frequencies identically, tropo error is fully correlated over L1 and L2 frequencies (i.e.  ${}^iT_{SD} = {}^iT_{L2,SD}$ ).

### 3.2 Receiver Noise and Multipath Error Models

In this section, the carrier measurement error time-correlation, the GF measurement variance, and the correlation between GF and carrier measurements is derived using raw measurements. Previous work assumed GF measurements to be

uncorrelated with carrier phase [Kha08]. To ensure integrity it is important that the system model be as accurate as possible.

**3.2.1 Carrier Time-Correlation.** Multipath time-correlation is modeled as a first order Gauss-Markov process with zero mean. In other words, a measurement sample  $m$  is related to the previous sample  $(m - 1)$  via an exponential function. The multipath error model is expressed as,

$${}^i\varepsilon_{\phi,m} = (e^{-\beta t_s})^i\varepsilon_{\phi,(m-1)} + \omega_{(m-1)}$$

where,

${}^i\varepsilon_{\phi}$  : multipath error for SV  $i$

$\beta$  : inverse of multipath time constant

$t_s$  : sampling interval

$\omega$  : GMP driving noise, assume  $\sim N(0, \sigma_{\omega}^2)$

We also introduce the autocovariance function, which is needed in Section 3.2.3. From [BP00] we know that the autocorrelation and autocovariance function are equivalent for a distribution with zero mean. Then, the autocovariance function  $C_{xx}(\tau)$  of a random variable  $x$  for a Gauss-Markov process can be written as a function of the time shift  $\tau$  between measurements.

$$\begin{aligned} C_{xx}(\tau) &= E\{x(t)x(t + \tau)\} \\ &= \sigma_x^2 e^{-\beta|\tau|} \end{aligned} \tag{3.13}$$

Here,  $t$  is an arbitrary time, and  $\tau$  is the time shift between sample measurements. Equation 3.13 is used to write the correlation between current and initial epoch carrier measurements as,

$$\begin{aligned} {}^iC_{\varepsilon_{\phi}\varepsilon_{\phi_0}}(\tau) &= E\{{}^i\varepsilon_{\phi}(t){}^i\varepsilon_{\phi_0}(t + \tau)\} \\ &= \sigma_{\phi}^2 \exp(-\beta|\tau|) \end{aligned} \tag{3.14}$$

### 3.2.2 Geometry Free Noise Variance.

From equation 2.13 we have an expression for the GF noise as a function of the noise of the raw measurements that it is derived from. It is a linear combination of independent random variables. So, we can write the variance as,

$${}^i\sigma_{GF}^2 = \left( \frac{{}^i\sigma_{\phi,L1}^2}{\lambda_{L1}^2} + \frac{{}^i\sigma_{\phi,L2}^2}{\lambda_{L2}^2} \right) + \left( \frac{\lambda_{L2} - \lambda_{L1}}{\lambda_{L1} + \lambda_{L2}} \right)^2 \left( \frac{{}^i\sigma_{\rho,L1}^2}{\lambda_{L1}^2} + \frac{{}^i\sigma_{\rho,L2}^2}{\lambda_{L2}^2} \right) \quad (3.15)$$

This is the variance of the raw GF measurement before any differencing between receiver or SV. Geometry free measurements are filtered using a running average. Time averaged GF noise is shown below, where  $m$  denotes the number of samples.

$${}^i\bar{\varepsilon}_{GF} = \frac{1}{{}^im} \sum_{q=1}^{im} {}^i\varepsilon_{GF,q} \quad (3.16)$$

Note that  $m$  is SV dependent. This is because SVs are filtered over different time periods depending on when they rise into view. In addition, the  $m^{\text{th}}$  sample is defined to be the current sample. Here, an overbar notation is used on the measurement error to denote averaging. By assuming a continuous sampling interval ( $t_s \rightarrow 0$ ) the variance of the filtered GF measurements may be written as a function of the filtering period (denoted  ${}^i\Upsilon$ ), rather than number of samples  $m$  and sampling interval  $t_s$ . The expression for the variance of a random variable using ‘continuous sampling’ is given in [BP00]. The derivation for filtered GF measurements is presented in [Heo04]. Using the expression for  ${}^i\sigma_{GF}^2$  given in equation 3.15, we may write,

$${}^i\sigma_{GF}^2 = {}^i\sigma_{GF}^2 \left\{ \frac{2}{{}^i\Upsilon\beta} - \frac{2}{{}^i\Upsilon^2\beta^2}(1 - e^{-{}^i\Upsilon\beta}) \right\} \quad (3.17)$$

Alternatively, the ‘discrete sampling’ derivation is shown in appendix B. It serves a dual purpose. It is used to verify the methodology used in the following section to derive the correlation between filtered GF and carrier measurements, which is carried out in a discrete fashion. It also results in a discrete expression for filtered

GF variance, which may prove useful in future work.

### 3.2.3 Correlation of GF Measurements with Carrier Measurements.

This section analyzes how the receiver noise and multipath (RNM) error of filtered GF measurements is correlated with that of carrier measurements. We see from equation 2.13 that the GF noise is a linear combination of raw carrier and code error. However, ionospheric and tropospheric errors are not present in GF measurements [Kha08]. So, only the RNM induces correlation between GF and carrier measurements. In the following derivation, WL measurements are considered.

The covariance of filtered GF and carrier measurements is derived assuming a discrete sampling rate. Using the definition of  ${}^i v_{\phi_w}$  from equation 2.10 we can write the GF measurement noise given in equation 2.13 as follows.

$${}^i \varepsilon_{GF} = \frac{{}^i \varepsilon_{\phi_w}}{\lambda_w} - \frac{\lambda_n}{\lambda_w} \left( \frac{{}^i \varepsilon_{\rho_{L1}}}{\lambda_{L1}} + \frac{{}^i \varepsilon_{\rho_{L2}}}{\lambda_{L2}} \right) \quad (3.18)$$

Since we are only considering RNM, we use  ${}^i \varepsilon_{\phi}$  instead of  ${}^i v_{\phi}$ . Note that  ${}^i \varepsilon_{\phi_w}$ ,  ${}^i \varepsilon_{\rho_{L1}}$ , and  ${}^i \varepsilon_{\rho_{L2}}$  are all in units of length, whereas  ${}^i \varepsilon_{GF}$  is in units of cycles.

Using the definition in 3.18, equation 3.16 may be expanded as,

$${}^i \bar{\varepsilon}_{GF} = \frac{1}{\lambda_w} {}^i \bar{\varepsilon}_{\phi_w} - \frac{\lambda_n}{\lambda_w \lambda_{L1}} {}^i \bar{\varepsilon}_{\rho_{L1}} - \frac{\lambda_n}{\lambda_w \lambda_{L2}} {}^i \bar{\varepsilon}_{\rho_{L2}}$$

Since carrier and code measurements are uncorrelated, the expected value of code with carrier would be zero. The GF and carrier correlation can be computed using the expected value operator, which yields,

$$\begin{aligned} E\{{}^i \bar{\varepsilon}_{GF} {}^i \varepsilon_{\phi_w}\} &= \frac{1}{\lambda_w} E\{{}^i \bar{\varepsilon}_{\phi_w} {}^i \varepsilon_{\phi_w}\} \\ &= \frac{1}{i m} \frac{1}{\lambda_w} \sum_{q=1}^{i m} E\{{}^i \varepsilon_{\phi_w, q} {}^i \varepsilon_{\phi_w, m}\} \\ &= \frac{1}{i m} \frac{1}{\lambda_w} \left( {}^i \sigma_{\phi_w}^2 + \sum_{q=1}^{i m-1} E\{{}^i \varepsilon_{\phi_w, q} {}^i \varepsilon_{\phi_w, m}\} \right) \end{aligned} \quad (3.19)$$

The summation (second term on the right-hand-side) represents the correlation between the current measurement sample  $m$ , and all previous samples. Assuming a Gauss-Markov process with zero mean, this summation may be represented using the autocovariance function, equation 3.13. Note that assuming a constant sampling interval  $t_s$  allows the series to be written as a finite geometric series (using properties of the exponential function), which has a closed-form solution derived in appendix A.

$$\begin{aligned}
\sum_{q=1}^{m-1} E\{x_q x_m\} &= C_{xx}(t_s) + C_{xx}(2t_s) + \cdots + C_{xx}((m-1)t_s) \\
&= \sigma_x^2 \sum_{p=1}^{m-1} (e^{-t_s \beta})^p \\
&= \sigma_x^2 (e^{-t_s \beta}) \frac{1 - (e^{-t_s \beta})^{m-1}}{1 - (e^{-t_s \beta})}
\end{aligned} \tag{3.20}$$

Finally, substituting equation 3.20 into 3.19 and simplifying, we obtain the following expression for the correlation between filtered GF and WL carrier measurements.

$$E\{{}^i\bar{\varepsilon}_{GF}{}^i\varepsilon_{\phi_w}\} = \frac{{}^i\sigma_{\phi_w}^2}{\lambda_w} \frac{1}{{}^im} \left( \frac{1 - e^{-{}^im t_s \beta}}{1 - e^{-t_s \beta}} \right) \tag{3.21}$$

If we want to write equation 3.21 in terms of filtering interval  $\Upsilon$  ( $\Upsilon = t_s(m-1)$ ), we have,

$$E\{{}^i\bar{\varepsilon}_{GF}{}^i\varepsilon_{\phi_w}\} = \frac{{}^i\sigma_{\phi_w}^2}{\lambda_w} \frac{1}{({}^i\Upsilon/t_s + 1)} \left( \frac{1 - e^{-({}^i\Upsilon/t_s + 1)t_s \beta}}{1 - e^{-t_s \beta}} \right) \tag{3.22}$$

Taking the limit of equation 3.22 as the filtering time  $\Upsilon$  tends to zero results in,

$$\lim_{\Upsilon \rightarrow 0} E\{{}^i\bar{\varepsilon}_{GF}{}^i\varepsilon_{\phi_w}\} = \frac{{}^i\sigma_{\phi_w}^2}{\lambda_w}$$

This corresponds to the case where GF measurements are not filtered.

To be consistent with the GF variance expression, we will now obtain a formula under the assumption of continuous sampling. Taking the limit as  $t_s \rightarrow 0$  of

equation 3.22,

$${}^i\sigma_{GF\phi_w}^2 := \lim_{t_s \rightarrow 0} E\{{}^i\bar{\varepsilon}_{GF} {}^i\varepsilon_{\phi_w}\} = \frac{{}^i\sigma_{\phi_w}^2}{\lambda_w} \frac{1}{{}^i\Upsilon\beta} \left(1 - e^{-{}^i\Upsilon\beta}\right) \quad (3.23)$$

This yields a formula for the correlation between filtered GF and carrier measurements, assuming continuous sampling, and concludes the derivation. The result for L1 and L2 frequencies instead of WL is very similar to equation 3.23, except for coefficients based on SV signal wavelength. The expressions will not be derived, but they are presented below for completeness as equations 3.24 and 3.25.

$$\lim_{t_s \rightarrow 0} E\{{}^i\bar{\varepsilon}_{GF} {}^i\varepsilon_{\phi_{L1}}\} = \frac{{}^i\sigma_{\phi_{L1}}^2}{\lambda_{L1}} \frac{1}{{}^i\Upsilon\beta} \left(1 - e^{-{}^i\Upsilon\beta}\right) \quad (3.24)$$

$$\lim_{t_s \rightarrow 0} E\{{}^i\bar{\varepsilon}_{GF} {}^i\varepsilon_{\phi_{L2}}\} = -\frac{{}^i\sigma_{\phi_{L2}}^2}{\lambda_{L2}} \frac{1}{{}^i\Upsilon\beta} \left(1 - e^{-{}^i\Upsilon\beta}\right) \quad (3.25)$$

Correlation between geometry free and initial epoch carrier measurements is more involved. The result is presented below, with details outlined in appendix C. Here,  $\Upsilon$  is the complete filtering period, and  $\Upsilon_a$  corresponds to the filtering period beginning at the initial epoch.

$$\lim_{t_s \rightarrow 0} E\{{}^i\bar{\varepsilon}_{GF} {}^i\varepsilon_{\phi_{w,0}}\} = \frac{\sigma_{\phi_w}^2}{\lambda_w} \frac{1}{{}^i\Upsilon\beta} \left(2 - e^{-{}^i\Upsilon_a\beta} - e^{({}^i\Upsilon_a - {}^i\Upsilon)\beta}\right) \quad (3.26)$$

Notice, when  $\Upsilon \rightarrow \Upsilon_a$ , equation 3.23 is recovered. This is because the carrier measurement at the initial epoch falls at one end of the filtering window.

One issue with these calculations that is specific to our example application, is that the user may not know how long the reference prefilters GF measurements. This may prove to be problematic when attempting to double difference these measurements. One reasonable assumption is that the reference begins filtering as soon as a SV becomes visible. The next section addresses the issues involved in double differencing and assembling the covariance matrix for all SVs.

### 3.3 Complete Error Covariance Matrix Derivation

Until this point, correlations between raw measurements have been modelled on a per-satellite basis. Measurements from all SVs are double differenced and stacked to form the inputs to the WLS positioning process. The measurement error correlations derived in the previous section must also be double differenced and stacked for all SVs. To simplify the full covariance matrix derivation, we assume our benchmark application uses GF and WL carrier measurements. In addition, dual reference antennas are considered to illustrate correlation over reference antennas. Furthermore, measurements may also be correlated across SVs because of the common impact of the troposphere. The procedure for establishing covariance matrices is outlined below.

1. Consider a single ship antenna and form the single difference RNM, iono, and tropo error covariance matrices, for double differenced WL and GF measurements
2. Derive correlation matrices of GF measurements with carrier measurements, as well as carrier time correlation matrices
3. Expand results to dual ship antennas
4. Combine all results in the final measurement noise covariance matrix

To visualize the multiple components of the derivation (addressed in Sections 3.3.1 to 3.3.5), we present the final covariance matrix as,

$$\mathbf{V} = \begin{bmatrix} \mathbf{V}_G & \mathbf{V}_{G\phi} & \mathbf{V}_{G\phi_0} \\ \mathbf{V}_{G\phi}^T & \mathbf{V}_\phi & \mathbf{V}_{\phi\phi_0} \\ \mathbf{V}_{G\phi_0}^T & \mathbf{V}_{\phi\phi_0}^T & \mathbf{V}_{\phi_0} \end{bmatrix} \quad (3.27)$$

where,

$$\begin{aligned} \mathbf{V}_\phi &= \mathbf{T}_{DD}(\mathbf{V}_R + \mathbf{V}_I + \mathbf{V}_T)\mathbf{T}_{DD}^T \\ \mathbf{V}_{\phi_0} &= \mathbf{T}_{DD}(\mathbf{V}_{R_0} + \mathbf{V}_{I_0} + \mathbf{V}_{T_0})\mathbf{T}_{DD}^T \end{aligned}$$

$$\begin{aligned}
\mathbf{V}_{\phi\phi_0} &= \mathbf{T}_{DD}(\mathbf{V}_{R,R_0} + \mathbf{V}_{I,I_0} + \mathbf{V}_{T,T_0})\mathbf{T}_{DD}^T \\
\mathbf{V}_G &= \mathbf{T}_{DD}(\mathbf{V}_{G_{SD}})\mathbf{T}_{DD}^T \\
\mathbf{V}_{G\phi} &= \mathbf{T}_{DD}(\mathbf{V}_{G\phi_{SD}})\mathbf{T}_{DD}^T \\
\mathbf{V}_{G\phi_0} &= \mathbf{T}_{DD}(\mathbf{V}_{G\phi_0_{SD}})\mathbf{T}_{DD}^T
\end{aligned}$$

This covariance matrix results from the addition of initial epoch DD carrier measurements to the measurement equation 2.15 used in the example application. The reason for this will become clear in Chapter 4. In equation 3.27, each matrix in parenthesis (e.g.  $\mathbf{V}_R$ ,  $\mathbf{V}_I$ ,  $\mathbf{V}_T$ ,  $\mathbf{V}_{G_{SD}}$ ,  $\mathbf{V}_{G\phi_{SD}}$ ) is expressed for single difference (between user and reference) measurements. The  $(n-1) \times n$  double difference transformation matrix  $\mathbf{T}_{DD}$  is applied to create the double difference measurement error covariance. Equation 3.28 shows the transformation matrix.

$$\mathbf{T}_{DD} = \begin{bmatrix} -1 & & \\ & \mathbf{I} & \\ -1 & & \end{bmatrix} \in \mathbb{R}^{(n-1) \times n} \quad (3.28)$$

Note that each block matrix corresponding to carrier measurements (i.e.  $\mathbf{V}_\phi$  and  $\mathbf{V}_{\phi_0}$ ) includes iono  $\mathbf{V}_I$  and tropo  $\mathbf{V}_T$  components. In the following subsections, these individual components are defined. Ionospheric and tropospheric models are also present in the time-correlated carrier phase measurement error covariance matrix  $\mathbf{V}_{\phi\phi_0}$ . Since these errors are eliminated when GF measurements are formed, only RNM correlation is considered for  $\mathbf{V}_{G\phi}$ .

**3.3.1 Receiver Noise and Multipath.** We begin by constructing the single difference RNM matrices for carrier phase and GF measurements. The variance of WL carrier RNM,  ${}^i\sigma_{WL}^2$ , is assumed to be the same for both user and reference receivers. So, the single difference variance  ${}^i\sigma_{WL_{SD}}^2$  is simply twice the raw variance ( ${}^i\sigma_{WL_{SD}}^2 = 2{}^i\sigma_{WL}^2$ ). In addition it is uncorrelated between SVs. Therefore, the single

difference covariance matrix is diagonal, and can be expressed as,

$$\mathbf{V}_R = \begin{bmatrix} {}^1\sigma_{WLSD}^2 & & \mathbf{0} \\ & \ddots & \\ \mathbf{0} & & {}^n\sigma_{WLSD}^2 \end{bmatrix} \quad (3.29)$$

It is further assumed that each RNM process is stationary. Therefore  $\mathbf{V}_R = \mathbf{V}_{R_0}$ .

The variance of GF measurements is not assumed to be the same for user and reference receivers, because they may have different filtering periods. Therefore, the single difference GF variance  ${}^i\sigma_{GFSD}^2$  is computed as the sum of user ( $u$ ) and reference ( $r$ ) GF measurement variances ( ${}^i\sigma_{GFSD}^2 = {}^i\sigma_{GF,u}^2 + {}^i\sigma_{GF,r}^2$ ). The filtered GF variance  ${}^i\sigma_{GF}^2$  is given by equation 3.17, and the single difference covariance matrix is given by,

$$\mathbf{V}_{GSD} = \begin{bmatrix} {}^1\sigma_{GFSD}^2 & & \mathbf{0} \\ & \ddots & \\ \mathbf{0} & & {}^n\sigma_{GFSD}^2 \end{bmatrix} \quad (3.30)$$

Again,  $\mathbf{V}_{GSD}$  is a diagonal matrix, because there is no RNM correlation between SVs.

**3.3.2 Ionosphere and Troposphere.** The ionospheric and tropospheric error models in Section 3.1 describe the residual error between receivers after performing a single difference of measurements. So we look at correlation over SVs.

The iono error for WL measurements is determined by substituting iono error  ${}^iI_{SD}$  into the WL error  ${}^iv_{\phi_w}$  in equation 2.10. Note that equation 3.6 is used to relate iono error at L2 to that at L1. After simplification, the single difference WL iono error  ${}^iI_{WL,SD}$  reduces to  ${}^iI_{WL,SD} = \left(\frac{-\lambda_{L2}}{\lambda_{L1}}\right){}^iI_{SD}$  (where  ${}^iI_{SD}$  is the single difference iono error at L1 frequency). The expected value operator, is used to compute the variance of WL iono error,  ${}^i\sigma_{IWL} = {}^i\sigma_I \left(\frac{\lambda_{L2}}{\lambda_{L1}}\right)^2$ . Equation 3.4 gives the iono error variance  ${}^i\sigma_I$  for each SV at the L1 frequency. Assuming no correlation between SVs, the single

difference covariance matrix is diagonal and can be written as,

$$\mathbf{V}_I = \begin{bmatrix} {}^1\sigma_I^2 \left(\frac{\lambda_{L2}}{\lambda_{L1}}\right)^2 & & \mathbf{0} \\ & \ddots & \\ \mathbf{0} & & {}^n\sigma_I^2 \left(\frac{\lambda_{L2}}{\lambda_{L1}}\right)^2 \end{bmatrix} \quad (3.31)$$

The WL tropo error must also be computed using equation 2.10. Unlike the iono, the tropo error has the same effect on both GPS frequencies. After simplification, the WL tropo error  ${}^i T_{WL,SD}$  reduces to the tropo error at L1 frequency,  ${}^i T_{WL,SD} = {}^i T_{SD}$ . Therefore, the variance is the same as that on the L1 frequency, equation 3.11. In addition, the tropo error is correlated over all SVs. To simplify the formulation of the single difference covariance matrix, we define vector  $\mathbf{a}$  using the tropo error coefficients for all visible SVs as,

$$\mathbf{a} = \left[ c_T({}^1\theta)h_T(1 - e^{-h/h_T}) \quad \dots \quad c_T({}^n\theta)h_T(1 - e^{-h/h_T}) \right]^T \quad (3.32)$$

The single difference covariance matrix is then formed using the outer product of vector  $\mathbf{a}$ . This matrix is fully populated because tropospheric error is correlated across all SVs.

$$\mathbf{V}_T = \left[ \mathbf{a}\mathbf{a}^T \right] \sigma_N^2 \quad (3.33)$$

A similar procedure is used to compute iono and tropo error covariance matrices at the initial epoch ( $\mathbf{V}_{I_0}$  and  $\mathbf{V}_{T_0}$  in equation 3.27).

### 3.3.3 Correlation Matrix Between Geometry-Free and Carrier Measurements.

The derivation of the correlation between GF and WL carrier measurements is complicated by the difference in filtering intervals at user and reference receivers. For our benchmark application, user and reference may have different filtering periods  $\Upsilon_a$  and  $\Upsilon$  respectively. To deal with this, we compute correlations individually for user and reference raw WL measurements. Single difference is com-

puted as shown below, where  ${}^i\sigma_{GF\phi_w}^2$  is expressed in equation 3.23.

$$\{{}^i\sigma_{GF\phi_w}^2\}_{SD} = \{{}^i\sigma_{GF\phi_w}^2\}_{user} + \{{}^i\sigma_{GF\phi_w}^2\}_{reference}$$

As mentioned earlier, RNM is not correlated between SVs. The single difference GF and carrier covariance matrix is diagonal, and is defined as,

$$\mathbf{V}_{G\phi_{SD}} = \begin{bmatrix} \{{}^1\sigma_{GF\phi_w}^2\}_{SD} & & \mathbf{0} \\ & \ddots & \\ \mathbf{0} & & \{{}^n\sigma_{GF\phi_w}^2\}_{SD} \end{bmatrix}$$

The same procedure is used to compute  $\mathbf{V}_{G\phi_{0SD}}$ , but the filtering time is different. It can be assumed that the user begins filtering once it enters the broadcast radius of the reference receiver (which would be epoch 0), so the user does not have time to filter GF measurements prior to the initial epoch (epoch 0).

**3.3.4 Carrier Phase Measurement Time-Correlation.** The carrier time-correlation includes RNM, but also ionospheric and tropospheric errors. RNM is modelled using a Gauss-Markov random process (see Section 3.2.1). Because RNM is not correlated between SVs, the time-correlation matrix is defined using equation 3.14 as,

$$\mathbf{V}_{R,R_0} = \begin{bmatrix} {}^1C_{\varepsilon_\phi\varepsilon_{\phi_0}}(\tau) & & \mathbf{0} \\ & \ddots & \\ \mathbf{0} & & {}^nC_{\varepsilon_\phi\varepsilon_{\phi_0}}(\tau) \end{bmatrix} \quad (3.34)$$

where  $n$  is the number of visible SVs. Recall, that  $\tau$  denotes the time difference between measurements.

Then, to simplify the notation for the ionospheric time-correlation covariance matrix, we define a diagonal matrix  $\mathbf{A}$  (which contains the iono error coefficients expressed in equation 3.3 on its diagonal) as,

$$\mathbf{A} = \begin{bmatrix} c_I({}^1\theta)d & & \mathbf{0} \\ & \ddots & \\ \mathbf{0} & & c_I({}^n\theta)d \end{bmatrix} \quad (3.35)$$

Assuming the iono gradient is constant over the duration of interest, the iono time correlation can be written as the product of current and initial time coefficients ( $\mathbf{A}$  and  $\mathbf{A}_0$  respectively), scaled by the variance of the vertical iono gradient  $\sigma_{Ivg}^2$ .

$$\mathbf{V}_{I,I_0} = \mathbf{A}_0 \mathbf{A} \sigma_{Ivg}^2 \quad (3.36)$$

Finally, for tropospheric time-correlation, the initial and current time tropo coefficient vectors  $\mathbf{a}_0$  and  $\mathbf{a}$  respectively (defined in equation 3.32) are used to compute the single difference covariance matrix. Again, the matrix is fully populated. Assuming constant nominal tropo refractivity over the duration of interest, the single difference covariance matrix is written as the outer product,

$$\mathbf{V}_{T,T_0} = [\mathbf{a}_0 \mathbf{a}^T] \sigma_N^2 \quad (3.37)$$

**3.3.5 Case of Multiple Reference Receivers.** For the case of a single reference antenna, the final covariance matrix can be derived using equation 3.27. However, when considering multiple reference antennas (e.g. two antennas), the correlation between their measurements must be addressed. This correlation arises from the fact that both reference antennas are single differenced with the same user measurements.

The matrices computed thus far only correspond to a single antenna. Therefore, all single difference covariance matrices must be stacked twice to account for dual antennas. The following equation is used to modify the single difference matrices to account for two ship antennas.

$$\mathbf{V}_\gamma = \begin{bmatrix} \mathbf{V}_\gamma & C\mathbf{V}_\gamma \\ C\mathbf{V}_\gamma & \mathbf{V}_\gamma \end{bmatrix} \quad (3.38)$$

where,

$C$  : correlation coefficient

$\mathbf{V}_\gamma$  : used to denote any of the single difference matrices constructed in Sections 3.3.1 through 3.3.4

It is assumed that RNM is independent across reference receivers. In this case, for RNM matrices  $\mathbf{V}_R$ ,  $\mathbf{V}_{R_0}$ ,  $\mathbf{V}_{R,R_0}$ ,  $\mathbf{V}_{G_{SD}}$ ,  $\mathbf{V}_{G\phi_{SD}}$ , and  $\mathbf{V}_{G\phi_{0SD}}$ , equation 3.38 is used with correlation coefficient  $C = 0.5$ . Matrices corresponding to iono and tropo errors ( $\mathbf{V}_I$ ,  $\mathbf{V}_{I_0}$ ,  $\mathbf{V}_{I,I_0}$ ,  $\mathbf{V}_T$ ,  $\mathbf{V}_{T_0}$ , and  $\mathbf{V}_{T,T_0}$ ) are treated differently because they are fully correlated over the two reference antennas. So, equation 3.38 is used with  $C = 1$ . Since all of the aforementioned matrices have doubled in size, the double difference transformation matrix  $\mathbf{T}_{DD}$  needs to be adjusted accordingly. Equation 3.38 can be used with  $C = 0$  to create the new block diagonal transformation matrix. The final covariance matrix is then obtained using equation 3.27.

### 3.4 Orbit Ephemeris Fault (OEF)

An Orbit Ephemeris Fault (OEF) is an unusually large error in the computed position of the space vehicles. As mentioned in the introduction, users must compute the SV locations in order to determine their own position. Therefore, an OEF can cause a bias in the user position estimate. This is unacceptable for many applications requiring high accuracy and integrity because it may cause integrity risk requirements to be exceeded. In this section we describe OEF classification and describe the OEF model used in the rendezvous application.

**3.4.1 Types of Orbit Ephemeris Faults.** Ephemeris faults are categorized into two main groups, type A and type B. Type A faults involve a SV maneuver (such as in-track station-keeping burns). Type A1 faults are caused by a blundered ephemeris during an orbit tangential maneuver. Type A2 faults are caused from broadcasting the pre-maneuver ephemeris (i.e. never updating the ephemeris). Type A2' faults are maneuvers in any direction (e.g. in the event of outgassing) occurring when the pre-maneuver ephemeris remains broadcast. All other faults in absence of SV maneuvers are type B faults. Type B faults are caused by a blundered ephemeris.

Although OEFs are rare, a type A2 fault occurred in 2007 [Tea07]. A SV maneuver was performed, and the SV was not marked ‘unhealthy’ (which should be done to inform users of the maneuver). During this time, it was possible to use this SV with the pre-maneuver ephemeris, which may have led to a hazardous situation for the user. To date, this is the only recorded OEF. However, it aided in validating the need for, and further development of OEF monitors.

**3.4.2 Effect on Differential Measurements.** For standalone GPS measurements, the fault component along the LOS vector impacts ranging error [ME06]. For differential GPS users, the fault impact on differential ranging error becomes more complex. In [Cha01] it is shown that only the tangential component (perpendicular to LOS) of an OEF impacts differential GPS measurements. In the following section, we show that the fault impact on estimate error is proportional to user-to-reference separation distance. Note that this was also shown in [Cha01].

**3.4.3 Ephemeris Fault Vector For Straight in Approach.** In applications where the user approaches the reference along a straight line, an ephemeris fault can be modeled as a spatial ramp over user-reference separation distance. Consider a blundered orbit ephemeris that causes an error in the observation matrix  $\delta\mathbf{H}$ . This fault only affects the LOS components of the observation matrix (noted  $\mathbf{G}$  in equation 2.17), so the cycle ambiguity component of  $\mathbf{H}$  is unaffected by ephemeris faults. The general measurement equation may be re-written as,

$$\begin{aligned}\mathbf{z} &= (\mathbf{H} - \delta\mathbf{H})\mathbf{u} + \mathbf{v} \\ &= \mathbf{H}\mathbf{u} + \mathbf{v} - \delta\mathbf{H}\mathbf{u}\end{aligned}\tag{3.39}$$

We also know that  $\delta\mathbf{H}$  does not impact cycle ambiguity states, so we can write the last term as follows,

$$\mathbf{z} = \mathbf{H}\mathbf{u} + \mathbf{v} - \delta\mathbf{H} \begin{bmatrix} \mathbf{x} \\ \mathbf{0} \end{bmatrix}$$

(3.40)

Assuming that the user approaches the reference along a straight line, the relative position states vary linearly with distance to reference. Using this information, we write the position states as a vector  $\mathbf{s}$ , which is scaled by distance to ship,  $d$ , such that  $\begin{bmatrix} \mathbf{x} \\ \mathbf{0} \end{bmatrix} = \mathbf{s}d$ . Substituting this expression into equation 3.40, we have,

$$\mathbf{z} = \mathbf{H}\mathbf{u} + \mathbf{v} - \delta\mathbf{H}\mathbf{s}d \quad (3.41)$$

Finally, by assuming a ‘short’ (on the order of several minutes) approach duration, we can define the constant  $\mathbf{q} := -\delta\mathbf{H}\mathbf{s}$ . Substituting  $\mathbf{q}$  into equation 3.41 results in,

$$\mathbf{z} = \mathbf{H}\mathbf{u} + \mathbf{v} + \mathbf{q}d \quad (3.42)$$

where the fault vector is defined to be  $\mathbf{f} := \mathbf{q}d$ . Note that the fault varies linearly with distance to reference antenna because  $\mathbf{q}$  is constant [HP04]. So, the magnitude of the OEF vector  $\mathbf{f}$  linearly decreases to zero as the distance to rendezvous decreases. Therefore, its effect on the differential estimate error also gets eliminated at the rendezvous point.

The standard measurement equation form in the presence of a fault vector  $\mathbf{f}$  is given by,

$$\mathbf{z} = \mathbf{H}\mathbf{u} + \mathbf{v} + \mathbf{f} \quad (3.43)$$

In the presence of a fault, equation 2.17 becomes,

$$\begin{bmatrix} \mathbf{z}_{GF} \\ \phi \end{bmatrix} = \begin{bmatrix} \mathbf{0} & \mathbf{D}_{GF} \\ \mathbf{G} & \mathbf{D}_\phi \end{bmatrix} \begin{bmatrix} \mathbf{x} \\ \mathbf{n} \end{bmatrix} + \begin{bmatrix} \mathbf{v}_{GF} \\ \mathbf{v}_\phi \end{bmatrix} + \begin{bmatrix} \mathbf{0} \\ \mathbf{f}_\phi \end{bmatrix} \quad (3.44)$$

By definition, geometry free measurements  $\mathbf{z}_{GF}$  are unaffected by orbit ephemeris faults (because satellite geometry is eliminated from these measurements). So, only

the carrier measurements are affected by the fault. An orbit ephemeris fault is described by its mode and magnitude. The mode is defined to be the satellite which is affected by the fault. Since carrier measurements are stacked for all SVs, the mode corresponds to the non-zero element of  $\mathbf{f}_\phi$  (refer to Section 3.4.4). In this case, the fault magnitude is simply the value of the non-zero element of  $\mathbf{f}_\phi$ .

The fault vector  $\mathbf{f}$  impacts the position estimate error. To mitigate the fault impact, fault detection algorithms can be implemented. However, because the fault vector decreases with user-reference separatio distance, detecting a fault becomes a challenge as we see in Chapter 4.

**3.4.4 Orbit Ephemeris Fault Modelling.** In this work, the prior probability of an orbit ephemeris fault on any single SV is taken to be  $P(\mathbf{f}_1) = 10^{-5}$  (where  $\mathbf{f}_1$  is used to denote a single satellite fault) [oD08]. Since OEFs are rare occurrences, there are not enough real data samples to determine a fault distribution. Therefore, we cannot rely on a distribution to model OEFs, as we did for other error sources in this chapter. We have to take a worst case approach when dealing with OEFs.

The worst case approach involves considering all possible fault hypotheses, and finding the worst case, which maximizes integrity risk. All hypotheses would include faults on any visible SV, as well as any combination of faults on multiple visible SVs. To reduce the number of fault hypotheses,  $P(HMI)$  can be bounded by assuming that the probability of hazardous information given two or more simultaneous SV faults  $P(HMI | \mathbf{f}_{\geq 2}) \rightarrow 1$ . From equation 2.24 we can write this bound for the faulted case as,

$$\begin{aligned} P(HMI | F)P(F) &= P(HMI | \mathbf{f}_1)P(\mathbf{f}_1) + \overset{1}{P}(HMI | \mathbf{f}_{\geq 2})P(\mathbf{f}_{\geq 2}) \\ &\leq P(HMI | \mathbf{f}_1)P(\mathbf{f}_1) + P(\mathbf{f}_{\geq 2}) \end{aligned} \quad (3.45)$$

where,

$\mathbf{f}_1$  : denotes single SV fault

$\mathbf{f}_{\geq 2}$  : denotes two or more simultaneous satellite faults

provided that the probability of two or more simultaneous SV faults  $P(\mathbf{f}_{\geq 2})$  is less than the integrity risk requirement.

The fault may occur on any SV in view. We may bound the remaining single SV fault hypotheses in equation 3.45 as,

$$P(HMI | \mathbf{f}_1)P(\mathbf{f}_1) \leq P(\mathbf{f}_1) \sum_{i=1}^n \max_{\forall \|\mathbf{f}_1\| \in \mathbb{R}^+} P(HMI | {}^i\mathbf{f}_1) \quad (3.46)$$

where  $i$  indicates fault modes, and  $n$  is the number of visible SVs. Note that  $P(HMI)$  must be maximized with respect to all possible fault magnitudes to determine the ‘worst case’. Substituting equation 3.46 into equation 3.45 we obtain,

$$\underbrace{P(HMI | F)P(F)}_{\text{Faulted Integrity Risk}} \leq P(\mathbf{f}_1) \sum_{i=1}^n \max_{\forall \|\mathbf{f}_1\| \in \mathbb{R}^+} P(HMI | {}^i\mathbf{f}_1) + P(\mathbf{f}_{\geq 2}) \quad (3.47)$$

Equation 3.47 can be used to compute a bound on the integrity risk in the presence of orbit ephemeris faults.

## CHAPTER 4

### ORBIT EPHEMERIS FAULT DETECTION

This chapter analyzes new Receiver Autonomous Integrity Monitors (RAIM) against orbit ephemeris faults. In RAIM, integrity monitoring is done at the user end rather than at a reference station. RAIM methods take advantage of measurement redundancy to carry out fault detection. Three residual-based RAIM methods for detecting OEFs are discussed; differential RAIM (DRAIM), relative RAIM (RRAIM) and unified RAIM (URAIM). The expected performance of each algorithm is investigated from a theoretical point of view.

#### 4.1 Differential RAIM

Differential RAIM (DRAIM) is the designation given to the application of the traditional residual-based RAIM algorithm [Stu89] to differential measurements as expressed in equation 3.44. The residual-based test statistic is derived using the residual vector, which is defined as,

$$\mathbf{r} = [\mathbf{I} - \mathbf{HS}]\delta\mathbf{z} \quad (4.1)$$

where,

$\mathbf{r}$  : residual vector

$\mathbf{I}$  : identity matrix

$\delta\mathbf{z}$  : measurement error plus bias;  $\delta\mathbf{z} := \mathbf{v} + \mathbf{f}$

The residual vector can also be written as,

$$\mathbf{r} = [\mathbf{I} - \mathbf{HS}]\mathbf{z} \quad (4.2)$$

This is because the state observation term  $\mathbf{H}\mathbf{u}$  is cancelled out by the  $[\mathbf{I} - \mathbf{H}\mathbf{S}]$  matrix. It has been shown in [Stu89] that the residual computed using equation 4.2 is statistically independent from the state estimate error. This is because the residual is derived from components of the measurement vector laying in the parity space. Statistical independence is an important property to have because it facilitates computation of integrity risk, which is the ultimate goal in this work.

The residual-based test statistic  $q$  is defined to be the norm of the residual vector weighted by the inverse of the measurement noise covariance matrix  $\mathbf{V}$ .

$$q := \|\mathbf{r}\|_{\mathbf{V}^{-1}} = \mathbf{r}^T \mathbf{V}^{-1} \mathbf{r} \quad (4.3)$$

Since this test statistic is computed using the residual, it is also independent of state estimate error [WE95].

The test statistic  $q$  follows a non-central chi-square distribution. It is described by the non-centrality parameter (NCP) and number of degrees of freedom (dof). For  $\mathbf{H} \in \mathbb{R}^{n \times m}$ , the test statistic has  $n - m$  degrees of freedom. The NCP is,

$$\begin{aligned} NCP_q^2 &= \mathbf{f}^T [\mathbf{I} - \mathbf{H}\mathbf{S}]^T \mathbf{V}^{-1} [\mathbf{I} - \mathbf{H}\mathbf{S}] \mathbf{f} \\ &= \mathbf{f}^T \mathbf{V}^{-1} [\mathbf{I} - \mathbf{H}\mathbf{S}] \mathbf{f} \end{aligned} \quad (4.4)$$

The NCP equation 4.4 is a function of the fault vector. In Section 3.4.3 we showed that the fault magnitude linearly decreases to zero as the user approaches the reference at constant velocity. Therefore, the test statistic's NCP also tends toward zero near the rendezvous point. Essentially, this implies that as the user approaches the rendezvous point, the ability of DRAIM to detect an OEF decreases. This is the biggest weakness of DRAIM. On the other hand, the state estimate error also decreases when approaching the rendezvous point due to the decreasing fault magnitude.

In an attempt to improve RAIM performance near rendezvous, the Residual RAIM (RRAIM) method is investigated. We have seen that DRAIM computes the

residual test statistic using the same measurement equation that is used for estimation. In RRAIM a separate measurement equation, used solely for detection, is introduced.

## 4.2 Relative RAIM

The Relative RAIM (RRAIM) concept was introduced in [HP04]. The main idea is to exploit a synthetic baseline formed by the user's displacement towards the reference in order to improve detection capability. This baseline is created by triple differencing carrier measurements. To triple difference measurements, we begin by double differencing. Afterwards, measurements are time-differenced between two epochs, the current time and an initial reference epoch. This creates a new measurement equation for detection, which is different from that used for position estimation. The estimation measurement equation 3.44 contains filtered double difference geometry free measurements. These are not used for detection in RRAIM. Only the portion of the positioning equation that contains double differenced carrier phase measurements is used to derive the RRAIM test statistic.

At this point it is convenient to choose the initial/reference epoch used to define the RRAIM synthetic baseline. We choose the initial epoch to be the point at which the user enters the broadcast radius of the reference receiver. This choice is farthest from the rendezvous point, and provides the most time to filter GF measurements. It maximizes the synthetic baseline length at rendezvous. The larger the baseline length is, the better the detection capability [HP04]. But, in contrast with DRAIM, near the entrance to the broadcast radius, the synthetic baseline is much shorter and the detection capability of RRAIM is diminished. So, combining RRAIM with DRAIM will help improve detection at all points within the approach.

Now, to derive the RRAIM test statistic, consider the following equation 4.5.

$$\begin{bmatrix} \phi \end{bmatrix} = \begin{bmatrix} \mathbf{G} & \mathbf{D}_\phi \end{bmatrix} \begin{bmatrix} \mathbf{x} \\ \mathbf{n} \end{bmatrix} + \begin{bmatrix} \mathbf{v}_\phi \end{bmatrix} + \mathbf{f}_\phi \quad (4.5)$$

Equation 4.5 shows the portion of the biased estimation measurement equation (equation 3.44) without GF measurements. This equation is written for the current epoch and contains DD carrier phase measurements  $\phi$ . Time-differencing current time measurements from measurements at the initial time (initial epoch, denoted using subscript 0) results in,

$$\begin{aligned} \phi_0 - \phi &= \begin{bmatrix} \mathbf{G}_0 & \mathbf{D}_\phi \end{bmatrix} \begin{bmatrix} \mathbf{x}_0 \\ \mathbf{n} \end{bmatrix} + \mathbf{v}_{\phi,0} + \mathbf{f}_{\phi,0} - \begin{bmatrix} \mathbf{G} & \mathbf{D}_\phi \end{bmatrix} \begin{bmatrix} \mathbf{x} \\ \mathbf{n} \end{bmatrix} - \mathbf{v}_\phi - \mathbf{f}_\phi \\ &= \mathbf{G}_0 \mathbf{x}_0 + \mathbf{D}_\phi \mathbf{n} + \mathbf{v}_{\phi,0} + \mathbf{f}_{\phi,0} - \mathbf{G} \mathbf{x} - \mathbf{D}_\phi \mathbf{n} - \mathbf{v}_\phi - \mathbf{f}_\phi \\ &= \mathbf{G}_0 \mathbf{x}_0 - \mathbf{G} \mathbf{x} + \mathbf{v}_{\phi,0} - \mathbf{v}_\phi + \mathbf{f}_{\phi,0} - \mathbf{f}_\phi \end{aligned} \quad (4.6)$$

The integer ambiguities are eliminated from the newly formed measurement combination. This is one of the advantages of RRAIM. Adding and subtracting  $\mathbf{G} \mathbf{x}_0$  in equation 4.6, and then rearranging terms yields,

$$\begin{aligned} \phi_0 - \phi &= \mathbf{G}_0 \mathbf{x}_0 + (-\mathbf{G} \mathbf{x}_0 + \mathbf{G} \mathbf{x}_0) - \mathbf{G} \mathbf{x} + \mathbf{v}_{\phi,0} - \mathbf{v}_\phi + \mathbf{f}_{\phi,0} - \mathbf{f}_\phi \\ \phi_\Delta &= \mathbf{G}_\Delta \mathbf{x}_0 + \mathbf{G} \mathbf{x}_\Delta + \mathbf{v}_{\phi,\Delta} + \mathbf{f}_{\phi,\Delta} \end{aligned} \quad (4.7)$$

where the subscript  $\Delta$  is used to denote differencing of measurements at current time from measurements at the initial time. In general, the change in the observation matrix  $\mathbf{G}_\Delta$  may not be neglected. For short mission duration it may be acceptable to do so. But, rendezvous applications may last several minutes from service volume entry to the rendezvous point. For example, the LOS to the SVs will change by roughly 1.5 degrees in 6 minutes. This is considered significant, and warrants keeping the  $\mathbf{G}_\Delta$  term. However, the true initial position  $\mathbf{x}_0$  in equation 4.7 is not known. It can either be estimated along with the relative baseline  $\mathbf{x}_\Delta$ , or an estimate of the initial position may be computed using the measurement equation 3.44.

Here, we choose the second option, and attempt to substitute the initial position estimate into equation 4.7. First let us write the measurement equation used for positioning for the initial epoch 0. Equation 3.44 is shown below using standard measurement equation notation.

$$\mathbf{z}_0 = \mathbf{H}_0 \mathbf{u}_0 + \mathbf{v}_0 + \mathbf{f}_0$$

Subscript 0 is used to denote the initial epoch. Then, the state estimate error may be written as,

$$\delta \mathbf{u}_0 = \mathbf{S}_0 (\mathbf{f}_0 + \mathbf{v}_0) \quad \text{where:} \quad \mathbf{S}_0 = (\mathbf{H}_0^T \mathbf{V}_0^{-1} \mathbf{H}_0)^{-1} \mathbf{H}_0^T \mathbf{V}_0^{-1}$$

Now, we can write the true initial position in terms of a state estimate vector and an error vector (using the definition of estimate error from equation 2.21). We are only interested in the position states  $\mathbf{x}_0$ , which correspond to the first three states in the state vector  $\mathbf{u}_0$ . Thus, we use the first three rows of the weighted pseudoinverse matrix  $\mathbf{S}_{0,r1:3}$  at the initial epoch to extract these states.

$$\begin{aligned} \mathbf{x}_0 &:= \hat{\mathbf{x}}_0 - \delta \mathbf{x}_0 \\ &= \hat{\mathbf{x}}_0 - \mathbf{S}_{0,r1:3} (\mathbf{f}_0 + \mathbf{v}_0) \end{aligned} \tag{4.8}$$

where,

$\mathbf{S}_{0,r1:3}$  : first three rows of the weighted pseudoinverse at the initial epoch

Then, substituting equation 4.8 into equation 4.7 and rearranging terms, the measurement equation used to derive the detection test statistic becomes the following,

$$\begin{aligned} \phi_\Delta &= \mathbf{G}_\Delta \mathbf{x}_0 + \mathbf{G} \mathbf{x}_\Delta + \mathbf{v}_{\phi,\Delta} + \mathbf{f}_{\phi,\Delta} \\ &= \mathbf{G}_\Delta (\hat{\mathbf{x}}_0 - \mathbf{S}_{0,r1:3} (\mathbf{f}_0 + \mathbf{v}_0)) + \mathbf{G} \mathbf{x}_\Delta + \mathbf{v}_{\phi,\Delta} + \mathbf{f}_{\phi,\Delta} \\ \phi_\Delta - \mathbf{G}_\Delta \hat{\mathbf{x}}_0 &= -\mathbf{G}_\Delta \mathbf{S}_{0,r1:3} (\mathbf{f}_0 + \mathbf{v}_0) + \mathbf{G} \mathbf{x}_\Delta + \mathbf{v}_{\phi,\Delta} + \mathbf{f}_{\phi,\Delta} \\ &= \mathbf{G} \mathbf{x}_\Delta + (\mathbf{v}_{\phi,\Delta} - \mathbf{G}_\Delta \mathbf{S}_{0,r1:3} \mathbf{v}_0) + (\mathbf{f}_{\phi,\Delta} - \mathbf{G}_\Delta \mathbf{S}_{0,r1:3} \mathbf{f}_0) \end{aligned}$$

Finally, we have,

$$\mathbf{z}_\Delta = \mathbf{G}\mathbf{x}_\Delta + \mathbf{v}_\Delta + \mathbf{f}_\Delta \quad (4.9)$$

where:

$$\begin{aligned} \mathbf{z}_\Delta &:= \boldsymbol{\phi}_\Delta - \mathbf{G}_\Delta \hat{\mathbf{x}}_0 \\ \mathbf{v}_\Delta &:= (\mathbf{v}_{\phi,\Delta} - \mathbf{G}_\Delta \mathbf{S}_{0,r1:3} \mathbf{v}_0) \\ \mathbf{f}_\Delta &:= (\mathbf{f}_{\phi,\Delta} - \mathbf{G}_\Delta \mathbf{S}_{0,r1:3} \mathbf{f}_0) \end{aligned}$$

Equation 4.9 is used to derive the relative RAIM test statistic in the case where  $\mathbf{G}_\Delta$  is not negligible.

Next we want to write the measurement noise covariance matrix for  $\mathbf{v}_\Delta$ . This is needed to determine if there exists a correlation between the residual-based test statistic derived from equation 4.9, and the estimate error in equation 3.44. First some useful transformations are introduced, which relate the terms in equation 4.9 to those in equation 3.44.

We wish to write the measurement noise vector  $\mathbf{v}_\Delta$  in equation 4.9 in terms of the noise  $\mathbf{v}$  in equation 3.44. First, we need the ability to extract carrier measurement noise  $\mathbf{v}_\phi$  from the full measurement equation noise  $\mathbf{v}$ . Let the observation matrices for estimation and detection respectively be,  $\mathbf{H} \in \mathbb{R}^{n \times m}$  and  $\mathbf{G} \in \mathbb{R}^{p \times 3}$ . Equations 4.10 and 4.11 show how  $\mathbf{v}_\phi$  and  $\mathbf{f}_\phi$  are extracted from  $\mathbf{v}$  and  $\mathbf{f}$  using the matrix,  $\mathbf{E}$ .

$$\mathbf{v}_\phi = \mathbf{E}\mathbf{v} \quad (4.10)$$

$$\mathbf{f}_\phi = \mathbf{E}\mathbf{f} \quad (4.11)$$

$$\text{where: } \mathbf{E} = \begin{bmatrix} \mathbf{0} & \mathbf{I}_p \end{bmatrix}_{p \times n} \quad (4.12)$$

In addition, the weighted pseudoinverse and observation matrices can be expressed as,

$$\mathbf{S}_{0,r1:3} = \mathbf{E}_3 \mathbf{S}_0 \quad (4.13)$$

$$\mathbf{G} = \mathbf{E}\mathbf{H}\mathbf{E}_3^T \quad (4.14)$$

$$\text{where: } \mathbf{E}_3 = \begin{bmatrix} \mathbf{I}_3 & \mathbf{0} \end{bmatrix}_{3 \times m} \quad (4.15)$$

Using these transformations, we can write the measurement covariance matrix for  $\mathbf{z}_\Delta$  in equation 4.9 in terms of the covariance matrix for the measurement in equation 3.44.

#### 4.2.1 Relative Fault Vector and Noise Covariance Matrix Derivation.

Using equations 4.10 and 4.11, noise and fault vectors  $\mathbf{v}_\Delta$  and  $\mathbf{f}_\Delta$  may respectively be written as,

$$\begin{aligned} \mathbf{v}_\Delta &= \mathbf{v}_{\phi,\Delta} - \mathbf{G}_\Delta \mathbf{E}_3 \mathbf{S}_0 \mathbf{v}_0 \\ &= [\mathbf{E} - \mathbf{G}_\Delta \mathbf{E}_3 \mathbf{S}_0] \mathbf{v}_0 - \mathbf{E} \mathbf{v} \end{aligned} \quad (4.16)$$

$$\mathbf{f}_\Delta = [\mathbf{E} - \mathbf{G}_\Delta \mathbf{E}_3 \mathbf{S}_0] \mathbf{f}_0 - \mathbf{E} \mathbf{f} \quad (4.17)$$

The measurement noise covariance matrix  $\mathbf{V}_\Delta$  is computed, using the expected value operator, as,

$$\begin{aligned} \mathbf{V}_\Delta &= E\{\mathbf{v}_\Delta \mathbf{v}_\Delta^T\} \\ &= E\{([\mathbf{E} - \mathbf{G}_\Delta \mathbf{E}_3 \mathbf{S}_0] \mathbf{v}_0 - \mathbf{E} \mathbf{v})([\mathbf{E} - \mathbf{G}_\Delta \mathbf{E}_3 \mathbf{S}_0] \mathbf{v}_0 - \mathbf{E} \mathbf{v})^T\} \\ &= [\mathbf{E} - \mathbf{G}_\Delta \mathbf{E}_3 \mathbf{S}_0] \mathbf{V}_0 [\mathbf{E} - \mathbf{G}_\Delta \mathbf{E}_3 \mathbf{S}_0]^T + \mathbf{E} \mathbf{V} \mathbf{E}^T - \mathbf{V}_{corr} \end{aligned} \quad (4.18)$$

$$\text{where: } \mathbf{V}_{corr} = [\mathbf{E} - \mathbf{G}_\Delta \mathbf{E}_3 \mathbf{S}_0] E\{\mathbf{v}_0 \mathbf{v}_0^T\} \mathbf{E}^T + \mathbf{E} E\{\mathbf{v} \mathbf{v}^T\} [\mathbf{E} - \mathbf{G}_\Delta \mathbf{E}_3 \mathbf{S}_0]^T$$

$\mathbf{V}_\Delta$  is expressed in terms of  $\mathbf{V}$ ,  $\mathbf{V}_0$ , and  $\mathbf{V}_{corr}$ . The two terms in  $\mathbf{V}_{corr}$  represent the measurement noise time-correlation between initial time (epoch 0) and current time.

**4.2.2 Relative Residual.** The relative residual vector  $\mathbf{r}_\Delta$  can be expressed by applying equation 4.2 to equation 4.9.

$$\mathbf{r}_\Delta = [\mathbf{I} - \mathbf{G} \mathbf{S}_\Delta] \delta \mathbf{z}_\Delta \quad (4.19)$$

$$= [\mathbf{I} - \mathbf{G} \mathbf{S}_\Delta] \mathbf{z}_\Delta \quad (4.20)$$

The RRAIM test statistic can be defined as the norm of the residual vector weighted by the inverse of the measurement error covariance matrix.

$$\begin{aligned}\|\mathbf{r}_\Delta\|^2 &= \mathbf{r}_\Delta^T \mathbf{V}_\Delta^{-1} \mathbf{r}_\Delta \\ &= \mathbf{z}_\Delta^T \mathbf{V}_\Delta^{-1} [\mathbf{I} - \mathbf{G}\mathbf{S}_\Delta] \mathbf{z}_\Delta\end{aligned}\quad (4.21)$$

It is non-centrally chi-square distributed and is described by the number of degrees of freedom  $dof$ , and non-centrality-parameter  $NCP$ . Depending on which implementation is used (WL or L1L2), we have,

$$\begin{aligned}\text{WL: } dof &= (n - 1) - 3 = n - 4 \quad \text{where } n \text{ is the number of SVs} \\ \text{L1L2: } dof &= 2(n - 1) - 3 = 2n - 5 \\ NCP^2 &= \mathbf{f}_\Delta^T \mathbf{V}_\Delta^{-1} [\mathbf{I} - \mathbf{G}\mathbf{S}_\Delta] \mathbf{f}_\Delta\end{aligned}\quad (4.22)$$

**4.2.3 Test Statistic Correlation.** In this section, it is shown that the RRAIM test statistic is correlated with the state estimate error. To prove this, a similar procedure to that presented in [Per96] is followed.

For the time being, assume that measurement error  $\mathbf{v}$  in equation 3.44 is independent and identically distributed (i.i.d.). The measurement error  $\delta\mathbf{z}$  (where  $\delta\mathbf{z} := \mathbf{v} + \mathbf{f}$ ) is expressed in terms of two orthogonal components,

$$\begin{aligned}\mathbf{z} &= \mathbf{H}\mathbf{u} + \delta\mathbf{z} \\ &= \mathbf{H}\mathbf{u} + (\delta\mathbf{z}_\parallel + \delta\mathbf{z}_\perp)\end{aligned}$$

where:  $\delta\mathbf{z}_\parallel$  is in range space of  $\mathbf{H}$

$\delta\mathbf{z}_\perp$  is a null vector of  $\mathbf{H}^T$

So,  $\delta\mathbf{z}_\parallel$  and  $\delta\mathbf{z}_\perp$  are derived from orthogonal components of the measurement error vector  $\delta\mathbf{z}$ . Similarly, for the initial epoch (denoted using subscript 0) we may write,

$$\mathbf{z}_0 = \mathbf{H}_0 \mathbf{u}_0 + (\delta\mathbf{z}_{\parallel,0} + \delta\mathbf{z}_{\perp,0})$$

where:  $\delta\mathbf{z}_{\parallel,0}$  is in range space of  $\mathbf{H}_0$

$\delta\mathbf{z}_{\perp,0}$  is null vector of  $\mathbf{H}_0^T$

Using the assumption of i.i.d. measurement noise, the position state estimate error vector at current time may be written as,

$$\delta\mathbf{x} = \mathbf{E}_3\mathbf{S}(\delta\mathbf{z}_{\parallel} + \delta\mathbf{z}_{\perp}) = \mathbf{E}_3(\mathbf{H}^T\mathbf{H})^{-1}\mathbf{H}^T\delta\mathbf{z}_{\parallel} \quad (4.23)$$

From equation 4.23, we see that the position estimate error is only a function of  $\delta\mathbf{z}_{\parallel}$ . Thus, in order for the residual to be independent of the state estimate error, it must be derived from  $\delta\mathbf{z}_{\perp}$ , the component orthogonal to  $\delta\mathbf{z}_{\parallel}$ .

To write the residual, we first we need the measurement  $\mathbf{z}_{\Delta}$ . Substitute equation 4.13 into equation 4.9, and using the orthogonal measurement error notation, we obtain,

$$\begin{aligned} \mathbf{z}_{\Delta} &= \mathbf{G}\mathbf{x}_{\Delta} + [\mathbf{E} - \mathbf{G}_{\Delta}\mathbf{S}_{0,r1:3}](\mathbf{v}_0 + \mathbf{f}_0) - \mathbf{E}(\mathbf{v} + \mathbf{f}) \\ &= \mathbf{G}\mathbf{x}_{\Delta} + [\mathbf{E} - \mathbf{G}_{\Delta}\mathbf{E}_3\mathbf{S}_0](\delta\mathbf{z}_{\parallel,0} + \delta\mathbf{z}_{\perp,0}) - \mathbf{E}(\delta\mathbf{z}_{\parallel} + \delta\mathbf{z}_{\perp}) \end{aligned} \quad (4.24)$$

Now, substituting equation 4.24 into equation 4.20, and simplifying, we have,

$$\begin{aligned} \mathbf{r}_{\Delta} &= [\mathbf{I} - \mathbf{G}\mathbf{S}_{\Delta}]\mathbf{z}_{\Delta} \\ &= [\mathbf{I} - \mathbf{G}\mathbf{S}_{\Delta}]\{[\mathbf{E} - \mathbf{G}_{\Delta}\mathbf{E}_3\mathbf{S}_0](\delta\mathbf{z}_{\parallel,0} + \delta\mathbf{z}_{\perp,0}) - \mathbf{E}(\delta\mathbf{z}_{\parallel} + \delta\mathbf{z}_{\perp})\} \end{aligned} \quad (4.25)$$

where,

$$\mathbf{S}_{\Delta} = (\mathbf{G}^T\mathbf{V}_{\Delta}^{-1}\mathbf{G})^{-1}\mathbf{G}^T\mathbf{V}_{\Delta}^{-1} \quad (4.26)$$

$$= (\mathbf{E}_3\mathbf{H}^T\mathbf{E}^T\mathbf{V}_{\Delta}^{-1}\mathbf{E}\mathbf{H}\mathbf{E}_3^T)^{-1}\mathbf{E}_3\mathbf{H}^T\mathbf{E}^T\mathbf{V}_{\Delta}^{-1} \quad (4.27)$$

Note that the measurements used in position estimation are assumed to be i.i.d., but the RRAIM measurement noise covariance matrix  $\mathbf{V}_{\Delta}$  will not be a diagonal

matrix. This is because of the matrix manipulations involved in forming  $\mathbf{V}_\Delta$  using equation 4.18.

First, consider the  $\delta\mathbf{z}_\parallel$  terms in equation 4.25, since they appear in the position error equation 4.23. Define,

$$\mathbf{r}_1 := -\mathbf{E}\delta\mathbf{z}_\parallel + \mathbf{G}\mathbf{S}_\Delta\mathbf{E}\delta\mathbf{z}_\parallel$$

Using the notation  $\delta\mathbf{z}_\parallel = \mathbf{H}\mathbf{y}$  (where  $\mathbf{y}$  can be any vector) to model the fact that  $\delta\mathbf{z}_{\parallel,k} \in \text{Image}\{\mathbf{H}\}$ , we have,

$$\mathbf{r}_1 = -\mathbf{E}\mathbf{H}\mathbf{y} + \mathbf{G}\mathbf{S}_\Delta\mathbf{E}\mathbf{H}\mathbf{y}$$

Substituting equation 4.14 for  $\mathbf{G}$  and equation 4.27 for  $\mathbf{S}_\Delta$  we obtain,

$$\begin{aligned} \mathbf{r}_1 &= -\mathbf{E}\mathbf{H}\mathbf{y} + \mathbf{E}\mathbf{H}\mathbf{E}_3^T\mathbf{S}_\Delta\mathbf{E}\mathbf{H}\mathbf{y} \\ &= -\mathbf{E}\mathbf{H}\mathbf{y} + \mathbf{E}\mathbf{H}\mathbf{E}_3^T(\mathbf{E}_3\mathbf{H}^T\mathbf{E}^T\mathbf{V}_\Delta^{-1}\mathbf{E}\mathbf{H}\mathbf{E}_3^T)^{-1}\mathbf{E}_3\mathbf{H}^T\mathbf{E}^T\mathbf{V}_\Delta^{-1}\mathbf{E}\mathbf{H}\mathbf{y} \\ &\neq 0 \end{aligned}$$

The resultant  $\mathbf{r}_1$  is not equal to zero. Therefore, the state estimate error vector  $\delta\mathbf{x}$  is correlated with the residual vector  $\mathbf{r}_\Delta$ .

Since the residual has already been shown to be correlated with the state estimate error, the development could stop here. However, for the sake of completeness we show the result for  $\delta\mathbf{z}_{\parallel,0}$  terms in equation 4.25,

$$\mathbf{r}_2 := -\mathbf{G}_\Delta\mathbf{E}_3\mathbf{S}_0\delta\mathbf{z}_{\parallel,0} + \mathbf{E}\delta\mathbf{z}_{\parallel,0} + \mathbf{G}\mathbf{S}_\Delta\{\mathbf{G}_\Delta\mathbf{E}_3\mathbf{S}_0\delta\mathbf{z}_{\parallel,0} - \mathbf{E}\delta\mathbf{z}_{\parallel,0}\}$$

Using the notation  $\delta\mathbf{z}_{\parallel,0} = \mathbf{H}_0\mathbf{y}_0$  (where  $\mathbf{y}_0$  can be any vector) to model the fact that  $\delta\mathbf{z}_{\parallel,0} \in \text{Image}\{\mathbf{H}_0\}$ , it can be shown that,

$$\begin{aligned} \mathbf{r}_2 &= -\mathbf{E}\mathbf{H}_0\mathbf{E}_3^T\mathbf{E}_3\mathbf{y}_0 + \mathbf{E}\mathbf{H}\mathbf{E}_3^T(\mathbf{S}_\Delta\mathbf{E}\mathbf{H}_0\mathbf{E}_3^T)\mathbf{E}_3\mathbf{y}_0 + \mathbf{E}\mathbf{H}_0\mathbf{y}_0 - \mathbf{G}\mathbf{S}_\Delta\mathbf{E}\mathbf{H}_0\mathbf{y}_0 \\ &\neq 0 \end{aligned}$$

In general, this term also causes correlation between  $\delta\mathbf{x}$  and  $\mathbf{r}_\Delta$ .

We have demonstrated that correlation exists between the RRAIM residual  $\mathbf{r}_\Delta$ , and the estimate error  $\delta\mathbf{x}$ , even for the simplified case of i.i.d. measurements. In reality, the i.i.d. assumption is not true, especially considering the content of Chapter 3. If the residual and estimate error are correlated under the i.i.d. assumption, they will most certainly be when measurement correlations are introduced. Therefore, the test statistic generated using this residual will also be correlated with the state estimate error. As we will see in Section 5.1, statistical independence between test statistic and state estimate error facilitates the computation of integrity risk.

Further developments in Appendix D and Appendix E show that RRAIM cannot be implemented individually for OEF detection and monitoring. Instead of using RRAIM and DRAIM separately, a new idea called Unified RAIM (URAIM) is pursued. This concept seamlessly transitions between RRAIM and DRAIM.

### 4.3 Unified RAIM Concept

The concept of URAIM combines DRAIM and RRAIM using a single measurement equation with a state vector that includes the initial position state,  $\mathbf{x}_0$ . Instead of estimating  $\mathbf{x}_0$  separately as in equations 4.8 and 4.7,  $\mathbf{x}_0$  is estimated here along with current position and cycle ambiguity states. A single measurement equation is needed, which eliminates the correlation between residual and estimate error. Since URAIM combines DRAIM and RRAIM, it provides detection capability at all points within an approach.

The derivation of the URAIM measurement equation is similar to that of RRAIM. It starts with the triple differenced carrier in equation 4.6. In this case, we add and subtract  $\mathbf{G}_0\mathbf{x}$  (as opposed to  $\mathbf{G}\mathbf{x}_0$  for RRAIM),

$$\phi_\Delta = \mathbf{G}_0\mathbf{x}_0 - \mathbf{G}\mathbf{x} + \mathbf{v}_{\phi,\Delta} + \mathbf{f}_{\phi,\Delta}$$

$$\begin{aligned}
&= \mathbf{G}_0 \mathbf{x}_0 + (-\mathbf{G}_0 \mathbf{x} + \mathbf{G}_0 \mathbf{x}) - \mathbf{G}_k \mathbf{x} + \mathbf{v}_{\phi, \Delta} + \mathbf{f}_{\phi, \Delta} \\
&= \mathbf{G}_0 \mathbf{x}_\Delta + \mathbf{G}_\Delta \mathbf{x} + \mathbf{v}_{\phi, \Delta} + \mathbf{f}_{\phi, \Delta}
\end{aligned} \tag{4.28}$$

Combining equations 4.28 with 3.44 we can write the following measurement equation,

$$\begin{bmatrix} \mathbf{z}_{GF} \\ \phi \\ \phi_\Delta \end{bmatrix} = \begin{bmatrix} \mathbf{0} & \mathbf{D}_{GF} & \mathbf{0} \\ \mathbf{G} & \mathbf{D}_\phi & \mathbf{0} \\ \mathbf{G}_\Delta & \mathbf{0} & \mathbf{G}_0 \end{bmatrix} \begin{bmatrix} \mathbf{x} \\ \mathbf{n} \\ \mathbf{x}_\Delta \end{bmatrix} + \begin{bmatrix} \mathbf{v}_{GF} \\ \mathbf{v}_\phi \\ \mathbf{v}_{\phi, \Delta} \end{bmatrix} + \begin{bmatrix} \mathbf{0} \\ \mathbf{f}_\phi \\ \mathbf{f}_{\phi, \Delta} \end{bmatrix} \tag{4.29}$$

As an alternative, we can simply augment equation 3.44 with the double-difference carrier measurements at the initial time,

$$\begin{bmatrix} \mathbf{z}_{GF} \\ \phi \\ \phi_0 \end{bmatrix} = \begin{bmatrix} \mathbf{0} & \mathbf{D}_{GF} & \mathbf{0} \\ \mathbf{G} & \mathbf{D}_\phi & \mathbf{0} \\ \mathbf{0} & \mathbf{D}_\phi & \mathbf{G}_0 \end{bmatrix} \begin{bmatrix} \mathbf{x} \\ \mathbf{n} \\ \mathbf{x}_0 \end{bmatrix} + \begin{bmatrix} \mathbf{v}_{GF} \\ \mathbf{v}_\phi \\ \mathbf{v}_{\phi, 0} \end{bmatrix} + \begin{bmatrix} \mathbf{0} \\ \mathbf{f}_\phi \\ \mathbf{f}_{\phi, 0} \end{bmatrix} \tag{4.30}$$

The outcome of least squares estimation is the same. This formulation is preferred due to its simplicity. It is worth noting that in order to have common cycle ambiguity states for both current and initial epoch carrier measurements, we have to use the SVs common to both epochs. Also, the fault is assumed to impact measurements at both initial and current epochs. It is of course possible that a fault may occur during an approach. The measurement noise covariance matrix for equation 4.30 has been derived in Chapter 3.

Equation 4.30 will be used in the remainder of this thesis, and referred to as the URAIM measurement equation. The most important advantage of URAIM is that it guarantees the independence between estimate error and test statistic. This is because the URAIM measurement equation will be used for both position estimation and fault detection. In this case, residual-based RAIM guarantees independence between residual and estimate error [Stu89]. It also provides a seamless transition between DRAIM and RRAIM. Again, DRAIM is expected to be more effective far

away from the rendezvous point (near the entrance to the broadcast radius). In contrast, RRAIM is expected to be more effective near the rendezvous point.

## CHAPTER 5

## UNIFIED RAIM FOR FIXED SOLUTION USING EPIC

In this chapter, the Unified RAIM algorithm for a fixed solution is investigated using the EPIC-light integrity risk bounding method. As previously mentioned, applications requiring high accuracy and high integrity demand that cycle ambiguities be fixed in order to satisfy stringent accuracy requirements.

In Chapter 2 the fault-free EPIC-light algorithm was discussed. In this chapter, EPIC-light is implemented in conjunction with URAIM against orbit ephemeris faults. In addition, we will see the effect of fixing integers on the integrity risk evaluation. The integrity risk bound is modified to include the faulted scenario and the set of cycle ambiguity fix candidates is modified (as compared to the fault-free set) to account for the measurement fault.

### 5.1 Modifying the Integrity Risk Bound

The integrity risk for the faulted case is developed from equation 2.25. In Chapter 2 we focused on the first term in the summation involving  $P(HMI | \bar{F}, \boldsymbol{\eta})$ . Here, we are concerned with the faulted portion, which is the  $P(HMI | F, \boldsymbol{\eta})$  term.

$$P(HMI | F) := \sum_{\boldsymbol{\eta} \in \mathbb{Z}^k} P(HMI | F, \boldsymbol{\eta}) P(\check{\mathbf{n}} = \boldsymbol{\eta} | F) \quad (5.1)$$

Again, we choose to only evaluate the integrity risk for a subset of the complete integer space, which we call the candidate region,  $C \subset \mathbb{Z}^k$ . The summation in equation 5.1 is now divided between the candidate region,  $C$ , and its complement,  $\bar{C}$ .

$$\begin{aligned} P(HMI | F) &= \sum_{\boldsymbol{\eta} \in C} P(HMI | F, \boldsymbol{\eta}) P(\check{\mathbf{n}} = \boldsymbol{\eta} | F) \\ &\quad + \sum_{\boldsymbol{\eta} \in \bar{C}} P(HMI | F, \boldsymbol{\eta}) P(\check{\mathbf{n}} = \boldsymbol{\eta} | F) \end{aligned} \quad (5.2)$$

We plan to apply a conservative bound for fixing outside the candidate region, similar to that of the fault free case in equation 2.31. However, in the presence of faults, an integrity monitor (URAIM) is implemented to mitigate the fault impact on the state estimate error  $\delta\mathbf{u}$ . Now that URAIM is being used for fault detection, the definition of  $P(HMI)$  needs to be changed. Instead of equation 2.30, which is just the probability of the error exceeding the alert limit,  $P(HMI)$  is defined as a joint probability,

$$P(HMI | F, \boldsymbol{\eta}) = P(|\delta\check{\mathbf{x}}_x| > \ell, q < R_c | F, \check{\mathbf{n}} = \boldsymbol{\eta}) \quad (5.3)$$

where :  $\delta\check{\mathbf{x}}_x \sim N(\mathbf{b}_x(\mathbf{f}, \boldsymbol{\eta}), \sigma_x^2)$

where,

$\delta\check{\mathbf{x}}_x$  : position error corresponding to state  $x$

$q$  : residual-based test statistic

$R_c$  : detection threshold

$\mathbf{b}_x(\mathbf{f}, \boldsymbol{\eta})$  : position domain bias (which is a function of fault and fix candidate) corresponding to state  $x$ ; Details in Section 5.3

$\sigma_x$  : standard deviation of position error for state  $x$

The distribution of position state  $\delta\check{\mathbf{x}}_x$  is derived in Section 5.3. The RAIM detection threshold  $R_c$  is set to comply with the continuity requirements [Stu89]. Note that the only way  $P(HMI | F, \boldsymbol{\eta})$  can be written as a product of probabilities is if the test statistic  $q$  and estimate error  $\delta\check{\mathbf{x}}_x$  are statistically independent. If it is not, then the joint probability in equation 5.3 must be computed. This is the reason why we went to such great lengths in Chapter 4 to ensure independence between  $q$  and  $\delta\check{x}_{|K}$ . Using the URAIM measurement equation, we can write,

$$\begin{aligned} P(HMI | F, \boldsymbol{\eta}) &= P(|\delta\check{\mathbf{x}}_x| > \ell | F, \check{\mathbf{n}} = \boldsymbol{\eta})P(q < R_c | F) \\ &= P(HI | F, \boldsymbol{\eta})P(ND | F) \end{aligned} \quad (5.4)$$

$$\begin{aligned} \text{where,} \quad & P(HI | F, \boldsymbol{\eta}) := P(|\delta \check{\mathbf{x}}_x| > \ell | F, \check{\mathbf{n}} = \boldsymbol{\eta}) \\ & P(ND | F) := P(q < R_c | F) \end{aligned}$$

Note that the probability of no detection  $P(ND | F)$  is unaffected by fixing cycle ambiguities because the test statistic is derived from the ‘float’ residual.

We can write  $P(HMI)$  in equation 5.2 using equation 5.4, and we can apply the conservative assumption that  $P(HI) \rightarrow 1$  when we fix outside the chosen candidate set. (This produces a tighter bound on integrity risk than assuming  $P(HMI) \rightarrow 1$ .)

$$\begin{aligned} P(HMI | F) &= \sum_{\boldsymbol{\eta} \in C} P(HI | F, \boldsymbol{\eta}) P(ND | F) P(\check{\mathbf{n}} = \boldsymbol{\eta} | F) \\ &\quad + \sum_{\boldsymbol{\eta} \in \bar{C}} P(HI | F, \boldsymbol{\eta}) P(ND | F) P(\check{\mathbf{n}} = \boldsymbol{\eta} | F) \\ &\leq P(ND | F) \sum_{\boldsymbol{\eta} \in C} P(HI | F, \boldsymbol{\eta}) P(\check{\mathbf{n}} = \boldsymbol{\eta} | F) \\ &\quad + P(ND | F) \sum_{\boldsymbol{\eta} \in \bar{C}} P(\check{\mathbf{n}} = \boldsymbol{\eta} | F) \end{aligned} \quad (5.5)$$

Now, since integer spaces  $C$  and  $\bar{C}$  are complements, the substitution

$$\sum_{\boldsymbol{\eta} \in \bar{C}} P(\check{\mathbf{n}} = \boldsymbol{\eta} | F) = 1 - \sum_{\boldsymbol{\eta} \in C} P(\check{\mathbf{n}} = \boldsymbol{\eta} | F) \quad (5.6)$$

is made. Equation 5.5 becomes,

$$\begin{aligned} P(HMI | F) &\leq P(ND | F) \sum_{\boldsymbol{\eta} \in C} P(HI | F, \boldsymbol{\eta}) P(\check{\mathbf{n}} = \boldsymbol{\eta} | F) \\ &\quad + P(ND | F) \left( 1 - \sum_{\boldsymbol{\eta} \in C} P(\check{\mathbf{n}} = \boldsymbol{\eta} | F) \right) \\ &\leq P(ND | F) \left( 1 - \sum_{\boldsymbol{\eta} \in C} \left( 1 - P(HI | F, \boldsymbol{\eta}) \right) P(\check{\mathbf{n}} = \boldsymbol{\eta} | F) \right) \end{aligned} \quad (5.7)$$

In the presence of an OEF, equation 5.7 provides an upper bound on the integrity risk. The integrity risk is guaranteed to be bounded, regardless of our choice of integer candidate subset  $C$ . In general, a larger subset  $C$  will produce a tighter

bound. However, choosing subset  $C$  is not as straightforward as it was for the fault free case. This is because an OEF results in a measurement bias which offsets the set of most likely candidates. There are times where we will not fix correctly because the fault has affected the integer fixing procedure. In these situations, we don't know what the correct fix is. So, we cannot center our distribution about this fix.

## 5.2 Modifying the Integer Candidate Subset Selection

In Chapter 2 the fault-free integer candidate subset was defined by its center and its size (or extent), which could be determined numerically. In the presence of a fault, the extent is still determined through simulation. However, the center is no longer the correct fix as it was in the fault-free scenario. Large faults may cause the probability distribution  $P(\check{\mathbf{n}} = \boldsymbol{\eta} | F)$  in equation 5.7 to shift significantly. If the probability of fixing to within the selected candidate subset is low, then a very loose bound is obtained on the integrity risk, which can cause poor system availability.

To account for the effect of the bias, we need a new method of defining the center of the candidate set. We want to choose the region  $C$  which gives the tightest possible bound on integrity risk. Therefore, we would like to have  $C$  be the following,

$$C = \arg \max_C \sum_{\boldsymbol{\eta} \in C} \left(1 - P(HI | F, \boldsymbol{\eta})\right) P(\check{\mathbf{n}} = \boldsymbol{\eta} | F) \quad (5.8)$$

Since the extent of  $C$  can be determined through simulation, we may simplify equation 5.8 to maximize over the center of the candidate set,  $\boldsymbol{\psi}$ , rather than the entire set  $C$ .

$$\boldsymbol{\psi} = \arg \max_{\boldsymbol{\eta}} \left(1 - P(HI | F, \boldsymbol{\eta})\right) P(\check{\mathbf{n}} = \boldsymbol{\eta} | F) \quad (5.9)$$

Equation 5.9 expresses the fact that we want to minimize  $P(HI | F, \boldsymbol{\eta})$  while simultaneously maximizing  $P(\check{\mathbf{n}} = \boldsymbol{\eta} | F)$ . Equation 5.9 is especially difficult to solve because the fault magnitude is a varying parameter in residual-based RAIM. Fortunately, an

approximate solution to equation 5.9 can be found by only considering  $P(\check{\mathbf{n}} = \boldsymbol{\eta} | F)$  in the optimization. The idea is to center the candidate set about the fix with the highest probability of occurrence, which we refer to as the most likely fix (MLF).

$$\boldsymbol{\eta}_{MLF} = \arg \max_{\boldsymbol{\eta}} P(\check{\mathbf{n}} = \boldsymbol{\eta} | F)$$

where,

$\boldsymbol{\eta}_{MLF}$  : center of candidate set corresponding to MLF for a given fault mode and magnitude

To further simplify this method, the integer candidate set is centered about the noise free fix (NFF)  $\boldsymbol{\eta}_{NFF}$  which is the integer fix we would obtain as a result of propagating the fault through the fixing process in the absence of measurement noise. The NFF has been numerically verified to be equivalent to the MLF roughly 90 percent of the time. The NFF-based integrity risk bound may be slightly looser in the remaining 10 percent of cases [JKSP12]. For URAIM using EPIC-light, we will center the candidate set about the NFF and determine the candidate range through numerical simulation.

When choosing a candidate set in the presence of a bias and noise, we have made several simplifications, which can inflate the bound on the integrity risk. Choosing a large enough candidate space will mitigate the effect of these conservative assumptions, hence providing a tight bound on the integrity risk at the cost of increasing the computational burden.

### 5.3 Impact on Position Domain

The impact of fix candidates on the position estimate error was presented for the fault-free case in Section 2.4.4. With the addition of an OEF, the impact of the OEF on fix candidates and on the position estimate error must be revisited.

First, in order to derive the NFF, the noise free impact of the fault on state estimate can be computed by simply propagating the fault impact on state estimates

through the bootstrap fixing procedure. We initialize equation 5.10 below with  $\mathbf{b}_0 = \mathbf{Sf}$ , so that at the  $k^{\text{th}}$  iteration of the bootstrap fixing process we have,

$$\mathbf{b}_k = \mathbf{b}_{k-1} + \mathbf{K}_k(\langle \mathbf{H}_k \mathbf{b}_{k-1} \rangle - \mathbf{H}_k \mathbf{b}_{k-1}) \quad (5.10)$$

$$\text{where : } \mathbf{H}_k = \begin{bmatrix} \mathbf{0} & \mathbf{Z}_{:,k}^T \end{bmatrix} \in \mathbb{R}^{1 \times m}$$

$$\mathbf{K}_k = \mathbf{P}_{k-1} \mathbf{H}_k^T (\mathbf{H}_k \mathbf{P}_{k-1} \mathbf{H}_k^T)^{-1} \in \mathbb{R}^{m \times 1}$$

$$\mathbf{P}_k = \mathbf{P}_{k-1} - \mathbf{K}_k (\mathbf{H}_k \mathbf{P}_{k-1} \mathbf{H}_k^T) \mathbf{K}_k^T \in \mathbb{R}^{m \times m}$$

After fixing  $k$  cycle ambiguities, the position bias induced only by the fault (i.e. in the absence of noise) is given by the first three elements of  $\mathbf{b}_k$ .

In addition, the position estimate error must be evaluated given a candidate fix vector  $\boldsymbol{\eta}$ . Equation 2.35 was based on the ‘correct’ fix. The corresponding equation in the presence of a fault is,

$$\mathbf{p}_k = \mathbf{K}_{kk(1:3,:)} (\boldsymbol{\eta}_{NFF} - \boldsymbol{\eta}) \in \mathbb{R}^{3 \times 1} \quad (5.11)$$

where,

$\mathbf{p}_k$  : bias on state estimate vector given candidate vector  $\boldsymbol{\eta}$ , for  $k$  fixed integers

$\boldsymbol{\eta}_{NFF}$  : noise free fix vector

$\boldsymbol{\eta}$  : candidate fix vector

It is worth noting that  $\boldsymbol{\eta}_{NFF}$  and  $\boldsymbol{\eta}$  do not need to be individually computed. Instead, the term  $(\boldsymbol{\eta}_{NFF} - \boldsymbol{\eta})$  is computed as a candidate vector  $\mathbf{c}$ . This is covered in Appendix F.

So, using equations 5.10 and 5.11 the bias  $\mathbf{b}(\mathbf{f}, \boldsymbol{\eta})$  on the position domain in the absence of measurement noise is written as,

$$\mathbf{b}(\mathbf{f}, \boldsymbol{\eta}) := \mathbf{b}_{k(1:3)} + \mathbf{p}_k \quad (5.12)$$

This is the mean of the estimate error in the absence of measurement noise after  $k$  fixes, given a fault vector  $\mathbf{f}$  and candidate fix  $\boldsymbol{\eta}$ . The state estimate error distribution can be written as,

$$\delta\check{\mathbf{x}}_x \sim N(\mathbf{b}_x(\mathbf{f}, \boldsymbol{\eta}), \sigma_x^2) \quad (5.13)$$

where,

$\delta\check{\mathbf{x}}_x$  : position error corresponding to state  $x$

$\mathbf{b}_x(\mathbf{f}, \boldsymbol{\eta})$  : position domain bias corresponding to state  $x$  (in absence of measurement noise)

$\sigma_x$  : standard deviation of position error for state  $x$

It is worth noticing that, the fault and fix candidates only influence the mean of the distribution.

#### 5.4 Evaluation of the EPIC-Light URAIM Integrity Risk Bound

To establish a bound on the integrity risk using URAIM with EPIC light, we need to compute  $P(HI | F, \boldsymbol{\eta})$ ,  $P(ND | F)$ , and  $P(\check{\mathbf{n}} = \boldsymbol{\eta} | F)$  shown in equation 5.7. The probability of no detection,  $P(ND | F)$ , is computed using the float residual defined in equation 4.2. We also know from Chapter 4 that the test statistic is non-centrally chi square distributed with  $n - m$  degrees of freedom and NCP given in equation 4.4. Also, the threshold,  $R_c$ , is set to meet a continuity requirement. Both the test statistic  $q$  and threshold  $R_c$  are independent of integer fixes.

The probability of hazardous information  $P(HI | F, \boldsymbol{\eta})$  may be computed knowing the distribution of the position state estimates given in equation 5.13. However, unlike  $P(ND | F)$ , this probability must be evaluated for each cycle ambiguity fix candidate  $\boldsymbol{\eta} \in C$ .

Finally, we consider the probability of fix occurrence  $P(\check{\mathbf{n}} = \boldsymbol{\eta} | F)$ . Equation 2.34 describes the probability mass function in absence of fault. A similar ex-

pression may be written for the faulted scenario as,

$$P(\check{\mathbf{n}} = \boldsymbol{\eta} | F) = \prod_{j=1}^k \left[ \Phi \left( \frac{1 - 2\xi}{2\sigma_{j|J}} \right) + \Phi \left( \frac{1 + 2\xi}{2\sigma_{j|J}} \right) - 1 \right] \quad (5.14)$$

where :  $\Phi(x) = \int_{-\infty}^x \frac{1}{\sqrt{2\pi}} e^{-1/2v^2} dv$

In equation 2.34, vector  $\boldsymbol{\zeta}$  captured the candidate fix we wished to evaluate the probability for. In the presence of an OEF, the shift in the distribution induced by the fault must also be captured. In equation 5.14,  $\xi$  is used to represent both of these shifts.

To account for the shift caused by the presence of an OEF given a candidate fix  $\boldsymbol{\eta}$ , we use what we call the “innovation” term,  $(\langle \mathbf{H}_k \mathbf{b}_{k-1} \rangle - \mathbf{H}_k \mathbf{b}_{k-1})$ . Then, the effect of the fix candidate is taken into account in a similar fashion to the fault free case, except that the candidate offset from the NFF is desired (rather than correct fix) because the region is centered about the NFF. The definition for  $\xi$  in equation 5.14 is shown below and numerically verified in [JKSP11].

$$\xi := (\langle \mathbf{H}_k \mathbf{b}_{k-1} \rangle - \mathbf{H}_k \mathbf{b}_{k-1}) + \mathbf{I}_j^T (\boldsymbol{\eta}_{NFF} - \boldsymbol{\eta})$$

Once again, the vector term  $(\boldsymbol{\eta}_{NFF} - \boldsymbol{\eta})$  appears. Appendix F describes how to compute this term.

## 5.5 EPIC-URAIM Integrity Risk Evaluation For All Possible Faults

The goal of URAIM is to protect against all possible orbit ephemeris faults. This means that our simulation must account for ephemeris faults of any magnitude on any satellite. Or, it must account for the worst-case fault, which maximizes the integrity risk. The OEF fault model discussed in Section 3.4.4 is now applied to the EPIC-URAIM integrity risk bounding procedure.

Substituting equation 5.7 for the  $P(HMI | {}^i\mathbf{f}_1)$  term in equation 3.47 we can

write the integrity risk bound as,

$$P(HMI | F)P(F) \leq P(\mathbf{f}_1) \sum_{i=1}^n \max_{\forall \|\mathbf{f}_1\| \in \mathbb{R}^+} \left\{ P(ND | \mathbf{f}_1) \left( \sum_{\boldsymbol{\eta} \in C} P(HI | \mathbf{f}_1, \boldsymbol{\eta}) P(\check{\mathbf{n}} = \boldsymbol{\eta} | \mathbf{f}_1) \right. \right. \\ \left. \left. + 1 - \sum_{\boldsymbol{\eta} \in C} P(\check{\mathbf{n}} = \boldsymbol{\eta} | \mathbf{f}_1) \right) \right\} + P(\mathbf{f}_{\geq 2}) \quad (5.15)$$

From equation 5.15, we see that  $P(ND | \mathbf{f}_1)$ ,  $P(HI | \mathbf{f}_1, \boldsymbol{\eta})$ , and  $P(\check{\mathbf{n}} = \boldsymbol{\eta} | \mathbf{f}_1)$  will depend on fault mode and magnitude. There are a finite number of possible fault modes, but accounting for all possible fault magnitudes is much more difficult.

The right-hand-side of equation 5.15 bounds the true integrity risk, and is compared to a requirement to assess the availability of integrity for the system. To satisfy an integrity risk requirement  $I_{F,req.}$  for a given application, the following must be true.

$$I_{F,req.} \geq P(\mathbf{f}_1) \sum_{i=1}^n \max_{\forall \|\mathbf{f}_1\| \in \mathbb{R}^+} \left\{ P(ND | \mathbf{f}_1) \left( \sum_{\boldsymbol{\eta} \in C} P(HI | \mathbf{f}_1, \boldsymbol{\eta}) P(\check{\mathbf{n}} = \boldsymbol{\eta} | \mathbf{f}_1) \right. \right. \\ \left. \left. + 1 - \sum_{\boldsymbol{\eta} \in C} P(\check{\mathbf{n}} = \boldsymbol{\eta} | \mathbf{f}_1) \right) \right\} + P(\mathbf{f}_{\geq 2}) \quad (5.16)$$

From equation 5.16 we see that it is only necessary to increase fault magnitude until  $P(ND | \mathbf{f}_1)$  drops below the integrity risk requirement. All larger faults are guaranteed to be detected with integrity. Adding this constraint to equation 5.16 we obtain,

$$I_{F,req.} \geq P(\mathbf{f}_1) \sum_{i=1}^n \max_{\forall \|\mathbf{f}_1\| \in \mathbb{R}^+} \left\{ P(ND | \mathbf{f}_1) \left( \sum_{\boldsymbol{\eta} \in C} P(HI | \mathbf{f}_1, \boldsymbol{\eta}) P(\check{\mathbf{n}} = \boldsymbol{\eta} | \mathbf{f}_1) \right. \right. \\ \left. \left. + 1 - \sum_{\boldsymbol{\eta} \in C} P(\check{\mathbf{n}} = \boldsymbol{\eta} | \mathbf{f}_1) \right) \right\} + P(\mathbf{f}_{\geq 2}) \\ \text{where: } P(ND | \mathbf{f}_1, \|\mathbf{f}_1\| = j) < (I_{F,req.} - P(\mathbf{f}_{\geq 2})) / (nP(\mathbf{f}_1)) \quad (5.17)$$

Equation 5.17 is the final expression used to evaluate the integrity availability of the EPIC-URAIM algorithm.

## 5.6 EPIC-URAIM Fixing Criterion

The criterion to stop the bootstrap fixing process for EPIC-RAIM is based on integrity. Three possible algorithms are proposed. The first is illustrated in figure 5.1, where integers are fixed until integrity requirements are met. The fault-free ( $\bar{F}$ ) and EPIC-URAIM (faulted) integrity risk bounds are computed after the float solution is obtained. If the bounds satisfy the integrity risk requirements, the float solution is used. If this is not the case, then we fix an additional ambiguity, compute new bounds on integrity risk, and check requirements again. This integer fixing process is repeated until requirements are satisfied, or until all cycle ambiguities are fixed. Afterwards, availability of accuracy may be computed.

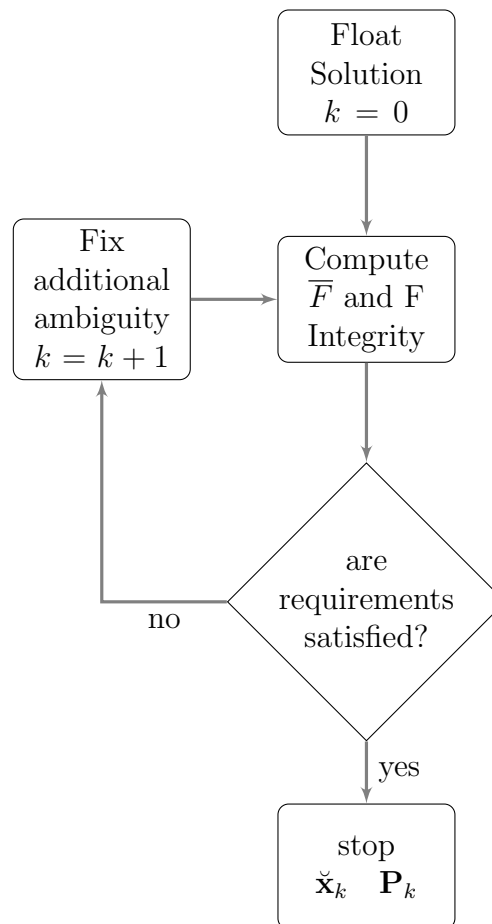


Figure 5.1. Overview of EPIC-URAIM Fixing Criterion 1

Anticipating poor accuracy performance using the first fixing criterion, an

alternative is to fix integers until the minimum integrity risk is obtained. Accuracy performance will improve as more cycle ambiguities are fixed. Figure 5.2, illustrates this algorithm. The float and first cycle ambiguity fix are computed. Fault free and EPIC-URAIM integrity risk bounds are computed for both  $k = 0$  (float) and  $k = 1$  (first ambiguity fix). If the bounds for  $k = 1$  are greater than those for  $k = 0$ , and  $k = 0$  satisfies the requirements, the float solution is the output. If this is not the case, then the current bounds are temporarily stored, and another integer is fixed,  $k = k + 1$ . Again, new bounds are computed and compared to the previous. This is repeated until the current bounds exceed the previous (while the previous satisfy requirements). This is taken to be the minimum because once the integrity risk bound begins growing, it is unlikely that it will decrease again.

To improve upon accuracy even more, the third criterion aims at fixing as many integers as possible without exceeding the integrity risk requirements. Figure 5.3 shows this process, which is similar to the previous criterion because it involves storing the previous bound. In this algorithm, two successive bounds are compared directly to the requirements rather than to one another. If the previous bound satisfies requirements and the current one exceeds requirements, the previous solution is the output of the algorithm. This solution corresponds to the maximum number of fixed cycle ambiguities before the integrity risk requirement is exceeded.

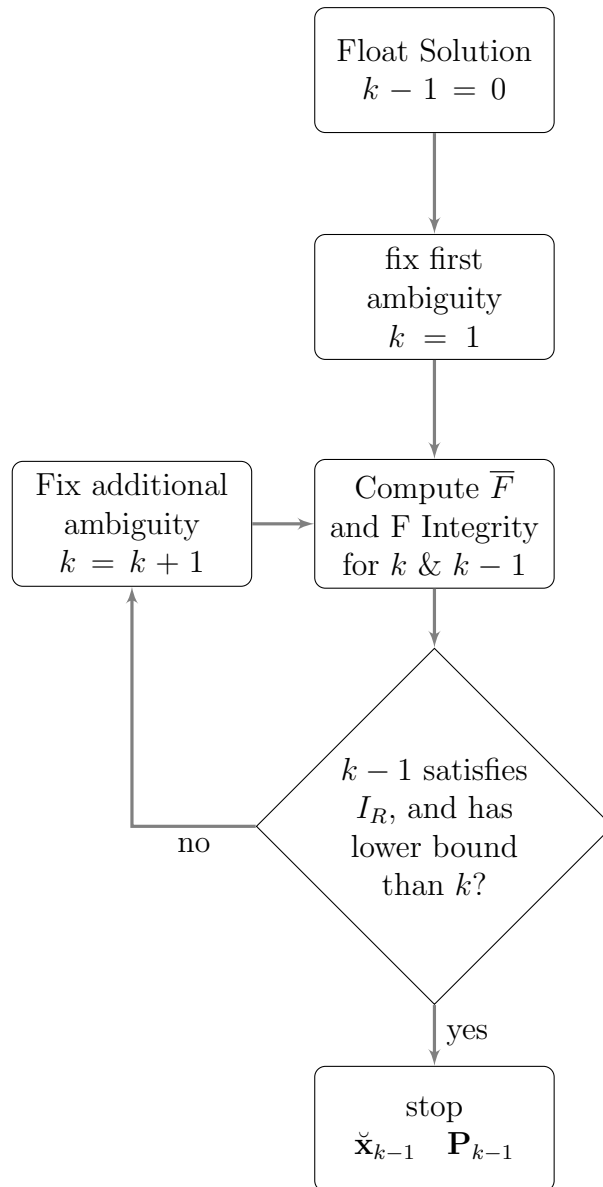


Figure 5.2. EPIC-URAIM Fixing Criterion 2: Minimizing Integrity Risk Bound

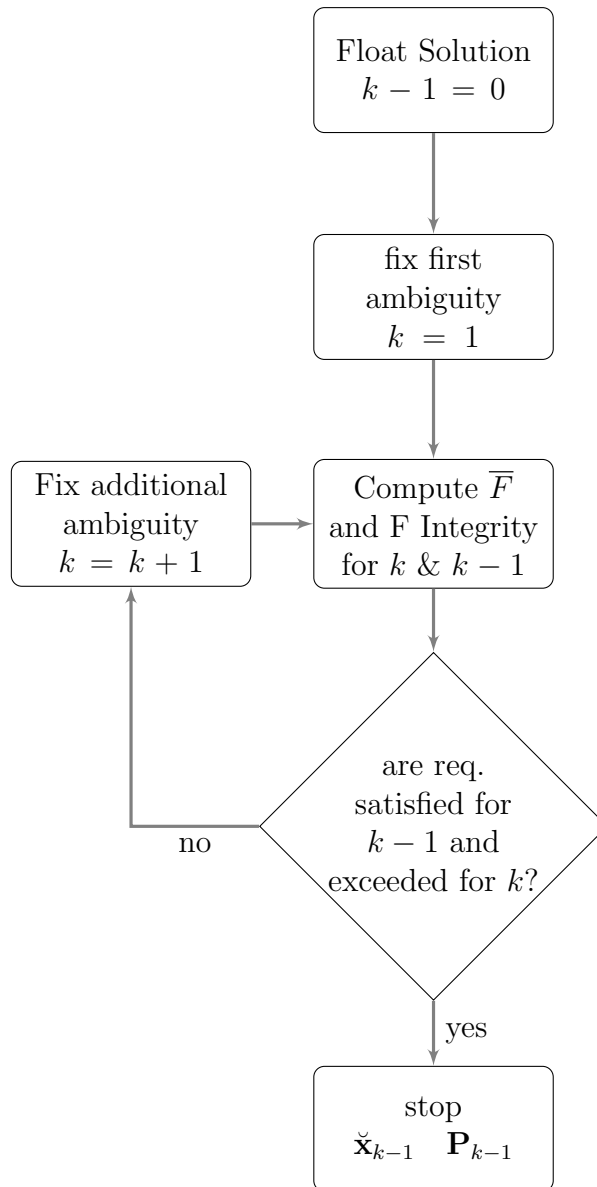


Figure 5.3. EPIC-URAIM Fixing Criterion 3: Maximum Number of Integer Fixes

## CHAPTER 6

### AVAILABILITY PERFORMANCE ANALYSIS

The focus of this chapter is on quantifying the performance and assessing implementation feasibility of the URAIM orbit ephemeris fault detection algorithm introduced in Section 4.3. The benchmark application used in the analysis is introduced and necessary simulation parameters are defined. Initially, the float solution results for URAIM and DRAIM are shown for comparison. In addition, the effect of fixing integers on algorithm performance is investigated. The impact of fault mode and magnitude as well as the number of EPIC fix candidates is discussed. Finally, the global-sea-coverage results using the new URAIM algorithm are shown.

#### **6.1 Framework For JPALS Benchmark Application**

The Joint Precision Approach and Landing System (JPALS) is used as the benchmark application for this work. The particular aircraft approach we consider involves landing military aircraft on a naval carrier ship. This type of mission is more difficult to carry out than land based precision approach because the ship is in constant motion. So, this is truly a rendezvous application. We are not focusing on the specific absolute location of the carrier ship, nor of the aircraft. The main concern for this approach is the relative positioning of the aircraft with respect to the carrier ship.

There are multiple ‘case’ approaches that the aircraft may use. In this work, the focus is on the case III approach, which is a straight in trajectory with a 3 degree glide slope angle. The speed of a typical aircraft during the approach is roughly 150 nmi/hr [HP04]. Note that the ephemeris fault for straight in approach was introduced in Section 3.4.3.

Example alert limit ( $\ell$ ) and continuity requirements for the JPALS benchmark application are listed in Table 6.1. The alert limits are given in the vertical and horizontal directions, and indicate the maximum allowable positioning errors. By definition, hazardous information (HI) is present if the error exceeds the alert limit. The emphasis of this work is placed on meeting integrity requirements. Therefore, accuracy requirements are not listed here.

Table 6.1. Example (JPALS) System Requirements

Requirement	Value
Vertical Alert Limit (VAL)	1.8 m
Lateral Alert Limit (LAL)	1.8 m
Continuity	$8 \times 10^{-6}$
Prior OEF probability, $P({}^i\mathbf{f}_1)$	$1 \times 10^{-5}$

An example integrity risk allocation tree for the JPALS application is shown in Figure 6.1 [Lag07]. Notice that the total allowable integrity risk probability of  $1 \times 10^{-6}$  is divided or allocated amongst the various fault hypotheses. The risk is divided between the fault free and faulted cases. Then, the orbit ephemeris fault is given an allowable integrity risk of  $1 \times 10^{-7}$ . This leaves a probability of  $3 \times 10^{-7}$  for other satellite faults, receiver faults and atmospheric anomalies.

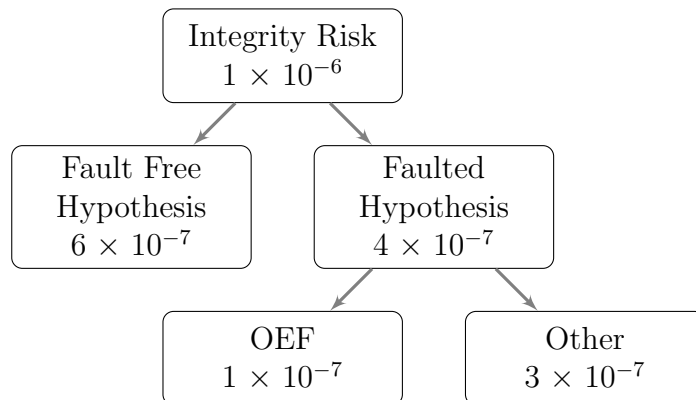


Figure 6.1. Example Integrity Allocation Tree

Differential GPS may be used once the aircraft enters the broadcast radius (also called the service volume). In this work, the service volume is considered to be within 15 nmi from touchdown (TD). Given the aircraft speed of 150 nmi/hr, the aircraft will reach the ship in roughly 6 minutes.

URAIM performance for this example application is first observed at a single location on the earth:  $35^\circ$  N latitude and  $-150^\circ$  E longitude. This particular point is chosen because it yields among the worst float results globally. This example location will also be used in the investigation of the effect of fixing cycle ambiguities on algorithm performance.

## 6.2 Float URAIM Results

The float implementation of the URAIM concept is introduced was Section 4.3. Since URAIM incorporates both RRAIM and DRAIM, its performance is expected to exceed that of float DRAIM as the aircraft nears touchdown. At the start of an approach, the performance of URAIM is expected to be comparable to that of DRAIM since the synthetic baseline is short and carrier measurements at the initial epoch will not provide added observability on the fault.

The float simulation parameters are presented in Table 6.2. Aircraft approaches are simulated at 2 minute increments for a 24 hour period. The aircraft begins each approach at 15 nmi from touchdown, and each 0.5 nmi increment during the approach is simulated. This work uses a nominal satellite constellation with 24 SVs [oD08]. Figure 6.2 shows the float URAIM and DRAIM results using GF and WL carrier measurements. Final availability is computed for each point within the aircraft approach.

From the results in Figure 6.2 we see that URAIM and DRAIM performance quantified in terms of availability is very similar from roughly 15 - 5 nmi from touch-

Table 6.2. Float Simulation Parameters

Parameter	Value
Location	35° N –150° E
Elevation Mask	7 deg.
SD Carrier sigma	0.01 m
SD Code sigma	0.5 m
# of ship antenna	2
Vertical iono gradient, $\sigma_{Ivg}$	4 mm/km
Initial nominal tropo refractivity, $\sigma_N$	10
Air MP time constant, $1/\beta_a$	20 s
Ship MP time constant, $1/\beta_s$	60 s

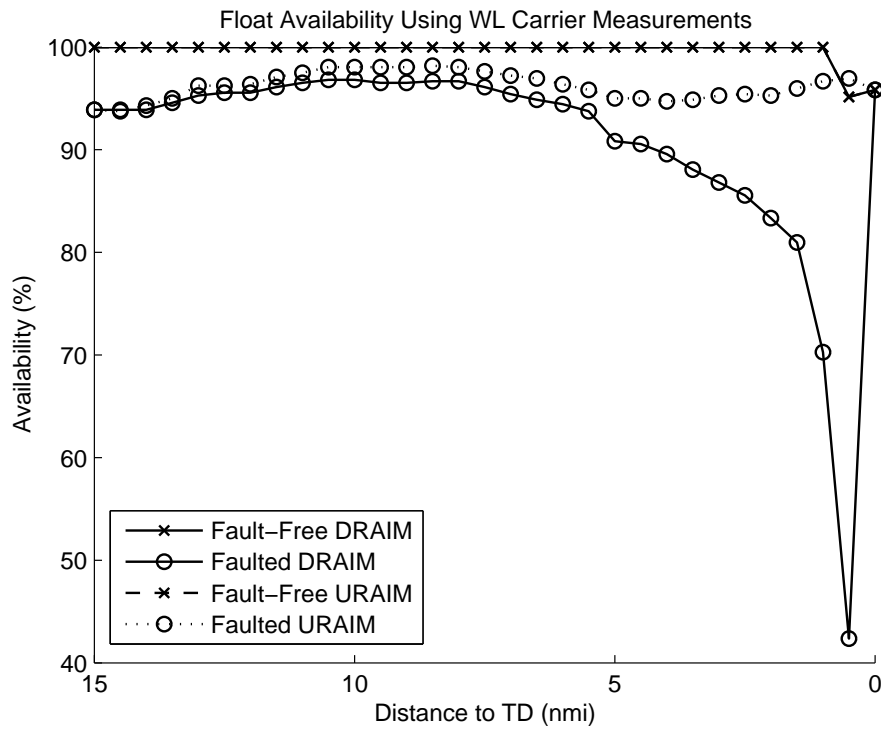


Figure 6.2. Comparison of DRAIM and URAIM float availability performance

down. Within 5 nmi of touchdown, DRAIM availability falls below 40 percent due to the short relative baseline between aircraft and ship. On the other hand, URAIM

availability does not decrease because the addition of initial epoch carrier measurements provides a much longer “synthetic” baseline which improves OEF detection capability.

Although the integrity availability of URAIM is above 90 % for the duration of the approach, the float solution does not simultaneously provide adequate accuracy availability. Simultaneously providing high integrity and high accuracy requires fixing cycle ambiguities. Fixing integers will improve accuracy and possibly integrity as well, because reducing standard deviation on position states will reduce  $P(HMI)$ . It is critical to bound the true integrity risk as “tightly” as possible, which is why the EPIC-light integrity risk bounding method is used with URAIM.

### 6.3 Understanding EPIC-URAIM

When cycle ambiguities are fixed, the EPIC-light integrity risk bounding method discussed in Chapter 5 is used with the URAIM measurement equation 4.30. The following examples are used to help illustrate the computations involved in the URAIM algorithm using EPIC light. Dual ship antenna and WL measurements are used in the simulation.

For these examples we look at the same sample location used in the float example ( $35^\circ$  N latitude and  $-150^\circ$  E longitude). However, instead of simulating approaches over a 24 hour period, a single SV geometry is considered with 5 visible satellites. Also, we look at a single ‘snapshot’ point during the approach. The most crucial part of an approach is seconds before touchdown. In this work, 0.5 nmi from touchdown is chosen to represent a point within this critical region. Unless otherwise stated, the remaining results analysis will focus on system performance at this distance from touchdown.

**6.3.1 Impact of Fault Magnitude.** The impact of fault magnitude on the

bound on integrity risk using the EPIC-light method is observed for all fault modes (defined in Section 3.4.3) and then narrowed down to a single mode for which the constituent probabilities are investigated. In addition, we look at two extreme fixing cases (one fixed and all fixed integers). The fault magnitude is increased until the probability of no detection  $P(ND|F)$  is less than the integrity risk requirement. Beyond that point, the fault will be detected with integrity and the user is safe.

In this example there are 5 visible SVs, and therefore 5 single SV fault modes. Since, this example uses dual reference antennas, there are 8 double differenced cycle ambiguities. Figure 6.3 shows the impact of fault magnitude on the bound on probability of HMI for each fault mode when 1 out of 8 double differenced integer ambiguities is fixed. The fault magnitude is computed as the norm of the fault vector. As shown in Figure 6.3, the probability of hazardous misleading information varies as a function of both fault mode and magnitude. Recall that the maximum probability of HMI for each mode is used in computing the final bound on integrity risk. We will consider mode 5 for the remainder of the fault magnitude discussion.

Figure 6.4(a) shows the impact of fault magnitude on the bound on probability of HMI. (Note that the bound on  $P(HMI)$  is plotted on a linear scale in Figure 6.4(a) and log scale in Figure 6.3.) Figure 6.4(b) shows the impact of fault magnitude on the constituent probabilities used to compute the bound in Figure 6.4(a). In this case 1 out of 8 double difference integer ambiguities is fixed and only a single fault mode is observed.

In Figure 6.4(b) this example has a consistently high probability of fixing to within the candidate region, i.e.  $\sum_{\boldsymbol{\eta} \in C} P(\check{\mathbf{n}} = \boldsymbol{\eta} | F) \cong 1$  in equation 5.7. This is vital to keeping a tight bound on the integrity risk. The probability of HMI is therefore dominated by the product of probability of no detection and hazardous information,  $P(ND|F) \sum_{\boldsymbol{\eta} \in C} P(HI|F, \boldsymbol{\eta}) P(\check{\mathbf{n}} = \boldsymbol{\eta} | F)$  where  $P(\check{\mathbf{n}} = \boldsymbol{\eta} | F) \cong 1$ . For small fault

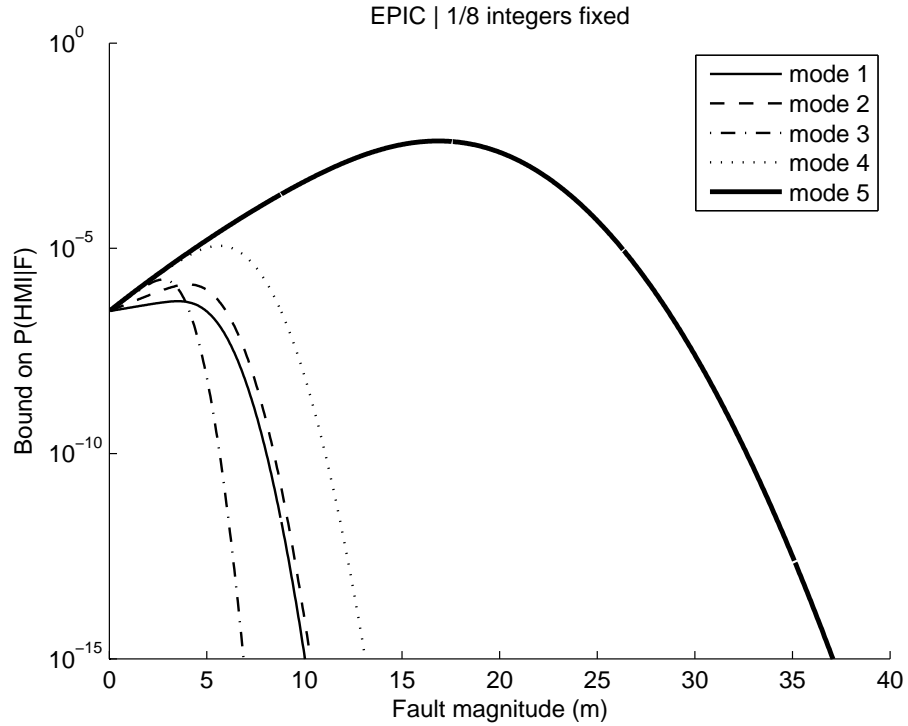
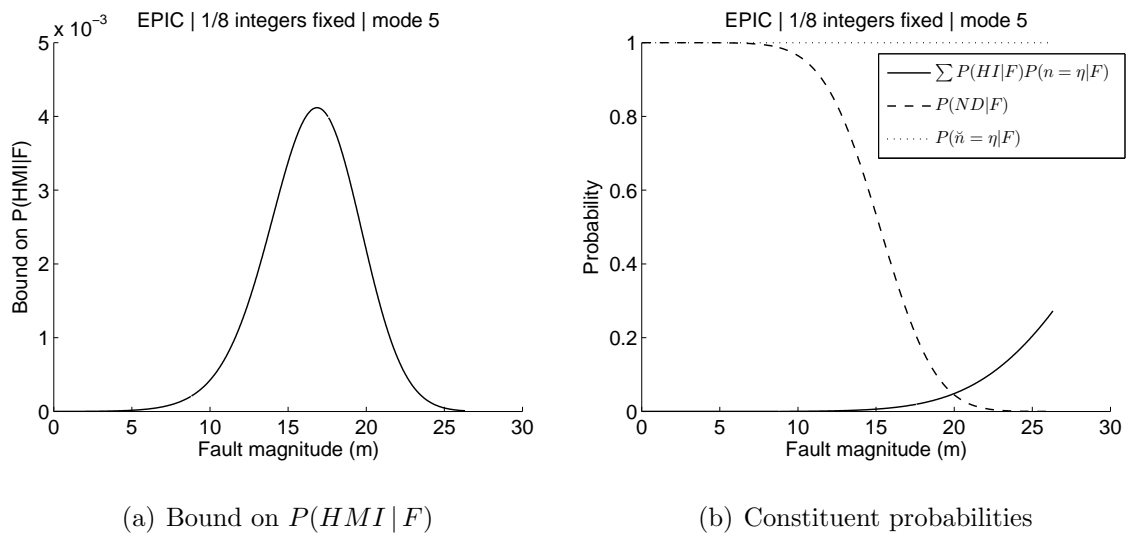


Figure 6.3. Bound on  $P(HMI | F)$  for all fault modes



(a) Bound on  $P(HMI | F)$

(b) Constituent probabilities

Figure 6.4. EPIC with 1/8 fixed integers

magnitudes, the probability of no detection is high and probability of hazardous information is low. As the fault magnitude increases, the probability of no detection decreases as the probability of HI increases. The peak in the bound on probability of

HMI happens during this transition.

Now, we move to the other extreme with all 8 integers fixed. Figure 6.5 shows the bound on probability of HMI and its constituent probabilities for the case of all fixed integers. The plots in Figure 6.5 are similar to those in Figure 6.4. The probability of no detection is the same in both cases, because this probability is derived from the float residual and is unaffected by integer fixes. The probability of fixing to within the candidate region remains very close to one. Notice that the probability of HI remains very low and only begins to increase noticeably for fault magnitudes greater than 20 m. At this point,  $P(ND | F)$  is already very low, which results in a lower bound on probability of HMI as compared to the previous case with 1/8 fixed integers.

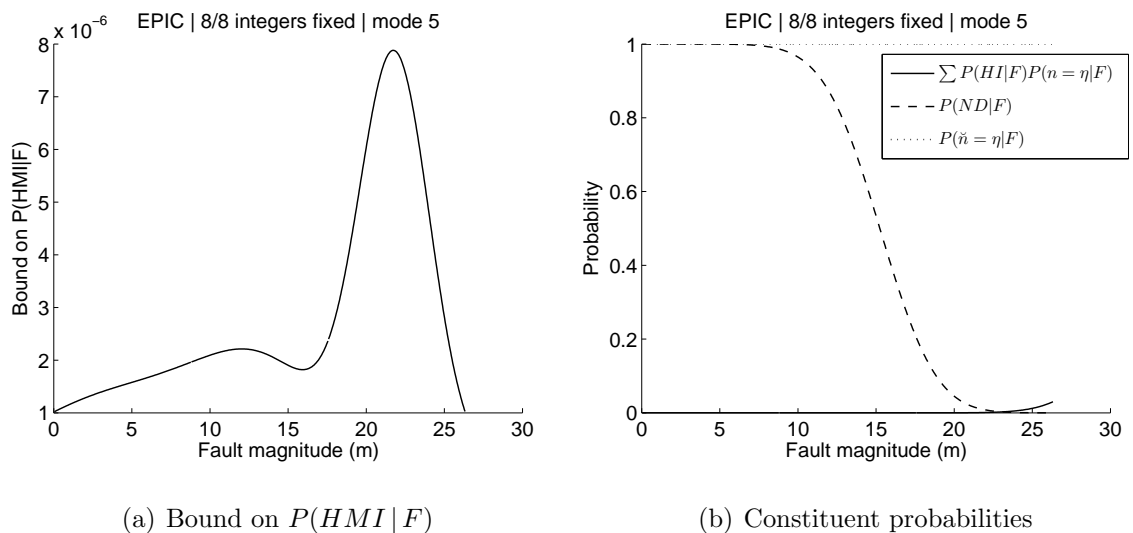


Figure 6.5. EPIC with 8/8 fixed integers

Since  $P(ND | F)$  is derived from the float residual, it is unaffected by fixing integers. To keep a tight the bound on the probability of HMI, we must ensure that the probability of fixing to the candidate region remains close to one. Increasing the number of candidates will aid in keeping the probability of fixing to within the candidate region high at the cost of additional computation. It will also help decrease

the probability of HI, because of the assumption that  $P(HI | F)$  is one when outside the candidate space.

**6.3.2 Impact of Candidates.** In this section, the impact of the number of candidates on the computed bound on  $P(HMI | F)$  is investigated. To begin, we first look at the probability of fix occurrence for each candidate. Afterwards, we look at the number of fix candidates considered, and their effect on the probability of fixing to within the candidate region and on the overall integrity risk bound. Finally, the bound on integrity risk is broken up into its constituent probabilities as a function of the number of candidates.

Figure 6.6 shows the probability of fixing to different candidate integer vectors (which are numbered on the x-axis), given a specific fault magnitude. The first candidate is the noise free fix (NFF), and the other candidates are in no particular order. Notice that the NFF has the largest probability of all the candidates in the set. This is expected because in Section 5.2 the NFF is defined as an approximation of the most likely fix. In addition, the probability of fix fluctuates because the candidates are not sorted in any particular order. The mode curves in Figure 6.6 follow a similar trend. However, the probability is dependent on both the fault mode and magnitude.

Figure 6.7 shows the effect of adding additional candidates on the computed bound on vertical integrity risk. In addition, the probability of fixing to within the chosen set of candidates  $\sum_{\eta \in C} P(\check{\mathbf{n}} = \boldsymbol{\eta} | F)$  is plotted for each fault mode. As the number of candidates increases, so does the probability of fixing to within the candidate region. However, this probability is not the same for each mode. In addition, the same candidate that has a relatively large effect on one mode, may not necessarily have such a large influence on another mode. A good example of this is observing mode 3 in Figure 6.7. The addition of the 196th candidate results in the most significant increase in the probability of fixing to the candidate set. Yet,

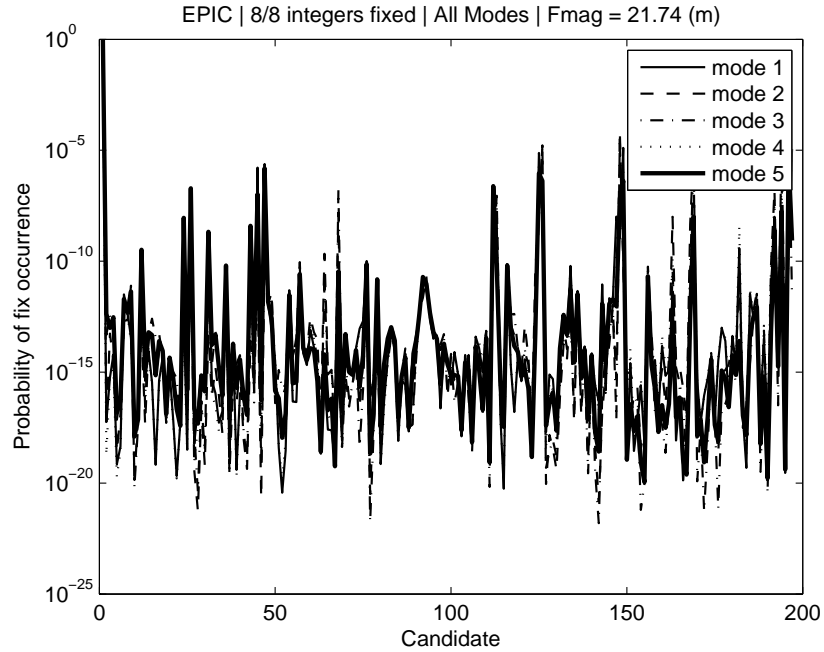


Figure 6.6. Probability of fix occurrence

the addition of this candidate is not as significant for the remaining modes. In this example (Figure 6.7), the probability of fixing to the candidate set is very close to unity regardless of the number of candidates.

The user and reference pre-filtering of geometry free measurements during the approach provide small cycle ambiguity state variance. This is the reason why the probability of fixing to the candidate region is not very sensitive to the addition of fix candidates. The effect of increasing the number of candidates would be much more pronounced for noisier measurements as illustrated in Figure 6.8. This figure shows that noisier measurements require more candidates for the probability curve to ‘stabilize’ at a particular value. In addition, a similar effect to increasing the measurement noise can occur if the approach distance of the benchmark JPALS application is shortened. The user (aircraft) filtering period would decrease and the estimate of cycle ambiguities would be noisier.

In addition, Figure 6.9 shows the  $P(HMI)$  (top) and ‘modified’  $P(HI)$  (bot-

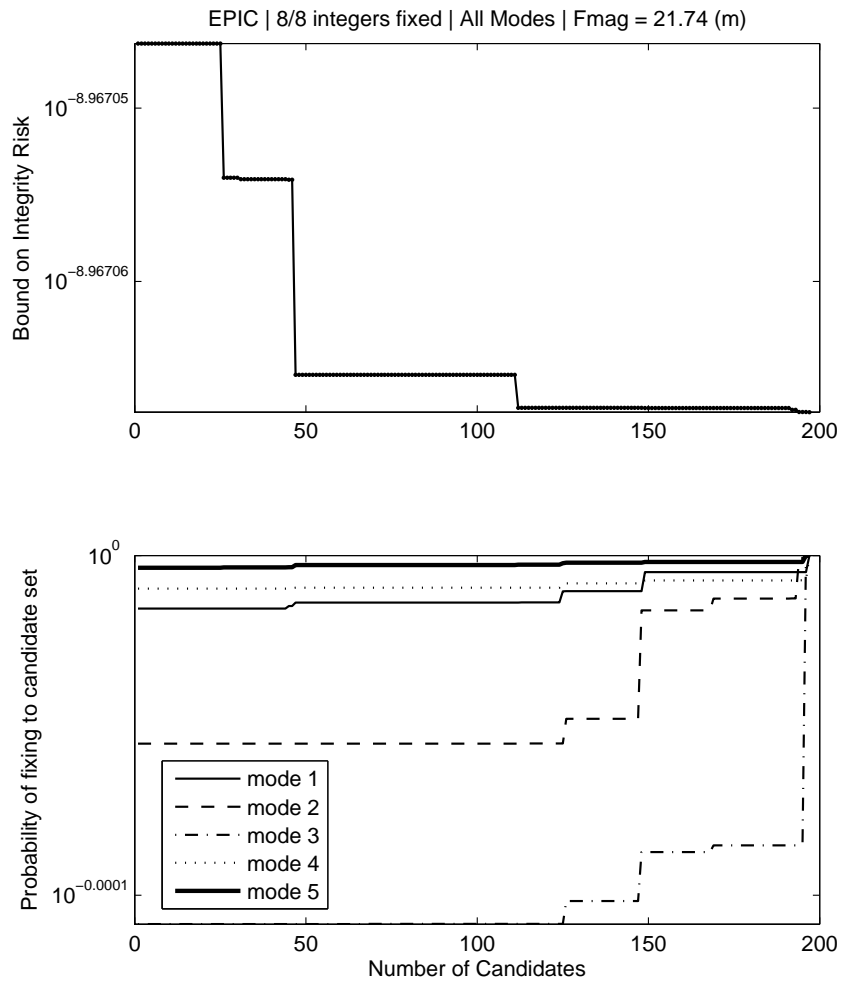


Figure 6.7. Integrity risk and probability of fixing to candidate set versus number of candidates

tom) used to generate the integrity risk bound plotted at the top of Figure 6.7. The modified  $P(HI)$  is defined as  $\sum_C P(HI | F, \boldsymbol{\eta}) P(\check{\mathbf{n}} = \boldsymbol{\eta} | F)$ . As expected, the modified probability of hazardous information grows as additional candidates are considered. This may seem to be a disadvantage of adding additional candidates, since this term increases the bound given in equation 5.7. However, because the probability of fixing to the candidate region grows faster than the modified probability of hazardous information, there is a net benefit to considering additional candidates. This is evident from the top plot in Figure 6.9 that shows  $P(HMI | F)$  for mode 5. Note that the remaining modes give probabilities less than  $10^{-50}$ , so they are not

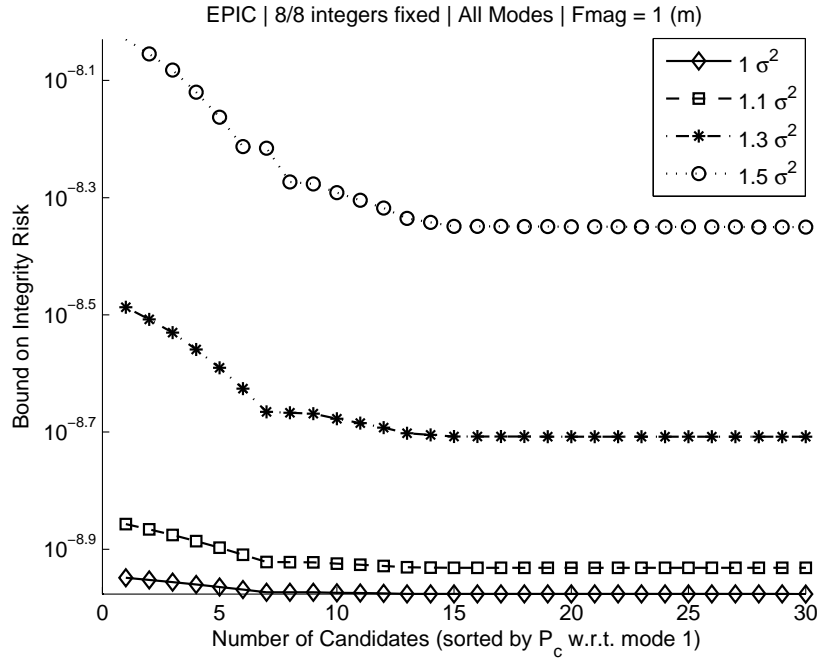


Figure 6.8. Inflated measurement noise effect on candidate set

visible/significant at the scale shown.

The candidate example shown in this section corresponds to a particular fault magnitude. For a different fault magnitude, the most effective candidates may vary. The search over fault mode and magnitude is unavoidable in the worst case approach to bounding integrity risk. And since very little can be said a priori regarding which candidates will prove useful in the search, there is no clear way to narrow down the candidate set to only include the most useful candidates.

### 6.3.3 Impact of Fixing.

Now that the component probabilities have been covered, we can look at the final integrity risk bound and how it is affected by fixing cycle ambiguities. Figure 6.10 shows the bound on integrity risk computed using EPIC-URAIM, as a function of integer fixes for both fault-free and faulted hypotheses. The integrity risk requirements (both fault-free and faulted) are given in Figure 6.1. The example is for dual ship antennas (5 SVs in view) and remaining simulation parameters are given in Table 6.2.

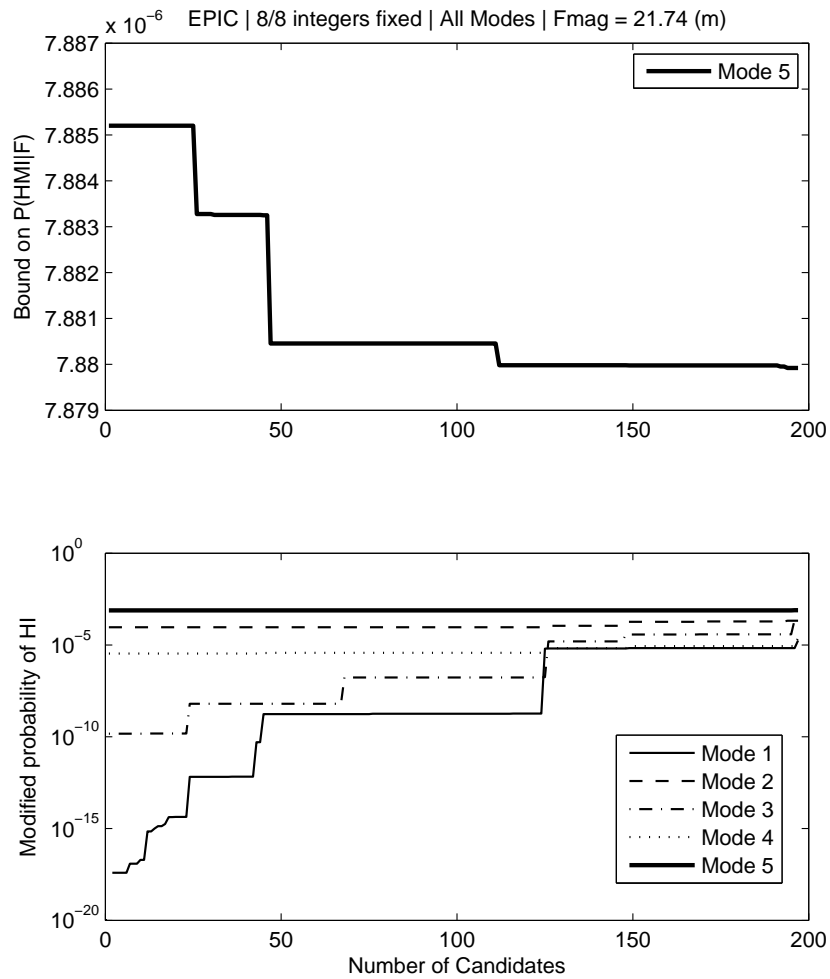


Figure 6.9. Bound on  $P(HMI | F)$  and modified probability of HI versus number of candidates

This example serves to illustrate the EPIC-URAIM algorithm for a single SV geometry. Assume we are looking to fix as many ambiguities as possible (to improve accuracy), while maintaining integrity. This algorithm is illustrated in Figure 5.3. We begin by computing the float case. From Figure 6.10 we see that the integrity risk bound for the faulted case exceeds the requirement. Therefore, we continue fixing integers. For the first six fixes, both the fault-free and faulted cases are available. For the seventh fix, the fault-free case is unavailable because the integrity risk exceeds the fault-free requirement. At this point, the algorithm is stopped and the solution with 6 fixed cycle ambiguities is used.

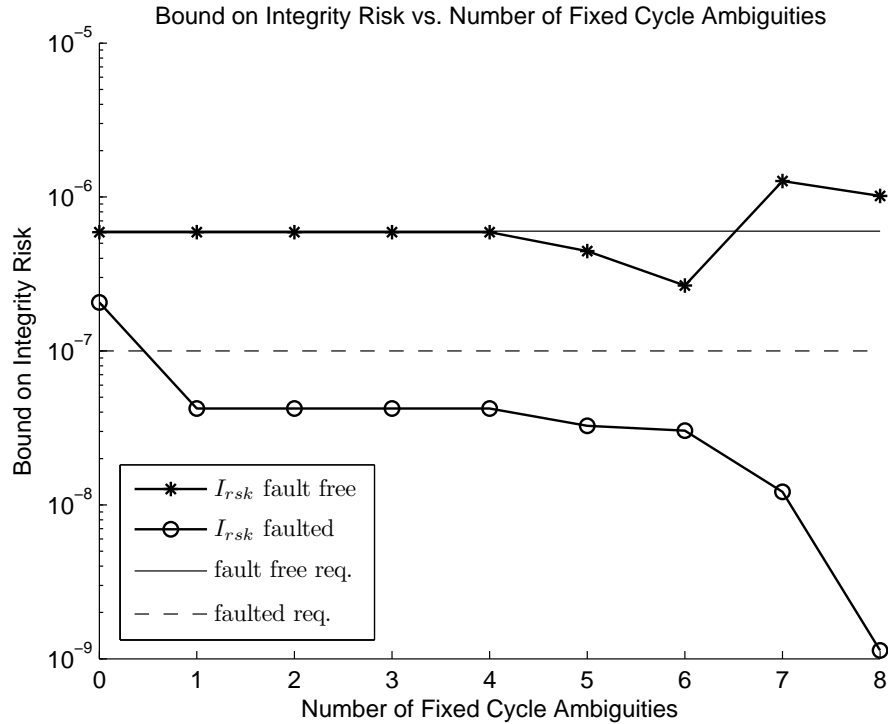


Figure 6.10. Impact of fixing integers on integrity risk

The results that follow are obtained by simply repeating this algorithm for numerous SV geometries at the same location. The algorithm shown in Figure 5.3 is used throughout the remainder of this work.

#### 6.4 EPIC-URAIM Single Location Results

The EPIC-URAIM algorithm is simulated over a 24 hour period for a hypothetical user located at  $35^\circ$  N latitude and  $-150^\circ$  E longitude. The EPIC specific simulation parameters are shown in Table 6.3. The remaining system parameters are in Table 6.2. The threshold for throwing out candidates is compared to the probability of occurrence for each fix candidate. And, if the probability of occurrence is less than the threshold, that candidate is eliminated from the simulation. Figure 6.11 shows the integrity risk, standard deviation of vertical and lateral positioning error, number of EPIC candidates, and number of fixed cycle ambiguities over the 24 hour

period.

Table 6.3. Single Location EPIC-URAIM Simulation Parameters

Parameter	Value
Candidate range	$\pm 2$ cycles
Threshold for throwing out candidates	$1 \times 10^{-12}$
Fixing criteria	Max fixes (Figure 5.3)

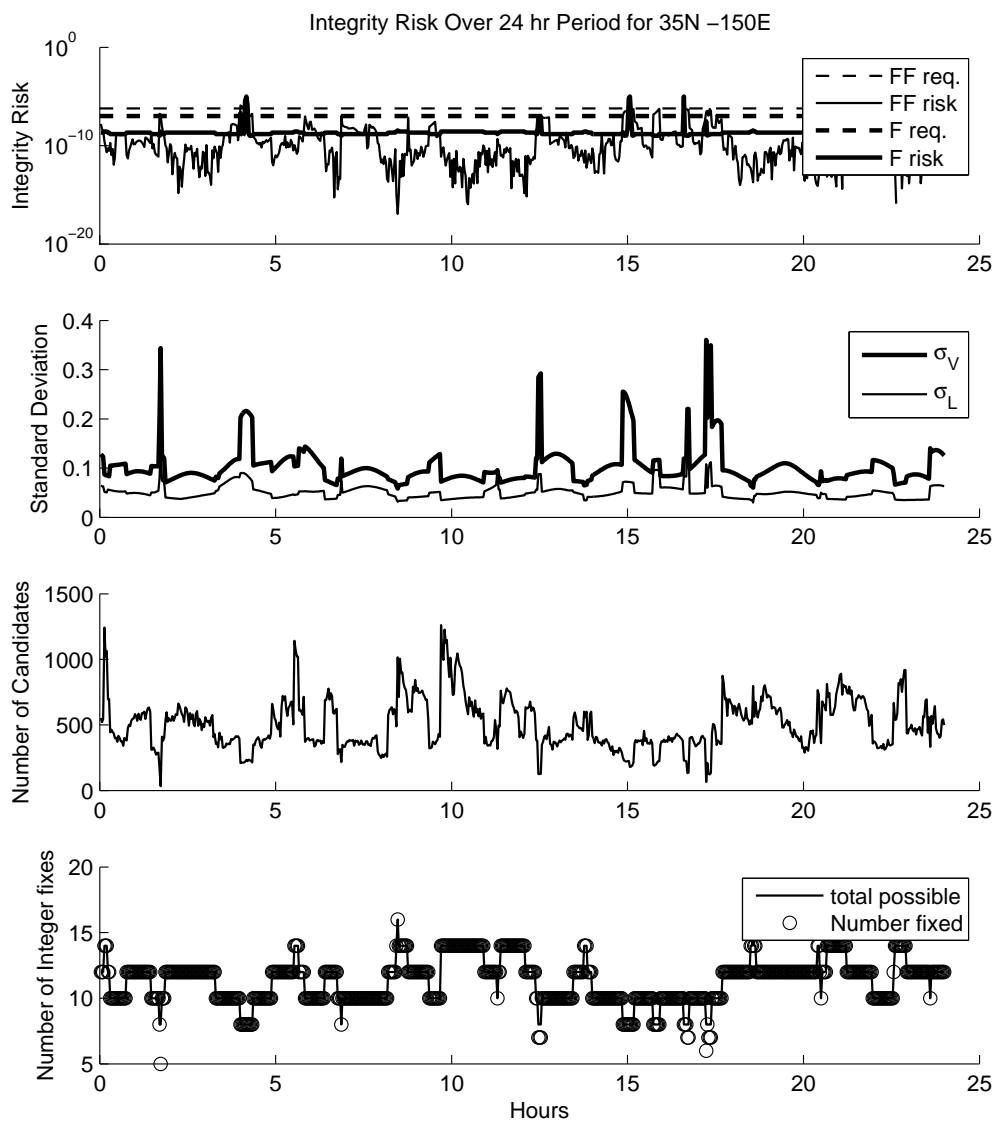


Figure 6.11. URAIM using EPIC-light results over 24 hr period

According to Figure 6.11, there are SV geometries during this 24 hour period that result in high integrity risk (at times: 2h, 4h, 12h, 15h, 16h, and 17h). We therefore cannot fix all cycle ambiguities (which results in relatively higher error standard deviations) and we have relatively fewer possible candidates to consider. There are several peaks in integrity risk that influence the overall system availability at this location. One interesting feature in Figure 6.11 is that the faulted integrity risk curve remains very flat between peaks. It does not fluctuate as much as the fault-free integrity risk. This behavior is explained because the integrity risk bound in equation 5.17 takes into account the prior probability of multiple simultaneous satellite faults as an added constant.

Due to the relatively large number of candidates used in generating the results for Figure 6.11, an attempt is made at reducing the required number of fix candidates. Figure 6.12 shows the same results as Figure 6.11, except that the threshold for eliminating candidates is increased to  $1 \times 10^{-3}$ . Comparing the two figures (note that there is a change of scale), we see that there is a difference in the computed integrity risk bound. Most notably, the fault-free curve fluctuates near the faulted curve, rather than below it. However, the overall system availability at this location is unaffected because no new integrity risk peaks appear. The benefit in terms of reduction in computation time is significant. In light of these results, the threshold for throwing out candidates is kept at  $1 \times 10^{-3}$  for the full sea-grid simulation.

Table 6.4 summarizes the EPIC-URAIM results at this location. The float and bootstrap results are also presented as a comparison to EPIC. The first column shows the combined availability including both fault-free and faulted cases. The second and third columns represent the fault-free and URAIM (faulted) availability respectively. The final column contains the average standard deviation of the vertical position state. Notice that EPIC outperforms bootstrap in combined availability. However, for

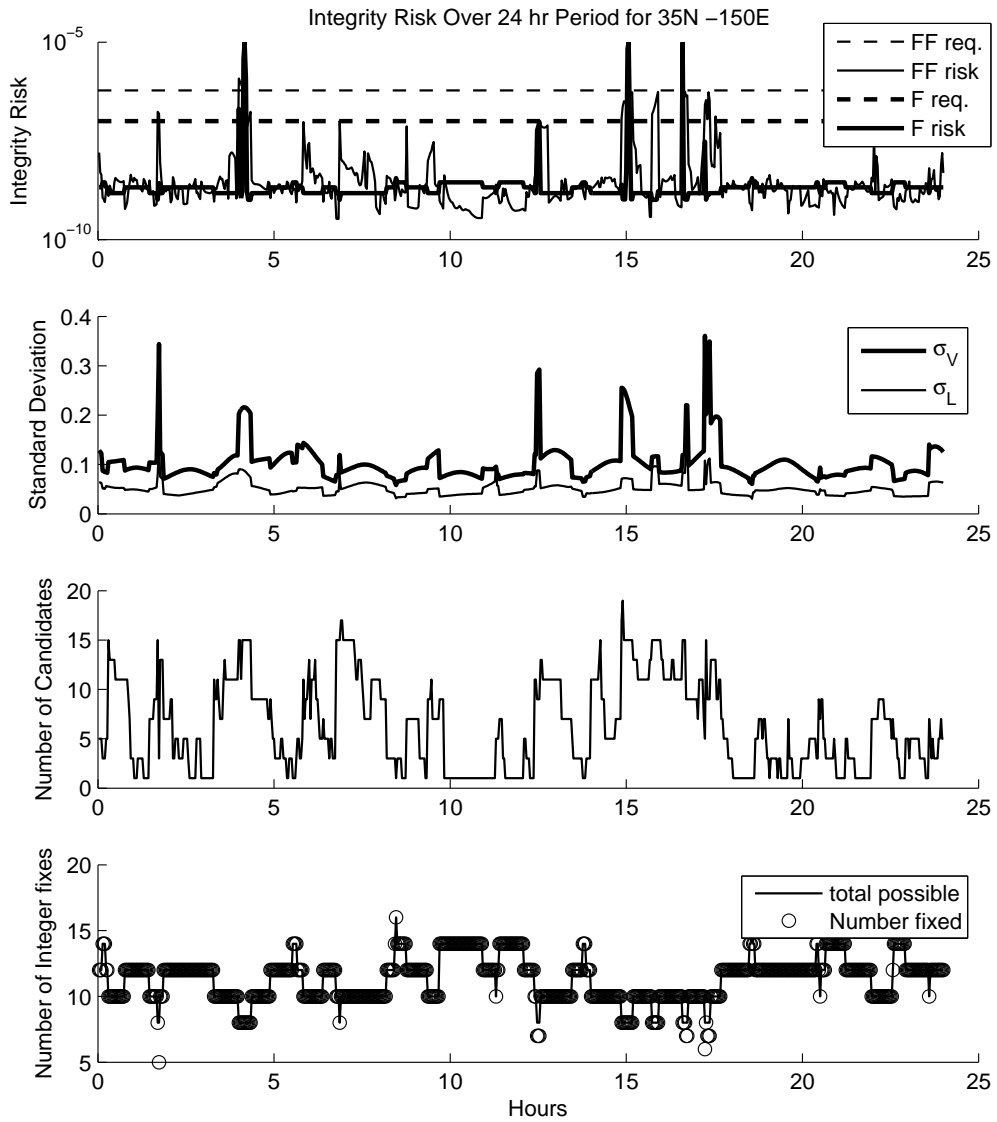


Figure 6.12. URAIM using EPIC-light results over 24 hr period using fewer candidates

the faulted scenario, they have the same availability.

Table 6.4. Avail. for Location 35N -150E; 0.5nm to TD

	Combined	H0	URAIM	avg. $\sigma_v$ (m)
Float	94.58	95.14	96.94	0.1881
Bootstrap	97.22	97.22	98.61	0.1054
EPIC	98.19	98.89	98.61	0.1027

## 6.5 Unified RAIM Results - EPIC light

In this section, the sea-grid simulation results for URAIM using EPIC-light are discussed. Aircraft approaches are simulated every 2 mins over a period of 24 hours, for 1507 sea-based locations around the globe. Figure 6.13 shows the sea-based locations on a world map. A single point during the approach (0.5 nmi from touchdown) is evaluated.

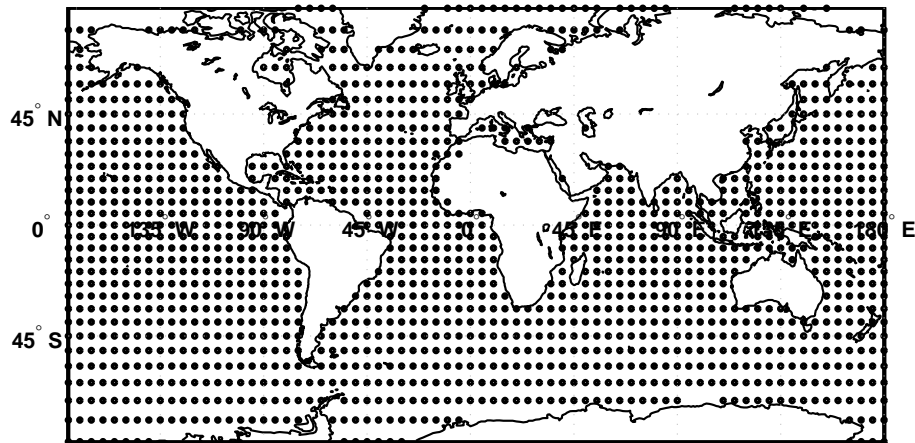


Figure 6.13. World map showing the simulation grid points

We begin with the integrity availability simulation, neglecting accuracy for the time being. The results for are plotted below in Figure 6.14. Average availability of EPIC-URAIM is shown to be 98.6%.

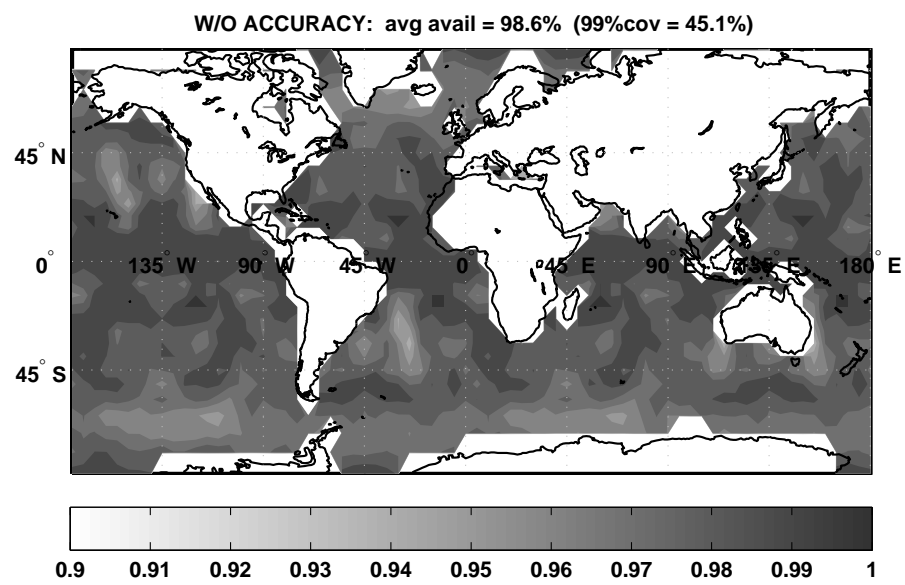


Figure 6.14. Integrity availability of sea based locations for JPALS

## CHAPTER 7

### CONCLUSION

In this work, we have established the theory behind orbit ephemeris fault detection for differential carrier phase GPS systems. These systems are used for applications requiring high accuracy as well as high integrity. The focus of this work has been on two residual-based Receiver Autonomous Integrity Monitoring (RAIM) methods, Relative RAIM (RRAIM) and Unified RAIM (URAIM).

#### **7.1 Measurement Error Models**

From the general viewpoint of integrity, it is important to model a system as completely and accurately as possible. This includes accounting for possible orbit ephemeris faults, as was the focus of this work. However, it is important to take into account measurement errors and their correlation as well.

This work focuses on the URAIM measurement equation. Existing models for ionospheric and tropospheric errors are used. However, the correlation of these models over time was derived. In addition, measurement noise correlations are derived. Closed-form expressions for the correlation between GF and (both current and past time) carrier measurements, assuming both discrete and continuous sampling, have been derived. In addition, the geometry free measurement noise variance is derived assuming discrete sampling. In this work, continuous sampling of measurements was assumed. However, it is now also possible to write the equations assuming discrete sampling.

#### **7.2 Unified RAIM**

The Unified RAIM (URAIM) concept was developed as a RAIM implementa-

tion that contains aspects of both Differential RAIM (DRAIM), and Relative RAIM (RRAIM). DRAIM was previously shown to be most effective upon entering the broadcast radius of the reference receiver. Its performance decreases when approaching the rendezvous point. The RRAIM concept was investigated as a means of improving DRAIM performance in close proximity of the rendezvous point (within 5nmi for the benchmark JPALS application). Unfortunately, it was shown that the RRAIM measurement equation cannot easily be used for detection because the residual is correlated with the state estimate error.

Unified RAIM was introduced as an alternative implementation to RRAIM. It integrates aspects of both DRAIM and RRAIM to provide good fault detection capability throughout an approach. The drawback of URAIM is that the same measurement equation must be used for position estimation and detection. Appendix E.2 shows that attempting to use the URAIM measurement equation solely for detection yields the same detection capability as DRAIM. Again, this results from the constraint requiring the test statistic to be independent from the state estimate error.

### **7.3 RAIM With Fixing Cycle Ambiguities**

URAIM greatly improves float availability within 5nmi of touchdown over DRAIM alone. However, when accuracy is also a concern, the float solution is often not sufficient to meet mission requirement. Fixing integers becomes necessary to improve accuracy; and, it can benefit integrity availability as well. In this work, the Enforced Position-Domain Integrity-Risk Cycle Resolution Algorithm (EPIC) is used with URAIM (which we call EPIC-URAIM). This is the first implementation of RAIM in which cycle ambiguities are fixed. When EPIC-URAIM is used to fix as many integers as possible without exceeding integrity risk, the average global (sea-based) integrity availability is 98.6 percent. In addition, accuracy availability computed using either the sigma average or sigma CDF methods also yields a 98.6 percent

global average.

#### 7.4 Recommendations and Future Work

Several improvements may be developed in the future for the EPIC-URAIM algorithm, and its assumptions. Although it does not seem necessary at this time because of relatively good integrity availability, there are opportunities to improve the performance of this algorithm. It may be possible to lower the integrity risk, or tighten the bound on the integrity risk.

One possible method of lowering the integrity risk that is worth investigating for the EPIC-URAIM algorithm is to consider a test statistic derived from the ‘fixed residual’. As its name suggests, the fixed residual is derived from the fixed solution, rather than from the float (as used in this work). To ‘tighten’ the integrity risk bound, the (multiple) simplifications made in attempting to optimize the candidate set for the faulted scenario can be addressed. In addition, the candidates from fault-free EPIC are used in computing the integrity risk bound for EPIC-URAIM. Fault-free EPIC eliminates certain candidates based on their fault-free probability of occurrence. So this same candidate region may not be ideal for the faulted case. Potentially useful candidates may be eliminated. Instead, the EPIC-URAIM algorithm can generate and eliminate candidates based on the faulted probability of occurrence. This is more memory and computationally expensive, which is why it was left out for initial algorithm feasibility study. However, it can provide the benefit of a tighter integrity risk bound.

Another aspect to consider is the computational efficiency (practical implementation) of the EPIC-URAIM algorithm. Increasing algorithm efficiency usually comes at the cost of a ‘less-tight’ bound on integrity risk. However, if the bound is far below the requirement, then it is possible to make simplifying assumptions to im-

prove computational efficiency. A good example of this, is increasing the threshold for throwing out candidates in Section 6.4. It did not affect overall system availability, but did facilitate the generation of sea-grid simulation results.

Finally, the possibility of using URAIM against other types of faults may be investigated. This includes, but is not limited to, ionospheric and tropospheric faults. Currently, an integrity allocation tree is used to divide the total allowable risk into integrity requirements for different faults such as ionospheric, tropospheric (including ducting), orbit ephemeris and others. It seems (inevitable) that at some point it will become desirable to combine the detection and integrity evaluation methods for all these faults, along with the fault free integrity, into a single algorithm.

APPENDIX A  
CLOSED-FORM EXPRESSION OF FINITE SERIES TERM FOR  
MEASUREMENT TIME-CORRELATION

In Section 3.2.3 the correlation of GF measurements with carrier measurements is expressed in terms of a finite series as shown in equation 3.19. In this appendix, the closed-form expression for this series is derived.

The finite geometric series given below has the corresponding closed-form solution, which we will show.

$$\sum_{p=1}^{m-1} e^{px} = (e^x) \frac{1 - e^{(m-1)x}}{1 - e^x}$$

The infinite geometric series has solution,

$$\begin{aligned} \sum_{p=1}^{\infty} e^{px} &= e^x + e^{2x} + e^{3x} + \dots \\ &= \frac{e^x}{1 - e^x} \end{aligned}$$

Then,

$$\begin{aligned} \sum_{p=1}^{m-1} e^{px} &= \sum_{p=1}^{\infty} e^{px} - \sum_{r=m}^{\infty} e^{rx} \\ &= \frac{e^x}{1 - e^x} - \frac{e^{mx}}{1 - e^x} \\ &= (e^x) \frac{1 - e^{(m-1)x}}{1 - e^x} \end{aligned} \tag{A.1}$$

Using a similar method we show that,

$$\sum_{p=1}^{m-1} p e^{px} = \frac{e^x [1 - m e^{(m-1)x} + (m-1) e^{mx}]}{(1 - e^x)^2}$$

This series is used in Appendix B to describe the variance of filtered GF measurements. We start by re-writing the summation as follows,

$$\sum_{p=1}^{m-1} p e^{px} = e^x + 2e^{2x} + 3e^{3x} + \dots + (m-1)e^{(m-1)x}$$

$$\begin{aligned}
&= e^x + e^{2x} + \dots + e^{(m-1)x} \\
&\quad + e^{2x} + e^{3x} + \dots + e^{(m-1)x} \\
&\quad \quad \quad \vdots \\
&\quad \quad \quad + e^{(m-2)x} + e^{(m-1)x} \\
&\quad \quad \quad \quad \quad \quad + e^{(m-1)x} \\
&= \sum_{r=1}^{m-1} e^{rx} + \sum_{r=2}^{m-1} e^{rx} + \dots + \sum_{r=m-1}^{m-1} e^{rx} \\
&= \sum_{q=1}^{m-1} \sum_{r=q}^{m-1} e^{rx}
\end{aligned}$$

Now we can use the previously obtained solution from equation A.1 to write,

$$\begin{aligned}
\sum_{p=1}^{m-1} p e^{px} &= (e^x) \frac{1 - e^{(m-1)x}}{1 - e^x} + (e^{2x}) \frac{1 - e^{(m-2)x}}{1 - e^x} + \dots + (e^{(m-1)x}) \frac{1 - e^{(1)x}}{1 - e^x} \\
&= \frac{e^x - e^{mx}}{1 - e^x} + \frac{e^{2x} - e^{mx}}{1 - e^x} + \dots + \frac{e^{(m-1)x} - e^{mx}}{1 - e^x} \\
&= \frac{e^x + e^{2x} + \dots + e^{(m-1)x}}{1 - e^x} - \frac{(m-1)e^{mx}}{1 - e^x} \\
&= e^x \frac{1 - e^{(m-1)x}}{(1 - e^x)^2} - \frac{(m-1)e^{mx}}{1 - e^x} \\
&= \frac{e^x - e^{mx} - (m-1)e^{mx} + (m-1)e^{(m+1)x}}{(1 - e^x)^2} \\
&= \frac{e^x [1 - me^{(m-1)x} + (m-1)e^{mx}]}{(1 - e^x)^2} \tag{A.2}
\end{aligned}$$

APPENDIX B  
DERIVATION OF GEOMETRY-FREE MEASUREMENT NOISE VARIANCE  
USING DISCRETE SAMPLING RATE

The variance of the filtered geometry free measurement given in equation 3.17 is derived under the assumption of a continuous sampling rate. In this appendix, the GF measurement variance is derived under the assumption of a discrete sampling rate. The derivation below follows a similar outline to the derivation of the correlation of GF measurements with carrier measurements in Section 3.2.3.

We begin by expressing the filtered GF variance as,

$$\begin{aligned} {}^i\sigma_{GF}^2 &= E\{v_{GF}^i v_{GF}^i\} \\ &= \frac{1}{i m^2} \sum_{q=1}^{i m} \sum_{p=1}^{i m} E\{v_{GF,q}^i v_{GF,p}^i\} \end{aligned} \quad (\text{B.1})$$

Using [SB88, p.566] we may write equation B.1 as,

$$\begin{aligned} {}^i\sigma_{GF}^2 &= \frac{{}^i m^i C_{xx}(0)}{i m^2} + \frac{2({}^i m - 1) {}^i C_{xx}(t_s)}{i m^2} + \frac{2({}^i m - 2) {}^i C_{xx}(2t_s)}{i m^2} + \dots \\ &\quad \dots + \frac{2({}^i m - ({}^i m - 1)) C_{xx}(({}^i m - 1)t_s)}{i m^2} \end{aligned}$$

Now substituting equation 3.13 for the autocovariance function we have,

$$\begin{aligned} {}^i\sigma_{GF}^2 &= \frac{{}^i m}{i m^2} {}^i\sigma_{GF}^2 + \frac{2({}^i m - 1)}{i m^2} {}^i\sigma_{GF}^2 e^{-t_s \beta} + \frac{2({}^i m - 2)}{i m^2} {}^i\sigma_{GF}^2 e^{-2t_s \beta} + \dots \\ &\quad \dots + \frac{2}{i m^2} {}^i\sigma_{GF}^2 e^{-(i m - 1)t_s \beta} \\ &= {}^i\sigma_{GF}^2 \left\{ \frac{1}{i m} + \frac{2({}^i m - 1)}{i m^2} e^{-t_s \beta} + \frac{2({}^i m - 2)}{i m^2} e^{-2t_s \beta} + \dots + \frac{2}{i m^2} e^{-(i m - 1)t_s \beta} \right\} \\ &= {}^i\sigma_{GF}^2 \left\{ \frac{1}{i m} + \frac{2}{i m} \sum_{r=1}^{i m - 1} (e^{-t_s \beta})^r - \frac{2}{i m^2} \sum_{r=1}^{i m - 1} r (e^{-t_s \beta})^r \right\} \end{aligned} \quad (\text{B.2})$$

The closed-form expressions for both summation terms in equation B.2 are given in Appendix A. The first summation term is given as equation A.1, and the second summation term is shown in equation A.2. Substituting these closed-form expressions into equation B.2 we have,

$${}^i\sigma_{GF}^2 = {}^i\sigma_{GF}^2 \left\{ \frac{1}{i m} + \frac{2}{i m} \frac{1 - (e^{-t_s \beta})^{i m - 1}}{1 - (e^{-t_s \beta})} e^{-t_s \beta} + \right.$$

$$-\frac{2}{i m^2} \frac{1 - i m (e^{-t_s \beta})^{i m - 1} + (i m - 1) (e^{-t_s \beta})^{i m}}{(1 - e^{-t_s \beta})^2} e^{-t_s \beta} \left. \right\} \quad (\text{B.3})$$

Equation B.3 represents the GF measurement noise variance under the assumption of a discrete sampling rate. To compare with equation 3.17, equation B.3 may be written in terms of filtering period  $\Upsilon$  rather than sampling interval  $t_s$  and number of samples  $m$ . Substituting  $m = \Upsilon/t_s + 1$  and taking limit as  $t_s \rightarrow 0$  (using the symbolic toolbox in Matlab) yields,

$$\lim_{t_s \rightarrow 0} {}^i \sigma_{GF}^2 = {}^i \sigma_{GF}^2 = {}^i \sigma_{GF}^2 \left\{ \frac{2}{i \Upsilon \beta} - \frac{2}{i \Upsilon^2 \beta^2} (1 - e^{-i \Upsilon \beta}) \right\} \quad (\text{B.4})$$

This result is consistent with equation 3.17.

APPENDIX C  
FILTERED GEOMETRY FREE MEASUREMENT CORRELATION WITH  
CARRIER MEASUREMENT AT INITIAL EPOCH

The correlation between filtered GF measurements and carrier measurements at initial epoch is derived in this appendix. Referring to Figure C.1, we see that the reference may start prefiltering each SV measurement as soon as it rises into view. So,  $n$  samples are filtered prior to the initial epoch, and  $m - n$  are afterwards. This differs from the derivation presented in Section 3.2.3 in that we will have two summation terms to deal with instead of a single term.



Figure C.1. GF carrier measurement sampling during approach

The correlation of GF measurements with carrier measurements at the initial epoch may be written as,

$$\begin{aligned}
 E\{^i\bar{\varepsilon}_{GF}^i \varepsilon_{\phi_w,0}\} &= \frac{1}{\lambda_w} E\{^i\bar{\varepsilon}_{\phi_w}^i \varepsilon_{\phi_w,0}\} \\
 &= \frac{1}{^i m \lambda_w} \sum_{q=1}^{i m} E\{^i \varepsilon_{\phi_w,q}^i \varepsilon_{\phi_w,n}\} \\
 &= \frac{1}{^i m \lambda_w} \left( \sum_{q=1}^{i n} E\{^i \varepsilon_{\phi_w,q}^i \varepsilon_{\phi_w,n}\} + \sum_{q=i n+1}^{i m} E\{^i \varepsilon_{\phi_w,q}^i \varepsilon_{\phi_w,n}\} \right) \quad (C.1)
 \end{aligned}$$

The first summation term has sample  $n$  at the end of the filtering interval. This is identical to the problem solved in Section 3.2.3 (equation 3.21). The second summation does not contain the  $n^{\text{th}}$  sample, and this corresponds to equation 3.20. Equation C.1 may be expressed as,

$$E\{^i\bar{\varepsilon}_{GF}^i \varepsilon_{\phi_w,0}\} = \frac{\sigma_{\phi_w}^2}{^i m \lambda_w} \left( \frac{1 - e^{-i n t_s \beta}}{1 - e^{-t_s \beta}} + (e^{-t_s \beta}) \frac{1 - (e^{-t_s \beta})^{i m - i n}}{1 - (e^{-t_s \beta})} \right) \quad (C.2)$$

Now, the expression is written terms of the ‘complete’ filtering interval  $\Upsilon$  (which begins when the reference starts filtering) and interval  $\Upsilon_a$  (which begins just after the initial epoch). Note that the total filtering time  $\Upsilon = t_s(m - 1)$  and filtering period

following the initial epoch measurement  $\Upsilon_a = t_s(m - n)$ . We may solve for  ${}^i n$  using these expressions,  ${}^i n = \left(\frac{\Upsilon - \Upsilon_a}{t_s} + 1\right)$ .

$$\begin{aligned} E\{\bar{\varepsilon}_{GF}^i \varepsilon_{\phi_w,0}^i\} &= \frac{\sigma_{\phi_w}^2}{({}^i \Upsilon / t_s + 1)\lambda_w} \left( \frac{1 - e^{-(\frac{\Upsilon - \Upsilon_a}{t_s} + 1)t_s\beta}}{1 - e^{-t_s\beta}} \right. \\ &\quad \left. + (e^{-t_s\beta}) \frac{1 - (e^{-t_s\beta})^{({}^i \Upsilon / t_s + 1) - (\frac{\Upsilon - \Upsilon_a}{t_s} + 1)}}{1 - (e^{-t_s\beta})} \right) \\ &= \frac{\sigma_{\phi_w}^2}{({}^i \Upsilon / t_s + 1)\lambda_w} \left( \frac{1 - e^{-(\frac{\Upsilon - \Upsilon_a}{t_s} + 1)t_s\beta}}{1 - e^{-t_s\beta}} + (e^{-t_s\beta}) \frac{1 - e^{-\Upsilon_a\beta}}{1 - (e^{-t_s\beta})} \right) \end{aligned}$$

Finally, after taking the limit as  $t_s \rightarrow 0$  we have,

$$\lim_{t_s \rightarrow 0} {}^i \sigma_{GF\phi_w,0}^2 := \frac{\sigma_{\phi_w}^2}{\lambda_w} \frac{1}{{}^i \Upsilon \beta} \left( 2 - e^{-i\Upsilon_a\beta} - e^{(i\Upsilon_a - i\Upsilon)\beta} \right) \quad (\text{C.3})$$

To compare this result to equation 3.23 we take the limit as  $\Upsilon \rightarrow \Upsilon_a$  the limit yields,

$${}^i \sigma_{GF\phi_w,0}^2 = \frac{{}^i \sigma_{\phi_w}^2}{\lambda_w} \frac{1}{{}^i \Upsilon \beta} \left( 1 - e^{-i\Upsilon\beta} \right) \quad (\text{C.4})$$

This is equivalent to equation 3.23, which is the result for current time carrier correlation. Referring to Figure C.1, when  $\Upsilon \rightarrow \Upsilon_a$  the initial epoch carrier measurement lies at one end of the filtering interval (just as the current time measurement does).

APPENDIX D  
INDEPENDENT TEST STATISTIC FOR RRAIM

In order to derive a RRAIM test statistic that is independent of the position state estimate error  $\delta\mathbf{x}$ , we extract only the portion of the residual  $\mathbf{r}_\Delta$  which is independent from the estimate error. We begin by writing the residual as sum of two components, one that is statistically independent from the estimate error, and one that is not (designated using subscripts  $I$  and  $NI$  respectively).

$$\mathbf{r} = \mathbf{r}_I + \mathbf{r}_{NI} \quad (\text{D.1})$$

By substituting the definition of  $\delta\mathbf{z}_\Delta$  into equation 4.19, the residual may be written as,

$$\begin{aligned} \mathbf{r} &= [\mathbf{I} - \mathbf{G}\mathbf{S}_\Delta]\delta\mathbf{z}_\Delta \\ &= [\mathbf{I} - \mathbf{G}\mathbf{S}_\Delta]\{\mathbf{E}(\delta\mathbf{z}_0 - \delta\mathbf{z}) - \mathbf{G}_\Delta\mathbf{E}_3\mathbf{S}_0\delta\mathbf{z}_0\} \end{aligned} \quad (\text{D.2})$$

Assuming that measurement errors at initial and current times are independent, the term  $\delta\mathbf{z}$  carries the correlation with  $\delta\mathbf{x}$  (because  $\delta\mathbf{x} = \mathbf{S}\delta\mathbf{z}$ ). We would like to extract the portion of  $\delta\mathbf{z}$  that is in the image of  $\mathbf{H}$ . (i.e.  $\delta\mathbf{z}_{\parallel,k} \in \text{Image}\{\mathbf{H}\}$ ) to calculate  $\mathbf{r}_{NI}$ . From the measurement equation 3.44 we can write the measurement error as follows.

$$\begin{aligned} \mathbf{z} &= \mathbf{H}\mathbf{u} + \delta\mathbf{z} \\ \delta\mathbf{z} &= \mathbf{H}\delta\mathbf{u} + (\mathbf{z} - \mathbf{H}\hat{\mathbf{u}}) \end{aligned} \quad (\text{D.3})$$

Note that the second term in equation D.3 is the residual of equation 3.44. So we can define the portion of the error in the image of  $\mathbf{H}$  as follows.

$$\delta\mathbf{z}_{NI} := \mathbf{H}\mathbf{S}\delta\mathbf{z}$$

The portion of the RRAIM residual derived from an element in the image of the observation matrix  $\mathbf{H}$  is,

$$\begin{aligned} \mathbf{r}_{NI} &= -[\mathbf{I} - \mathbf{G}\mathbf{S}_\Delta]\mathbf{E}\delta\mathbf{z}_{NI} \\ &= -[\mathbf{I} - \mathbf{G}\mathbf{S}_\Delta]\mathbf{E}\mathbf{H}\mathbf{S}\delta\mathbf{z} \end{aligned}$$

Substituting this result into equation D.1, we can solve for the statistically independent component of the residual.

$$\begin{aligned}
\mathbf{r}_I &= \mathbf{r} - \mathbf{r}_{NI} \\
&= \mathbf{r} + [\mathbf{I} - \mathbf{G}\mathbf{S}_\Delta]\mathbf{E}\mathbf{H}\mathbf{S}\delta\mathbf{z} \\
&= [\mathbf{I} - \mathbf{G}\mathbf{S}_\Delta]\delta\mathbf{z}_\Delta + [\mathbf{I} - \mathbf{G}\mathbf{S}_\Delta]\mathbf{E}\mathbf{H}\mathbf{S}\delta\mathbf{z}
\end{aligned}$$

Since vector  $\mathbf{r}_I$  is derived from the component of the estimate error orthogonal to all vectors in the image of the observation matrix  $\mathbf{H}$ , it will be statistically independent of the position error. We define a new measurement error vector, and denote it as the measurement component which is independent of the current time estimate error,

$$\begin{aligned}
\delta\mathbf{z}_I &:= \delta\mathbf{z}_\Delta + \mathbf{E}\mathbf{H}\mathbf{S}\delta\mathbf{z} \\
&= [\mathbf{E} - \mathbf{G}_\Delta\mathbf{E}_3\mathbf{S}_0]\delta\mathbf{z}_0 + [\mathbf{E}\mathbf{H}\mathbf{S} - \mathbf{E}]\delta\mathbf{z}
\end{aligned} \tag{D.4}$$

We can compute the noise covariance matrix  $\mathbf{V}_I$  of this newly formed measurement error,

$$\begin{aligned}
\mathbf{V}_I &= E\{\mathbf{v}_I\mathbf{v}_I^T\} \\
&= E\{[\mathbf{v}_\Delta + \mathbf{E}\mathbf{H}\mathbf{S}\mathbf{v}][\mathbf{v}_\Delta + \mathbf{E}\mathbf{H}\mathbf{S}\mathbf{v}]^T\} \\
&= \mathbf{V}_\Delta + [\mathbf{E}\mathbf{H}\mathbf{S}]\mathbf{V}[\mathbf{E}\mathbf{H}\mathbf{S}]^T + [\mathbf{E}\mathbf{H}\mathbf{S}]E\{\mathbf{v}\mathbf{v}_\Delta^T\} + E\{\mathbf{v}_\Delta\mathbf{v}^T\}[\mathbf{E}\mathbf{H}\mathbf{S}]^T
\end{aligned} \tag{D.5}$$

Finally, the residual statistically independent from the current time estimate error is,

$$\mathbf{r}_I = [\mathbf{I} - \mathbf{G}\mathbf{S}_\Delta]\delta\mathbf{z}_I \tag{D.6}$$

Unfortunately, this ‘independent’ residual cannot be computed using the measurement  $\mathbf{z}_I$ , because  $\mathbf{z}_I$  and  $\delta\mathbf{z}_I$  are not interchangeable in equation D.6. In other words,  $\mathbf{r}_I$  can be expressed using  $\delta\mathbf{z}_I$ , but it cannot be evaluated using  $\mathbf{z}_I$ .

APPENDIX E  
LIMITATIONS OF A MEASUREMENT EQUATION USED TO GENERATE  
THE TEST STATISTIC

In certain circumstances, it may not be feasible to modify the measurement equation used for estimation. In these cases, it is desirable to have a separate ‘detector’ (measurement equation used to generate the test statistic) which can be added to an existing system. At the same time, ensuring that the test statistic and estimate error are statistically independent can facilitate integrity risk evaluation.

In this appendix we show that the URAIM equation used for test statistic generation must also be used for position estimation to ensure the statistical independence between test statistic and estimate error. As an alternative, a set of criteria is presented to test whether a detection equation produces a test statistic independent of the state estimate error. The analysis is carried out using the parity space RAIM implementation. In this work, Gaussian distributed states are observed using weighted least squares (WLS), so the parity and residual RAIM interpretations are equivalent [Stu89].

We first formulate the problem. Let us define the full set of measurements,  $\mathbf{z}_{all} \in \mathbb{R}^m$ . As shown below, geometry free and DD carrier measurements at current time, as well as DD carrier at initial time are all stacked in a single vector.

$$\mathbf{z}_{all} := \left[ \mathbf{z}_{GF}^T \quad \phi^T \quad \phi_0^T \right]^T \quad (\text{E.1})$$

State estimate and parity vectors are noted  $\hat{\mathbf{u}}$  and  $\mathbf{p}$  respectively,

$$\hat{\mathbf{u}} = \mathbf{S}\mathbf{A}\mathbf{z}_{all} \quad \mathbf{p} = \mathbf{T}\mathbf{B}\mathbf{z}_{all}$$

where:

$$\begin{aligned} \mathbf{S}_e &\in \mathbb{R}^{N_e \times m_e} & \mathbf{T} &\in \mathbb{R}^{\square \times m_p} \\ \mathbf{A} &\in \mathbb{R}^{m_e \times m} & \mathbf{B} &\in \mathbb{R}^{m_p \times m} \end{aligned}$$

Matrices  $\mathbf{A}$  and  $\mathbf{B}$ , with full row-rank, are used to extract the measurements respectively used in estimation and test statistic generation. Again,  $\mathbf{S}_e$  is the weighted pseudoinverse used in estimation, and  $\mathbf{T}$  is a transformation used to generate the

parity vector. Note that  $\mathbf{T}$  is not yet fully defined, but it will be once we introduce the properties that our parity vector must possess in order to be useful in detection.

Note that subscripts  $e$  and  $p$  are used to denote terms corresponding to estimation and detection, respectively. The parity vector  $\mathbf{p}$  will be used to compute the test statistic. We want to derive a vector  $\mathbf{p}$  that satisfies the following conditions.

1.  $\mathbf{p}$  should be statistically independent from the state estimate  $\hat{\mathbf{u}}$ ,  $E\{\mathbf{p}\hat{\mathbf{u}}^T\} = 0$
2. When there is no fault  $E\{\mathbf{p}\}$  should be zero.
3. In the presence of a fault,  $E\{\mathbf{p}\}$  should be a function of the fault

Substituting the standard form of a linear measurement equation 2.18 into the parity vector expression, we have,

$$\begin{aligned}\mathbf{p} &= \mathbf{T}\mathbf{B}\mathbf{z}_{all} \\ &= \mathbf{T}\mathbf{z}_p \\ &= \mathbf{T}(\mathbf{H}_p\mathbf{u}_p + \mathbf{v}_p + \mathbf{f}_p)\end{aligned}$$

Taking the expected value of  $\mathbf{p}$  we obtain,

$$E\{\mathbf{p}\} = \mathbf{T}(\mathbf{H}_p\mathbf{u}_p + \mathbf{f}_p)$$

To satisfy the second criterion, it is required that  $\mathbf{T}\mathbf{H}_p = \mathbf{0}$ . We are then left with  $E\{\mathbf{p}\} = \mathbf{T}\mathbf{f}_p$ , which satisfies the third criterion.

Now, let us focus on the first condition of independence of  $\mathbf{p}$  with  $\hat{\mathbf{u}}$ . This will help determine  $\mathbf{T}$ . This condition has prevented the use of RRAIM in Section 4.2. Substituting expressions for  $\mathbf{p}$  and  $\hat{\mathbf{u}}$  into the first criterion results in,

$$E\{\mathbf{p}\hat{\mathbf{u}}^T\} = \mathbf{0}$$

$$\begin{aligned}\mathbf{TBE}\{\mathbf{z}_{all}\mathbf{z}_{all}^T\}\mathbf{A}^T\mathbf{S}_e^T &= \mathbf{0} \\ \mathbf{TBV}_{all}\mathbf{A}^T\mathbf{V}_e^{-1}\mathbf{H}_e(\mathbf{H}_e^T\mathbf{V}_e^{-1}\mathbf{H}_e)^{-1} &= \mathbf{0}\end{aligned}$$

Since the matrix  $(\mathbf{H}_e^T\mathbf{V}_e^{-1}\mathbf{H}_e)^{-1}$  has full rank, we may write,

$$\begin{aligned}\mathbf{TBV}_{all}\mathbf{A}^T\mathbf{V}_e^{-1}\mathbf{H}_e &= \mathbf{0} \\ \mathbf{TC} &= \mathbf{0} \quad \text{where: } \mathbf{C} := \mathbf{BV}_{all}\mathbf{A}^T\mathbf{V}_e^{-1}\mathbf{H}_e\end{aligned}\quad (\text{E.2})$$

This shows that  $\mathbf{T}$  must be in the left-null-space of the known matrix  $\mathbf{C}$  (i.e.  $\mathbf{T} \in \text{null}_L\{\mathbf{C}\}$ ). Then, we can specify that  $\mathbf{T}$  forms an orthonormal basis for the left-null-space of  $\mathbf{C}$ . Therefore, for the existence of a non-trivial solution,  $\mathbf{C}$  must have deficient row rank.

Note that when the same measurement equation is used for both estimation and test statistic generation, the first and second conditions collapse into a single criterion. In this case,  $\mathbf{A} = \mathbf{B} = \mathbf{I}$ ,  $\mathbf{V}_{all} = \mathbf{V}_e$ , and  $\mathbf{H}_e = \mathbf{H}_p := \mathbf{H}$

$$\begin{aligned}\mathbf{TBV}_{all}\mathbf{A}^T\mathbf{V}_e^{-1}\mathbf{H}_e = \mathbf{0} &\Rightarrow \mathbf{TH} = \mathbf{0} \\ \mathbf{TH}_p = \mathbf{0} &\Rightarrow \mathbf{TH} = \mathbf{0}\end{aligned}$$

However, when the test statistic is generated using a separate measurement equation from the one used in position estimation, the conditions do not collapse to a single criterion.

Given that equation 3.44 is used for estimation, the following examples analyze whether using the RRAIM or URAIM measurement equations solely for generating a test statistic, will produce one that is independent of the estimate error.

### E.1 Test Statistic Derived Using RRAIM Measurement Equation

Equation 4.9 may be expressed as,

$$\mathbf{z}_p := \mathbf{Bz}_{all} = \phi_\Delta - \mathbf{G}_\Delta \hat{\mathbf{x}}_0$$

To help simplify the example, we make the following assumptions. Assume that the change in SV geometry  $\mathbf{G}_\Delta$  during an approach is negligible. In addition, assume that carrier phase measurements are uncorrelated in time, and that GF measurements are uncorrelated with carrier measurements. We may write the extraction matrices  $\mathbf{A}$  and  $\mathbf{B}$  as,

$$\mathbf{A} := \begin{bmatrix} \mathbf{I} & \mathbf{0} & \mathbf{0} \\ \mathbf{0} & \mathbf{I} & \mathbf{0} \end{bmatrix} \quad \mathbf{B} := \begin{bmatrix} \mathbf{0} & -\mathbf{I} & \mathbf{I} \end{bmatrix}$$

Using these notations, equation E.2 becomes,

$$\begin{aligned} \mathbf{C} &:= \mathbf{B}\mathbf{V}_{all}\mathbf{A}^T\mathbf{V}_e^{-1}\mathbf{H}_e \\ &= \begin{bmatrix} \mathbf{G} & \mathbf{D}_\phi \end{bmatrix} \end{aligned}$$

This matrix has full row-rank. Therefore, only  $\mathbf{T} = \mathbf{0}$  satisfies the first criterion. This result is consistent with previous attempts to satisfy the first condition. It was shown in Section 4.2.3 that the RRAIM residual is correlated to the state estimate error.

In summary, under these assumptions, the test statistic derived using the original RRAIM measurement equation is not suitable for detection. To circumvent this problem, we try to generate a test statistic using the URAIM measurement equation.

## E.2 Test Statistic Derived Using URAIM Measurement Equation

Recall, the URAIM measurement equation

$$\mathbf{z}_p := \mathbf{B}\mathbf{z}_{all} = \mathbf{z}_{all} = \begin{bmatrix} \mathbf{z}_{GF} \\ \phi \\ \phi_0 \end{bmatrix}$$

Again, we make the same simplifying assumptions as in the RRAIM example ( $\mathbf{G}_\Delta = \mathbf{0}$ , carrier phase measurements are uncorrelated in time, and GF measurements are uncorrelated with carrier measurements). The extraction matrices become,

$$\mathbf{A} := \begin{bmatrix} \mathbf{I} & \mathbf{0} & \mathbf{0} \\ \mathbf{0} & \mathbf{I} & \mathbf{0} \end{bmatrix} \quad \mathbf{B} := \mathbf{I}$$

Equation E.2 becomes,

$$\begin{aligned}\mathbf{C} &= \mathbf{V}_{all} \mathbf{A}^T \mathbf{V}_e^{-1} \mathbf{H}_e \\ &= \begin{bmatrix} \mathbf{H}_e \\ \mathbf{0} \end{bmatrix}\end{aligned}\quad (\text{E.3})$$

This matrix has full col-rank (i.e.  $\text{rank}\{\mathbf{C}\} = N_e$ ). So, the left null space of  $\mathbf{C}$  has dimension  $m_p - N_e$  (i.e.  $\text{nullity}\{\mathbf{C}\} = m_p - N_e$ ). Therefore, there exists  $\mathbf{T} \neq \mathbf{0}$  which satisfies the first criterion, and  $\mathbf{T} \in \mathbb{R}^{(m_p - N_e) \times m_p}$ . Note that  $\mathbf{T}$  will not be unique.

In order to compute  $\mathbf{T}$  it is essential to satisfy the second criterion as well.

First, note that the relationship between  $\mathbf{H}_e$  and  $\mathbf{H}_p$  is,

$$\mathbf{H}_p = \begin{bmatrix} \mathbf{0} & \mathbf{H}_e \\ \mathbf{G}_0 & \mathbf{M} \end{bmatrix}\quad (\text{E.4})$$

Since the second criterion requires that  $\mathbf{T}$  be in the kernel of  $\mathbf{H}_p$ , we try defining  $\mathbf{T}$  as,  $\mathbf{T} := \begin{bmatrix} \mathbf{T}_1 & \mathbf{T}_2 \end{bmatrix}$ . Equation E.2 may be evaluated as,

$$\begin{aligned}\mathbf{0} &= \mathbf{TC} \\ &= \begin{bmatrix} \mathbf{T}_1 & \mathbf{T}_2 \end{bmatrix} \begin{bmatrix} \mathbf{H}_e \\ \mathbf{0} \end{bmatrix} \\ &= \begin{bmatrix} \mathbf{T}_1 \mathbf{H}_e \end{bmatrix}\end{aligned}\quad (\text{E.5})$$

Evaluating the second condition we obtain,

$$\begin{aligned}\mathbf{0} &= \mathbf{TH}_p \\ &= \begin{bmatrix} \mathbf{T}_1 & \mathbf{T}_2 \end{bmatrix} \begin{bmatrix} \mathbf{0} & \mathbf{H}_e \\ \mathbf{G}_0 & \mathbf{M} \end{bmatrix} \\ &= \begin{bmatrix} \mathbf{T}_2 \mathbf{G}_0 & \mathbf{T}_1 \mathbf{H}_e + \mathbf{T}_2 \mathbf{M} \end{bmatrix}\end{aligned}\quad (\text{E.6})$$

Simultaneously satisfying equation E.5 and E.6 requires that,

$$\mathbf{T}_2 \mathbf{G}_0 = \mathbf{T}_2 \mathbf{M} = \mathbf{0}\quad (\text{E.7})$$

Since  $\mathbf{T}_2$  can not be in kernel of both matrices, this statement can only be satisfied by the trivial solution  $\mathbf{T}_2 = \mathbf{0}$ .

Therefore, the transformation matrix becomes  $\mathbf{T} = \begin{bmatrix} \mathbf{T}_1 & \mathbf{0} \end{bmatrix}$ . Note that from the parity vector computation,

$$\begin{aligned} \mathbf{p} = \mathbf{T}\mathbf{z}_{all} &= \begin{bmatrix} \mathbf{T}_1 & \mathbf{0} \end{bmatrix} \begin{bmatrix} \mathbf{z}_{GF}^T \\ \phi \\ \phi_0 \end{bmatrix} \\ &= \mathbf{T}_1 \begin{bmatrix} \mathbf{z}_{GF}^T \\ \phi \end{bmatrix} \end{aligned} \quad (\text{E.8})$$

From equation E.8 we see that the parity vector generated from all the measurements is not influenced by the initial epoch measurements. This is because of the zero block ( $\mathbf{T}_2 = \mathbf{0}$ ) in our transformation matrix necessary to ensure that the test statistic is independent from state estimate error. Since, initial epoch measurements are not used in test statistic generation, the performance of this monitor will reduce to that of DRAIM.

**E.3 Working Detector Criteria** This section investigates characteristics that a detector must have in relation to the measurement equation used for position estimation, in order to successfully satisfy the established criteria. Recall, that generating a test statistic using the URAIM measurement equation requires that equation E.7 is satisfied. This means that  $\mathbf{T}_2$  must be in two kernels. However, if the measurements added to the measurement equation for estimation to form the measurement equation for detection have either a) all same states as estimation or b) no common states to the estimation equation, then this can work. For example, the observation matrix  $\mathbf{H}_p$  needs to have one of the two forms,

$$\mathbf{H}_p = \begin{bmatrix} \mathbf{0} & \mathbf{H}_e \\ \mathbf{K} & \mathbf{0} \end{bmatrix} \quad \text{or} \quad \mathbf{H}_p = \begin{bmatrix} \mathbf{H}_e \\ \mathbf{K} \end{bmatrix}$$

However, simplifying assumptions were made regarding independence of measurements. Note that this applies to a situation where the measurement equation used to

generate a test statistic contains all the measurements used for position estimation. Substituting code measurements at the initial epoch instead of carrier measurements at the initial epoch in the URAIM measurement equation produces a block diagonal form for  $\mathbf{H}_p$ . But, it seems that the code measurements are too noisy to provide good detection capability for applications requiring both high accuracy and integrity.

APPENDIX F  
CANDIDATE GENERATION FOR EPIC-LIGHT

The candidate vector  $\mathbf{c} := (\boldsymbol{\eta}_{NFF} - \boldsymbol{\eta})$  defines the offset of the candidate fix from the NFF. Since we want to evaluate all candidate fixes within the candidate region to compute the bound on integrity risk, we can stack all of these vectors into a matrix describing the candidate set.

First, we must decide the extent of the candidate region. A larger region produces a tighter integrity risk bound, but requires more computation resources. Let us build an example candidate matrix  $\mathbf{M}$  assuming a range of 1 cycle off of the NFF. For the first iteration of the bootstrap process, we have three integer candidates,  $-1$ ,  $0$ , and  $1$ . The candidate matrix for the first fixed integer (denoted using subscript 1) becomes,

$$\mathbf{M}_1 = \begin{bmatrix} -1 & 0 & 1 \end{bmatrix}$$

For successive fixes, the matrix forms a combination tree,

$$\mathbf{M}_2 = \begin{bmatrix} -1 & 0 & 1 & -1 & 0 & 1 & -1 & 0 & 1 \\ -1 & -1 & -1 & 0 & 0 & 0 & 1 & 1 & 1 \end{bmatrix}$$

so, 
$$\mathbf{M}_k = \begin{bmatrix} \mathbf{M}_{k-1} & \mathbf{M}_{k-1} & \mathbf{M}_{k-1} \\ -\mathbf{1}_{1 \times 3^k} & \mathbf{0}_{1 \times 3^k} & \mathbf{1}_{1 \times 3^k} \end{bmatrix}$$

For a larger candidate set, we can consider 2 or more cycles off of the noise free fix. In an attempt to conserve computational resources, candidates that have a low probability of occurrence are eliminated.

## BIBLIOGRAPHY

- [BP00] J. S. Bendat and A. G. Piersol. *Random Data: Analysis and Measurement Procedures*. John Wiley and Sons, New York, NY, 3rd edition, 2000.
- [Cha01] F. Chan. Detection of global positioning satellite orbit errors using short-baseline carrier phase measurements. Master's thesis, Illinois Institute of Technology, 2001.
- [GJP] L. Gratton, M. Joerger, and B. Pervan. Carrier phase relative raim algorithms and protection level derivation. In *Proc. of the ION GPS*.
- [GP06] L. Gratton and B. Pervan. Carrier phase airborne and ground monitors for ionospheric front detection for category iii laas. In *Proc. of the 19th International Technical Meeting of the Satellite Division of the Institute of Navigation*, pages 1212–1223, 2006.
- [GPSa] *GPS Constellation Figure*. Available online at [http://140.137.13.100/derceng/SERVICE/SE\\_JPG/cstech014.jpg](http://140.137.13.100/derceng/SERVICE/SE_JPG/cstech014.jpg).
- [GPSb] *GPS System Architecture Figure*. Available online at <http://connet.us/gps.htm>.
- [Heo04] M.B. Heo. *Robust Carrier Phase DGPS Navigation for Shipboard Landing of Aircraft*. PhD thesis, Illinois Institute of Technology, 2004.
- [HP04] M.B. Heo and B. Pervan. Autonomous fault detection with carrier-phase dgps for shipboard landing navigation. *Journal of the ION*, 51.3, Fall 2004.
- [JKSP11] M. Joerger, S. Khanafseh, S. Stevanovic, and B. Pervan. *Unified RAIM Approach Against Orbit Ephemeris Faults using the Bootstrap Fixing Process*. Presented as IIT periodic review for JPALS, December 2011.
- [JKSP12] M. Joerger, S. Khanafseh, S. Stevanovic, and B. Pervan. *Airborne Unified RAIM for EPIC-light and Standalone RAIM Against Orbit Ephemeris Faults*. Presented as IIT periodic review for JPALS, February 2012.
- [JSKP] M. Joerger, S. Stevanovic, S. Khanafseh, and B. Pervan. Differential raim and relative raim for orbit ephemeris fault detection. In *Proc. of the ION GPS*.
- [Kha08] S. Khanafseh. *GPS Navigation Algorithms for Autonomous Airborne Refueling of Unmanned Air Vehicles*. PhD thesis, Illinois Institute of Technology, 2008.
- [KP10] S. Khanafseh and B. Pervan. New approach for calculating position domain integrity risk for cycle resolution in carrier phase navigation systems. *IEEE Transactions on Aerospace And Electronic Systems*, 46.1, January 2010.
- [Lag07] M. Lage. *UCAS-N Requirements Allocation*. Presented at UCAS briefing, March 2007.

- [ME06] P. Misra and P. Enge. *Global Positioning System: Signals, Measurement, and Performance*. Ganga-Jamuna Press, Lincoln, MA, 2006.
- [MMB<sup>+</sup>00] G. McGraw, T. Murphy, M. Brenner, S. Pullen, and A. Van Dierendonck. Development of the laas accuracy models. In *Proc. of the ION GPS*, pages 1212–1223, 2000.
- [oD08] Department of Defense. Global positioning system standard positioning service performance standard. Technical report, DOD, September 2008. Available online at <http://www.gps.gov/technical/ps/2008-SPS-performance-standard.pdf>.
- [Per96] B. Pervan. *Navigation Integrity for Aircraft Precision Landing Using the Global Positioning System*. PhD thesis, Stanford University, 1996.
- [PG05] B. Pervan and L. Gratton. Orbit ephemeris monitors for local area differential gps. *IEEE Transactions on Aerospace and Electronic Systems*, 41.2, 2005.
- [SB88] K. Sam Shanmugan and A.M. Breipohl. *Random Signals: Detection, Estimation and Data Analysis*. John Wiley and Sons, New York, NY, 1988.
- [Stu89] M.A. Sturza. Navigation system integrity monitoring using redundant measurements. *Journal of the ION*, 35.4, Winter 1988-89.
- [Tea07] Federal Aviation Administration GPS Product Team. Global positioning system standard positioning service performance analysis report. Technical Report 58, FAA, July 2007. Available online at <http://www.nstb.tc.faa.gov/DisplayArchive.htm>.
- [Teu98] P.J.G. Teunissen. A probabilistic evaluation of correct gps ambiguity resolution. In *Proc. of the 11th International Technical Meeting of the Satellite Division of the Institute of Navigation*, 1998.
- [Teu01a] P.J.G. Teunissen. Gns ambiguity bootstrapping: Theory and application. In *Proc. KIS2001, International Symposium on Kinematic Systems in Geodesy*, pages 246–254, 2001.
- [Teu01b] P.J.G. Teunissen. The probability distribution of the ambiguity bootstrapped gns baseline. *Journal of Geodesy*, 75, January 2001.
- [TPE<sup>+</sup>10] H. Tang, S. Pullen, P. Enge, L. Gratton, B. Pervan, M. Brenner, J. Scheitlin, and P. Kline. Ephemeris type a fault analysis and mitigation for laas. In *Proc. IEEE/ION PLANS 2010*. Indian Wells, CA, 2010.
- [WE95] T. Walter and P. Enge. Weighted raim for precision approach. In *Proc. ION GPS*. Palm Springs, CA, 1995.
- [WPF08] S. Wu, S. Peck, and R. Fries. Geometry extra-redundant almost fixed solutions: A high integrity approach for carrier phase ambiguity resolution for high accuracy relative navigation. In *Proc. IEEE/ION PLANS 2010*, pages 568–582. Monterey, CA, 2008.